

Hydrogen in Austenite: What Changes after Martensitic Transformation?

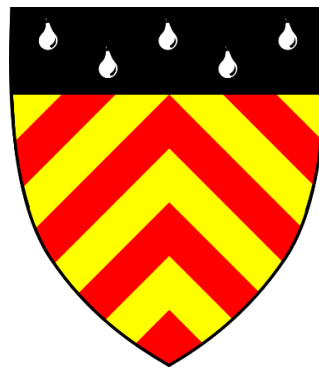
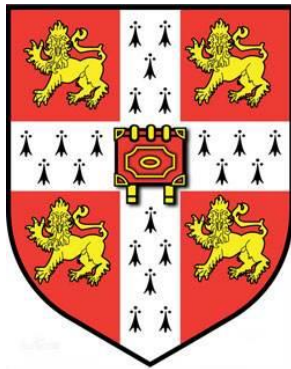
Thesis for MPhil in Materials Science and Metallurgy

by

Shengda Pu

25th Sep 2018

Supervised by Dr. Steve Ooi and Prof. H.K.D.H. Bhadeshia



Phase Transformations and Complex Properties Research Group

Department of Materials Science and Metallurgy

University of Cambridge

Preface

This thesis is submitted for the degree of Master of Philosophy in Materials Science and Metallurgy at the University of Cambridge in 2017/2018. This work is, to my best knowledge, original. Any mention of previous work in this thesis has been properly referenced and acknowledged. Some part of the work has been presented in the following literatures:

- S.D. Pu, A. Turk, S. Lenka, S.W. Ooi, 'Study of hydrogen release resulting from the transformation of austenite into martensite', *Materials Science and Engineering: A*, Vol. 754 (2019), pp. 628-635
- S.D. Pu, A. Turk, S. Lenka, S.W. Ooi, 'Hydrogen Desorption Change after Deformation of a Bainitic Steel with Unstable Retained Austenite', *Scripta Materialia*, Vol. 170 (2019), pp. 38-42
- S.D. Pu, S.W. Ooi, 'Hydrogen Transport by Dislocation Movement in Austenitic Steel' (accepted to *Materials Science and Engineering: A*, 2019)

Acknowledgements

I would like to thank both of my supervisors, Steve and Harry, for this great opportunity to work on this interesting project and for their constant guidance throughout this project. It is a great honour to work with them.

I would also like to thank all the PT group members and other department members who have provided me with all kinds of help throughout this year. I would like to thank Andrej Turk for his help on TDA simulation and Mary Vickers for her help on XRD quantification. I would like to thank Dominik for showing me how to use the laboratory and Mo for being the coolest deskmate ever. Most of all, I want to thank Shaumik Lenka, who constantly helped me with different experiments and data analysis, I could have never done this project without his help.

Finally, I would like to thank my family, I would not be in Cambridge without their support and love.

Table of Contents

Preface	- 1 -
Acknowledgements.....	- 1 -
Abstract.....	- 3 -
1 Introduction	- 4 -
1.1 Hydrogen embrittlement in steels.....	- 4 -
1.2 Hydrogen diffusion and trapping.....	- 6 -
1.3 Hydrogen in austenite.....	- 14 -
1.4 Thermal desorption analysis	- 16 -
1.5 Microprinting	- 18 -
2 Experimental method	- 19 -
2.1 Specimen preparation.....	- 19 -
2.2 Hydrogen charging.....	- 21 -
2.3 Compression	- 22 -
2.4 Metallography using optical microscopy	- 22 -
2.5 Scanning electron microscopy	- 23 -
2.6 X-ray diffraction	- 23 -
2.7 Hydrogen desorption analysis.....	- 24 -
2.8 Microprinting	- 25 -
3 Results and Discussion	- 26 -
3.1 Starting material characterisation	- 26 -
3.2 Deformation-induced martensitic transformation	- 35 -
3.3 The effect of hydrogen charging time.....	- 45 -
3.4 Changes in room-temperature hydrogen desorption and XRD after compression.....	- 61 -
3.5 Changes in constant-heating-rate TDA after compression.....	- 67 -
3.6 Effect of room-temperature aging.....	- 74 -
3.7 Other interesting desorption results from side experiments	- 83 -
3.8 Visualization of hydrogen	- 87 -
4. Conclusions	- 93 -
5. Lessons learnt from failed attempts and future work	- 95 -

Abstract

Diffusible hydrogen in steels can cause embrittlement. Hydrogen has much lower diffusivity in austenite than in ferrite. Therefore, austenite is relatively immune to embrittlement. However, the poor stability of austenite can lead to martensitic transformation. And martensite cannot dissolve all the hydrogen inherited from austenite due to its lower solubility. So, what will happen to this excess hydrogen? This is the topic explored in this project.

Three types of steel with different austenite contents and austenite stability were investigated: duplex steel, austenitic steel and bainitic steel. Their deformation induced phase transformation of austenite and the corresponding hydrogen desorption behaviour were studied using microscopy, diffraction, thermal desorption analysis and microprinting.

This work has shown that the change in hydrogen desorption behaviour after compression strongly depends on the dissolved hydrogen concentration and the extent of phase transformation. For duplex steel, containing a large hydrogen concentration (up to 40 ppmw) and no phase transformation after compression, there is no noticeable change in hydrogen behaviour according to room-temperature desorption and constant-heating-rate thermal desorption analysis. On the other hand, the austenitic steel, after compression, revealed a significant burst in the hydrogen desorption rate, indicating an overall increase in hydrogen diffusivity. In the case of the bainitic steel, with very low saturated hydrogen concentration (less than 0.5 ppmw) and a little phase transformation (less than 10%) after compression, a significant reduction in the hydrogen desorption rate was detected since the newly strain-induced defects were able to trap almost all the diffusive hydrogen.

1 Introduction

1.1 Hydrogen embrittlement in steels

Hydrogen can be introduced into steels during various stages of production and in service. Hydrogen was first proven and reported as a cause of embrittlement (reduction of toughness) in steel in 1875 by W. H. Johnson [1]. It was found that with the infusion of hydrogen, metals show a significant reduction in fracture strength and ductility. Since then, it has become the subject of intensive research. However, its exact mechanism remains a subject of debate. Many theories have been proposed to explain hydrogen embrittlement.

The first one, “pressure theory”, was introduced in 1935 by Benneck [2], who suggested that atomic hydrogen in metal tends to form molecular hydrogen in voids or microcracks, which exerts an internal pressure. This reduces the external stress required for crack initiation and propagation. It was also observed that this internal pressure can, by itself, produce cracks without any external forces at high fugacity [3]. The pressure theory has been used by many to explain various hydrogen related failures in hydrogen-rich environments. However, it is not the best theory to explain embrittlement when hydrogen content is as low as several parts per million (ppm).

Petch’s theory [4][5] of embrittlement was introduced later in 1952, that the absorbed hydrogen atoms reduce the surface energy of metal, in turn reducing the stress needed to create new surfaces during cracking.

In-situ transmission electron microscopy (TEM) observation of the enhancement of dislocation movements by hydrogen was made in 1984 [6]. This phenomenon was further explored by Birnbaum, who later proposed a hydrogen-enhanced localized plasticity (HELP) mechanism [7]. It is proposed that hydrogen shields the stress field around dislocations, so they interact with fewer

other dislocations or defects. Therefore, they can move more easily, and work hardening becomes less likely to happen, leading to local plasticity far below yield stress.

Another interesting theory is the hydrogen-enhanced strain-induced vacancy (HESIV) model [8][9]. It is different from most other theories in that it does not consider hydrogen's direct involvement in crack initiation or propagation. It proposes that the main role of hydrogen is to induce and agglomerate vacancies in the material during deformation. It is the vacancies, rather than hydrogen itself, that is responsible for the embrittlement. Supporting experiments have shown that the presence of hydrogen during the later stage of straining and fracture is not required for the reduction in toughness and fracture strength, as long as it was present in the early stage of plastic straining [10].

Many other theories exist, for example, cohesion theory [11], hydrides theory [12] etc. However, due to the existence of a huge range of various steels with different microstructure and strength, it is impossible to perfectly fit one single theory to all types of steels. It is nevertheless accepted that only diffusible hydrogen is harmful to toughness [13] and that hydrogen embrittlement is a diffusion-controlled process. This makes understanding the movement of hydrogen within steels a critical factor for understanding hydrogen embrittlement.

1.2 Hydrogen diffusion and trapping

Due to their small size, hydrogen atoms occupy and migrate via interstitial sites in crystalline structures. The diffusivity of hydrogen in austenite is much lower than in ferrite, i.e. migration energy E_m in austenite is higher, as shown in Figure 1.1.

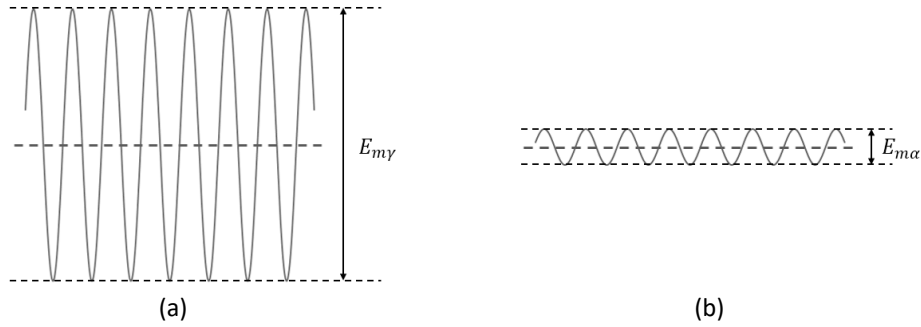


Figure 1.1: Schematic of the difference in migration energy E_m of hydrogen in austenite (a) and in ferrite (b), $E_{m\gamma} = 52.12 \text{ kJ mol}^{-1}$ for 304 austenitic steels and $E_{m\alpha} = 4.5 \text{ kJ mol}^{-1}$ for 99.99% pure iron

In high purity ferritic steels with minimal defects [14], the diffusivity of hydrogen is:

$$D_{\alpha}(\text{m}^2 \text{ s}^{-1}) = (5.8 \pm 0.1) \times 10^{-8} \exp\left(-\frac{4.5 \times 10^3 \pm 200}{RT}\right) \quad \text{(Equation 1)}$$

R : ideal gas constant, 8.314 J kg^{-1} , T : temperature in K

Katsuta [15] compiled many hydrogen diffusion results for different austenitic steels and gave an estimation for hydrogen diffusivity in austenite:

$$D_{\gamma}(\text{m}^2 \text{ s}^{-1}) = (9.9 \pm 0.6) \times 10^{-7} \exp\left(-\frac{52.12 \times 10^3 \pm 551}{RT}\right) \quad \text{(Equation 2)}$$

At room temperature (25°C), $D_{\gamma} = 7.4 \times 10^{-16} \text{ m}^2 \text{ s}^{-1}$ and $D_{\alpha} = 5.8 \times 10^{-8} \text{ m}^2 \text{ s}^{-1}$. Applying diffusion length equation 3, we can see that it takes less than 1 s for hydrogen to diffuse $100 \mu\text{m}$ in ferrite and this same diffusion length will take tens of days in austenite. The solubility of hydrogen, on the other hand, is two to three orders of magnitude higher in austenite than in ferrite at ambient conditions.

$$l = \sqrt{4Dt} \quad \text{(Equation 3)}$$

l : diffusion length after diffusing for time t

Assuming a constant surface concentration during charging, the concentration depth profile can be estimated using finite element simulation or the diffusion equation [16]:

$$N(x, t) = N(0)\operatorname{erfc}\left(\frac{x}{\sqrt{4Dt}}\right) \quad \text{(Equation 4)}$$

$N(0)$: concentration of hydrogen at the charging surface, $N(x, t)$: concentration of hydrogen x metres away from the charging surface at time t

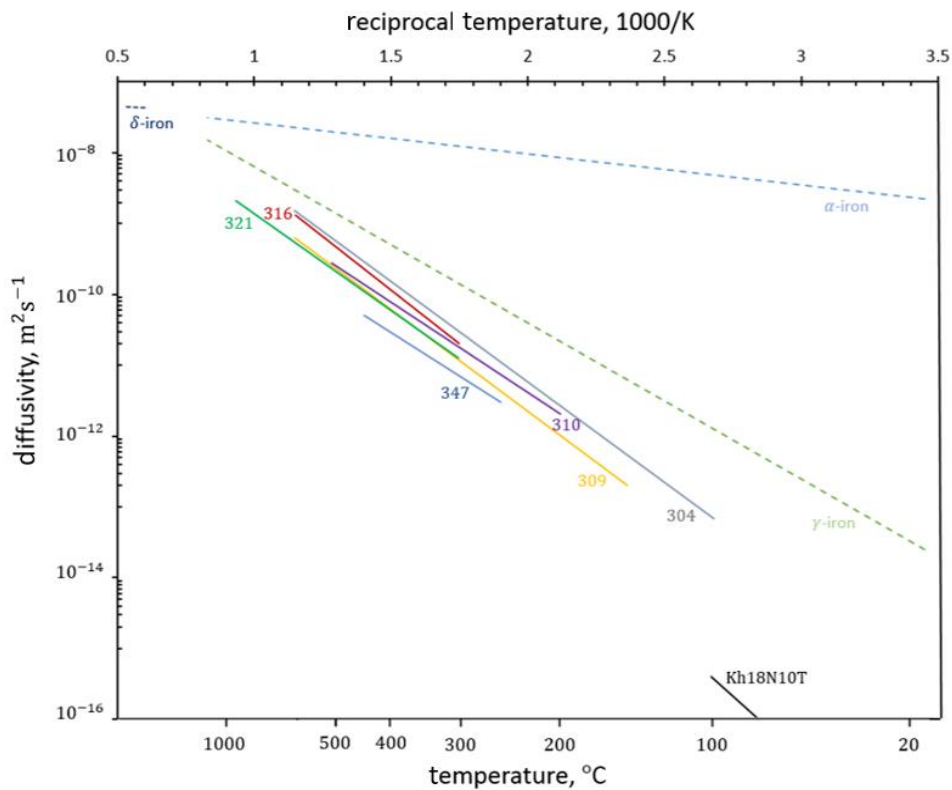


Figure 1.2: Diffusivity of hydrogen in different type of steels [15] [17]

However, the actual diffusion process in steels is a much more complex process. For example, the addition of alloying elements can significantly vary the diffusion behaviour and solubility of hydrogen. Figure 1.2 compares some of the reported hydrogen diffusivity values in different austenitic steels and in pure ferrite.

Within the lattice, defects can interact with hydrogen atoms and become sites that are more energetically favourable for hydrogen to sit in. These sites are called hydrogen ‘traps’. The illustration of such energy well is shown in figure 1.3. Table 1.1 compiles some of the published binding energy values of different traps.

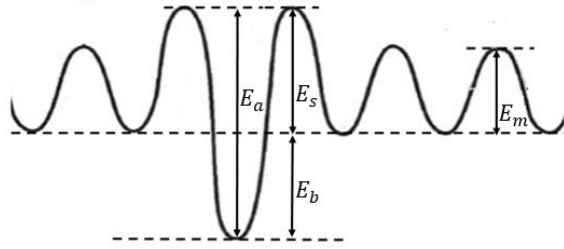


Figure 1.3: Schematic of a typical hydrogen trap, E_m : Lattice migration energy, E_a : trap's activation energy, E_b : trap's binding energy, E_s : Saddle point energy (notice: E_s could be either bigger or smaller than E_m)

Trap site	Phase	$E_b/\text{kJ mol}^{-1}$	Method
Single iron-vacancy	α	49–78	Diffusion analysis
Single iron-vacancy	α	24–29	First principles calculations
Cr, Mo or V atom	α	26–27	Elastic/electronic calculations
Mn atom	α	11	Elastic/electronic calculations
Ni atom	α	-12	Elastic/electronic calculations
C atom	α	3	Magnetic relaxation
N atom	α	13	Magnetic relaxation
Al atom	γ	6	First principles calculation
Ti atom	α	26	Permeability
grain boundaries	α	32	Mechanical analysis
γ/α interface	$\gamma+\alpha$	52	Permeability
Dislocation strain field	α	23-27	Diffusion analysis, TDA
Dislocation core/jogs	α	60	Diffusion analysis
Microvoids	α	48	Thermal desorption analysis
ϵ -carbide	α	65	
Cementite/ α interfaces	α	11-18	Permeability, TDA
TiC	α	46-116	Permeability
$\text{Fe}_{1.2}\text{Ti}_{0.8}\text{S}_2$	α	58	Thermal desorption spectroscopy
V_4C_3	α	33-35	Thermal desorption analysis
Coherent M_2C (Mo-rich needle)	α	11-12	Thermal desorption analysis
MnS	α	72	
MnS/ α interfaces	α	72	Thermal desorption analysis
Iron oxide/ α interfaces	α	51-70	Thermal desorption analysis
$\text{Y}_2\text{O}_3/\alpha$ interfaces	α	70	Thermal desorption analysis
$\text{Al}_2\text{O}_3/\alpha$ interfaces	α	79	Thermal desorption analysis

Table 1.1: Published data on binding energies E_b of different trap sites measured by different methods, compiled by Prof. Bhadeshia [18]

A trap's trapping capability depends on its stress field's interaction with hydrogen [19]. A non-worked single-phased steel usually has low intrinsic trap density of around 10^{19} cm^{-3} . Introducing lattice defects through, for example cold rolling, can greatly increase (several orders of magnitude) trap density. This leads to a remarkable increase in hydrogen content and a decrease in effective diffusivity of hydrogen in steels. Taking trapping into account, the apparent diffusivity [20] and hydrogen content [21] become:

$$D_{app} = D_L \times \left[1 + \frac{N_T}{N_L} \exp\left(\frac{E_b}{RT}\right) \right]^{-1} \quad \text{(Equation 5)}$$

D_L : diffusivity in perfect lattice, N_T : trap number density, N_L : lattice site number density, E_b : binding energy of traps

$$C_{Total} = C_L + \sum_i Z_i \theta_i N_i \quad \text{(Equation 6)}$$

C_L : hydrogen concentration in perfect lattice, N_i : number density of traps of type i , θ_i : percentage fraction of traps of type i that are filled with hydrogen, Z_i : number of hydrogen atoms trapped at each trap of type i

For simplicity, in most simulations, $Z = 1$, therefore:

$$\theta_i = \frac{C_i}{N_i} \quad \text{(Equation 7)}$$

C_i : hydrogen concentration in traps of type i

For dislocations and grain boundaries, N_i can be approximated to be [22]:

$$N_{Dis} \approx \pi b^2 \rho N_L \quad \text{(Equation 8)}$$

b : magnitude of the Burger's vector, ρ : dislocation density

$$N_{GB} \approx L_{GB} b N_L \quad \text{(Equation 9)}$$

L_{GB} : total length of grain boundaries higher than 2° per unit area

Both trap density and trapping capability increase with cold working [20]. The strain-induced increase of hydrogen solubility and reduction in apparent diffusivity can be largely restored by the removal of these defects through annealing [23] [24]. Various traps with different trapping capability can exist simultaneously in the same material. Taking into account contributions from different traps, McNabb and Foster [25] modified Fick's second law and proposed a dynamic trapping/detrapping kinetic model. For traps of type i :

$$\frac{\partial C_L}{\partial t} + \sum_i \frac{\partial C_i}{\partial t} = \frac{\partial^2 C_L}{\partial x^2} \quad \text{(Equation 10)}$$

$$\frac{dC_i}{dt} = k C_L (1 - \theta_i) - p C_i \quad \text{(Equation 11)}$$

The first part of equation 11 describes the trapping process and the second part describes the detrapping process, where:

$$k = k_0 \exp\left(-\frac{E_s}{RT}\right) \quad \text{(Equation 12)}$$

$$p = p_0 \exp\left(-\frac{E_s + E_b}{RT}\right) \quad \text{(Equation 13)}$$

E_s & E_b : as defined in figure 1.3, k_0 & p_0 : constants

Oriani's local equilibrium model [20] assumes local equilibrium between hydrogen content in lattice and in traps during diffusion:

$$\frac{\theta_i(1-\theta_L)}{\theta_L(1-\theta_i)} = \exp\left(\frac{E_b}{RT}\right) \quad \text{(Equation 14)}$$

θ_L : the atomic fraction of lattice sites filled with hydrogen

Many simulations of hydrogen absorption and desorption are based on these two models. From which, thermal desorption analysis (TDA) profiles can be simulated taking into account traps of various types.

Traps are generally divided into two groups according to their trapping power, 'weak/reversible traps' and 'strong/irreversible traps'. When a hydrogen atom encounters a weak trap, it can 'detrap' itself relatively easily by thermal or mechanical energy. These detrapped hydrogen atoms are diffusible and can lead to embrittlement. However, when a hydrogen atom encounters a strong trap, it cannot get out easily by itself unless a substantial amount of thermal energy is provided. The hydrogen atoms in these traps are not diffusible, therefore cannot contribute to the embrittlement process. Several types of common hydrogen traps are described below.

1. Dislocation

A dislocation core is a low energy site for hydrogen atoms to sit in. During slow-rate plastic deformation, each moving dislocation can carry the interacted hydrogen atoms with it and therefore enhance their effective diffusivity within the lattice [26] [27]. The interaction energy between the stress fields of a hydrogen atom and an edge dislocation is [17]:

$$W = \frac{Gb(1+\nu)\delta V \sin\theta}{3\pi(1-\nu)r} \quad \text{(Equation 15)}$$

G : shear modulus, b : magnitude of the Burger's vector, ν : Poisson's ratio, δV : volume change around the hydrogen atom, $\approx 1.2 \text{ ml mol}^{-1}$ in iron, r & θ : the hydrogen atom's position coordinates with respect to the dislocation

In comparison, screw dislocations have no long-range hydrostatic stress field thus their interaction with hydrogen is shorter-ranged [28]. As mentioned before, hydrogen can also shield the stress fields around dislocations and therefore significantly enhances their movement [6] during plastic deformation and enhances the generation of dislocations around a crack tip [29]. This leads to the notion of hydrogen-enhanced local plasticity and strain localization. In this project, dislocation density is estimated from X-ray diffraction (XRD) spectra using the Williamson-Hall technique [30], which correlates the peaks' width and the micro-strain ε :

$$FWHM \times \cos(\theta) \approx 2 \varepsilon \sin(\theta) \quad \text{(Equation 16)}$$

θ : peak position, FWHM: full width half maximum of each diffraction peak

From micro-strain ε , dislocation density ρ is estimated:

$$\rho = 6\pi \frac{\varepsilon^2}{b^2} \quad \text{(Equation 17)}$$

For body-centred-cubic (BCC) ferrite with lattice parameter a_α :

$$b = \frac{\sqrt{3}}{2} a_\alpha \quad \text{(Equation 18)}$$

Whereas for face-centred-cubic (FCC) austenite with lattice parameter a_γ :

$$b = \frac{\sqrt{2}}{2} a_\gamma \quad \text{(Equation 19)}$$

2. Microcrack

When strain-induced traps were first observed, many believed that the increase in hydrogen content is mainly due to the increase in dislocation density. However, this was later proven not to be the case. By comparing the changes in dislocation density and trap density after staining and after annealing, Oriani pointed out that microcracks play a more important role than dislocations as hydrogen traps [20].

3. Point defect

By comparing TDA spectra of deformed and annealed specimens, Nagumo pointed out that the enhanced hydrogen absorption due to deformation can be almost completely removed by annealing the specimen at as low as 200 °C, which corresponds to the removal of point defects like vacancies and vacancy-carbon pairs rather than dislocations [31]. The same observation was also made by Takai [10] and Aoki [32].

4. Precipitate

Precipitates like carbides and nitrides also act as traps for hydrogen. TiC, for example, is well known as an irreversible strong hydrogen trap with a reported E_a value of 86.9 kJ mol⁻¹ [33]. Other carbides like NbC and VC can also act as traps and can mitigate the hydrogen induced fracture phenomena, though their reported trapping power is not as high as that of TiC [29]. The trapping power of such precipitates normally depends on the precipitate/matrix interface coherency and precipitate size [34]. For example, NbC and TiC were found to be ineffective in hydrogen trapping in Nickel alloys [35] since these precipitates form incoherent interfaces with the matrix, compared to the coherent or semi-coherent interfaces in steels which induce elastic strain field.

4. Grain boundary

The role of grain boundaries in hydrogen diffusion is unclear. Many different values have been reported as their trapping energy in steels. This is not only due to the diverse types and structures of grain boundaries exist in steels, but also due to fact that they are segregation sites for different impurity and sites for precipitates formation. It is reported that hydrogen tends to segregate to grain boundaries [36] [37]. Hydrogen induced cracking also tends to initiate from and grow along grain boundaries [38] [39]. On the other hand, it is also reported that hydrogen embrittlement is generally suppressed by grain refinement [40] [41]. Therefore, it is still under debate whether increasing the grain boundary suppresses or enhances hydrogen embrittlement in steels.

To better correlate hydrogen desorption with different traps in a material, it is important to characterize its grain size, grain boundary etc. The linear intercept method is used to characterize grain size as illustrated in ASTM E112 standard [42]. Mean linear intercept length (\bar{L}) is:

$$\bar{L} = 1 / \bar{n}_L \quad \text{(Equation 20)}$$

n_L : number of grains intercept by a line of 1 mm. \bar{n}_L : mean n_L

(Notice: linear intercept value does not equal the actual average grain diameter; most grains' full size is not displayed on the plane of observation because they are cut at different sections)

Mean grain boundary surface area to volume ratio (\bar{S}_v) is:

$$\bar{S}_v = 2 \bar{n}_L = 2/\bar{L} \quad \text{(Equation 21)}$$

In textured samples, like rolled sheets, these values are found individually for each direction, rolling, normal, transverse and the overall \bar{n}_L and \bar{L} are:

$$\bar{n}_L = \sqrt[3]{\bar{n}_{\text{Rolling}} \cdot \bar{n}_{\text{Normal}} \cdot \bar{n}_{\text{Transverse}}} \quad \text{(Equation 22)}$$

$$\bar{L} = \sqrt[3]{\bar{L}_{\text{Rolling}} \cdot \bar{L}_{\text{Normal}} \cdot \bar{L}_{\text{Transverse}}} \quad \text{(Equation 23)}$$

For a material with multiple phases, the mean grain size of phase A, $\bar{n}_{L,A}$ is:

$$\bar{L}_A = V_A / \bar{n}_{L,A} \quad \text{(Equation 24)}$$

V_A : volume fraction of phase A

For bainitic structure, another critical parameter in hydrogen trapping is the ferrite/austenite interface area. Mean linear intercept length from plate's perpendicular direction ($\bar{L}_{\text{perpendicular}}$) is used to estimate plate thickness, t_B [43]:

$$\bar{L}_{\text{perpendicular}} = \frac{\pi}{2} t_B \quad \text{(Equation 25)}$$

The interphase surface area per unit volume, S_V is [44]:

$$S_V = V_B / t \quad \text{(Equation 26)}$$

V_B : volume fraction of bainitic ferrite

1.3 Hydrogen in austenite

As mentioned before, hydrogen has negligible diffusivity in austenite and much higher solubility in austenite than in ferrite. Therefore, many expected austenite to behave like hydrogen traps. It has been shown that the hydrogen solubility in martensitic steels increases due to the presence of retained austenite [45] and such increase follows a linear relationship with the amount of retained austenite [46]. However, it is still debatable whether retained austenite itself or its interfaces with martensitic/bainitic ferrite is the main trapping entity [46] [47].

However, hydrogen embrittlement also exists in austenitic steels [48]. Hatano [49] charged and tensile tested 304 and 316 austenitic stainless steels. Both of the steels exhibited hydrogen enhanced strain-induced vacancies (HESIV) formation, and 304 exhibited significant reduction in toughness. 316, however, suffered less from HESIV and experienced no reduction in toughness. This embrittlement phenomenon has been ascribed to the instability of austenite to martensitic transformation. The discrepancy in toughness reduction between 304 and 316 was ascribed to the difference in their stack-fault energy (SFE). Martensite is formed via a faulting process which has a corresponding SFE. For n number of atomic planes, such SFE, γ_{SF} ($J m^{-2}$) is [50]:

$$\gamma_{SF} = n\rho(\Delta G^{chem} + E^{strain}) + 2\sigma_{int} \quad \text{(Equation 27)}$$

ρ : atom density in a close-packed plane ($mol m^{-2}$), ΔG^{chem} : molar chemical free energy difference between austenite and martensite, E^{strain} : molar coherency energy, σ_{int} : austenite/martensite interfacial energy

A low γ_{SF} value means that martensitic transformation is more likely to happen since little driving force is required. γ_{SF} in 304 is around $2 mJ m^{-2}$, compared with around $30 mJ m^{-2}$ for 316. This means 304 is less stable and it forms martensite easily which is much more susceptible to hydrogen embrittlement than austenite. This theory was further explored and supported by Ryu [51] [52], who compared γ_{SF} , austenite stability and embrittlement properties between TWIP and TRIP steels.

As shown in figure 1.4, since martensite formation will create a lot of new surfaces and internal stress etc., a critical driving force of around 1000 J mol^{-1} [53] is required for the transformation to take place. This is usually achieved via undercooling $\Delta G_{\text{undercooling}}$. However, this driving force can also be partially provided by deformation $\Delta G_{\text{deformation}}$, and less undercooling will be required $\Delta G_{\text{undercooling}}' = \Delta G_{\text{undercooling}} + \Delta G_{\text{deformation}}$ ($\Delta G_{\text{deformation}}$ is negative). This shifts M_s to M_s' . If an austenitic material is stable at temperature T , applying such deformation will induce martensitic transformation.

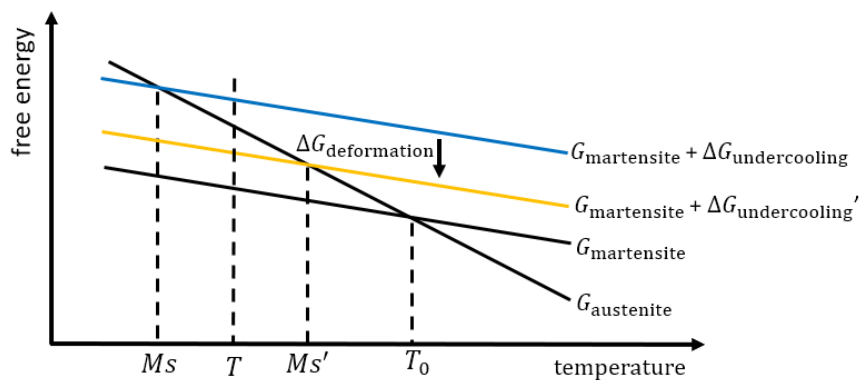


Figure 1.4: Schematic of free energy change during deformation-induced martensitic transformation

On the other hand, it has been shown that hydrogen charging, by itself, can induce martensitic transformation in austenitic steels [54] and in retained austenite within martensitic steels [55]. A comprehensive study of hydrogen charging's effects on different austenitic steels by Rozenak [56] shows a clear correlation between the austenite stability and the amount of induced martensite. Both BCC/body-centered tetragonal (BCT) α' and hexagonal close packed (HCP) ϵ martensite can be formed. These martensitic phases do not form straight away, two intermediate hydride phases, HCP ϵ' and FCC γ , are observed first before they transform into martensite [57] [58] [59]. This hydrogen-induced phase transformation has also been explained using SFE: hydrogen is capable of lowering SFE [60]. However, these phase transformations were mostly found in samples charged under very high charging current and were more of a surface phenomenon rather than a bulk phase transformation.

1.4 Thermal desorption analysis

TDA is a commonly used technique to determine the hydrogen profile within a sample. By heating a sample at constant rate, hydrogen gradually dissociates from different sites and diffuse out of the sample. A schematic of the instruments is illustrated here in figure 1.5:

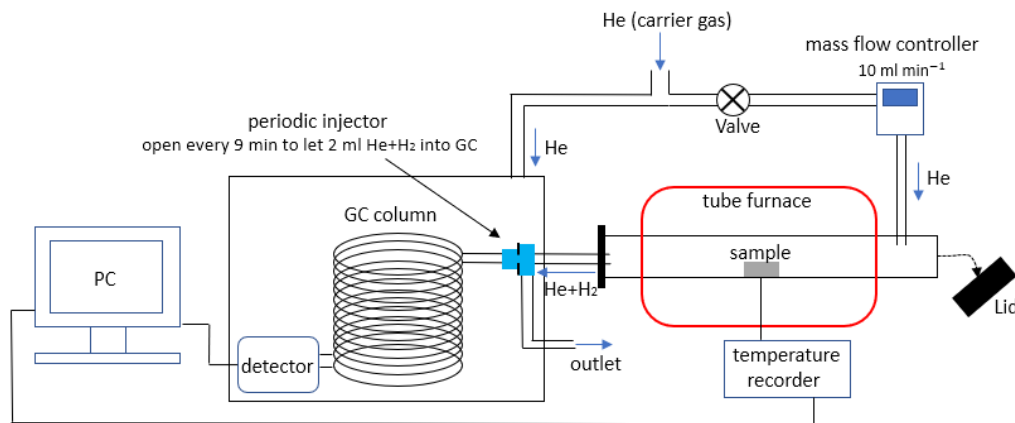


Figure 1.5: Schematic of the TDA set-up used in Cambridge

A standard He + H gas of known ratio was first used to calibrate the TDA. Different types of gas from the tube furnace were injected into the GC column and were accelerated, these gases can then be differentiated by the different time of flight for it to reach the detector at the end of the GC column, due to the difference in their molecular mass. TDA provides a spectrum of the desorption rate of the hydrogen from the specimen at different temperature. These different peaks on the spectrum help to identify hydrogen in various phases and trapping sites and their corresponding activation energy [61]. There are two stages in the desorption process: thermal dissociation and lattice diffusion. When thermal dissociation is the dominant step, the spectrum will only depend on heating. However, when lattice diffusion is the dominant step, the spectrum will also be highly dependent on sample size and geometry [29], which is undesired. In order to minimize the effects from lattice diffusion, small specimens and slow heating rate were used. In this case, the desorption rate can be related to temperature using the Kissinger's Equation [62]:

$$\frac{dx}{dt} = A(1-x)^n \exp\left(-\frac{E_a}{RT}\right) \quad \text{(Equation 28)}$$

x : fraction of hydrogen detrapped at time t , n : order of reaction, E_a : activation energy of the trap, A : constant

E_a is different for different types of traps. Therefore, their corresponding peak positions on the TDA spectrum will also be different. Under constant heating rate, the peak with maximum desorption rate will satisfy equation 29 [63]:

$$\frac{d}{dt} \left(\frac{dx}{dt} \right) = 0 = \left(\frac{\emptyset E_a}{RT^2} - A \exp \left(-\frac{E_a}{RT} \right) \right) \quad \text{(Equation 29)}$$

\emptyset : heating rate

The peak temperature T_C with maximum desorption rate satisfies:

$$\frac{\emptyset E_a}{RT_C^2} = A \exp \left(-\frac{E_a}{RT_C} \right) \quad \text{(Equation 30)}$$

Taking the logarithm and differentiating with respect to $(1/T_C)$ transforms equation 30 into:

$$\frac{d \ln(\emptyset/T_C^2)}{d(1/T_C)} = -E_a/R \quad \text{(Equation 31)}$$

Equation 31 is commonly applied to find E_a of various traps. Several TDA runs using different heating rate are performed on identical specimens under the same charging condition. A plot of $\ln(\emptyset/T_C^2)$ against $(1/T_C)$ is then made, from which the slope is used to determine E_a .

This setup can also be used to detect the natural degassing process of a specimen at room temperature without heating. This was also employed in this project. To better and more accurately capture the low temperature peaks (weak/reversible trapping sites), low temperature thermal desorption spectroscopy (LTDS) can be used [29], which can start the measurement from 70 K. However, in this project, the use of LTDS is not required.

1.5 Microprinting

Microprinting, is a good technique to correlate hydrogen distribution with microstructure at a microscopic level. Silver bromide is reduced to silver atom when it encounters hydrogen. This is the fundamental reaction of the microprinting technique, as shown in equation 32.



Microprinting can be used in two ways: to identify hydrogen-rich sites on a specimen surface, as in figure 1.6, and to identify fast diffusion path within a material, as in figure 1.7. The difference is that, for the latter, hydrogen is charged from the opposite side and hydrogen needs to diffuse to the microprinting surface to be detected. This project mainly employed the former.

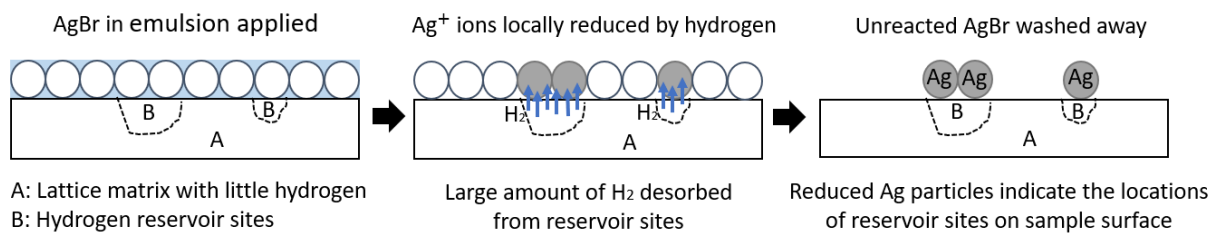


Figure 1.6: Illustration of microprinting technique used to identify hydrogen-rich sites

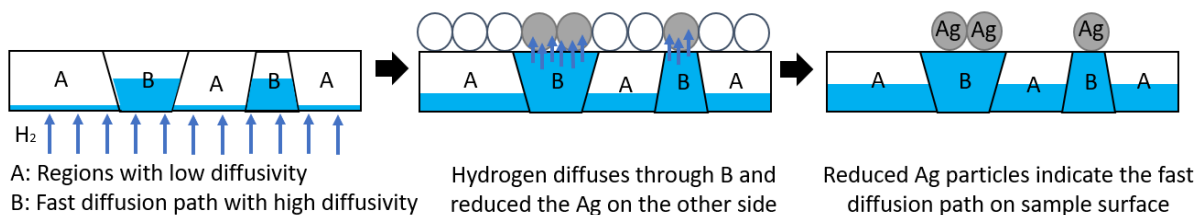


Figure 1.7: Illustration of microprinting used to identify fast-diffusion path

However, microprinting can only detect diffusible and weakly-trapped hydrogen on a sample surface. To identify stronger trap sites and to detect them underneath the surface or to have a bulk 3D profile, other visualization methods like tritium autoradiography, neutron tomography (NT) or scanning secondary ion mass spectroscopy (SIMS) [64] can be used.

2 Experimental method

2.1 Specimen preparation

Three types of austenite-containing steels were used: 2205 duplex stainless steel, 304 austenitic steel and a Nb-containing bainitic steel. They will simply be referred to as duplex steel, austenitic steel and bainitic steel in this report. Their compositions are listed in table 2.1:

	C	Mn	Si	Cr	Mo	Nb	P	S	Ni
duplex	0.017	1.45	0.39	22.61	3.28	0.001	0.018	0.001	5.17
austenitic	0.055	1.57	0.44	18.47	0.34	0.029	0.02	0.005	8.36
bainitic	0.21	2.0	1.9	0.54	0.52	0.019	0.0023	0.0007	N/A

Table 2.1: Chemical composition in wt % of the three types of steels used

The duplex steel was received as a hot rolled plate. No further heat treatment was performed. Rods of 8 mm in diameter were machined out along the transverse direction of the rolled plate. Each rod was then cut into 12-mm-long cylindrical specimens as shown in figure 2.1 (a).

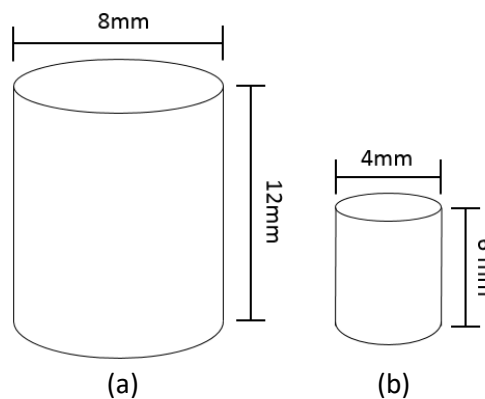


Figure 2.1: Standard test specimens used

The 304 austenitic steel was received as a cubic block. The block was annealed at 1050°C for 30 min then quenched in water. Smaller-sized cylindrical specimens, as shown in figure 2.1 (b), were machined out by electrical discharge machining (EDM).

The bainitic steel plate was received as-rolled. It was first homogenised at 1200°C for 48 h in an argon-environment furnace. Then, seven cycles of heat treatments were performed to reduce the prior austenite grain size in order to maximize the amount of retained austenite. Each cycle is a two-stage heat treatment as shown in Figure 2.2. Stage I is austenisation at higher temperature and stage II is ferrite/pearlite formation. For each cycle, the holding temperature and the time spent at each stage is different. These are collected in table 2.2.

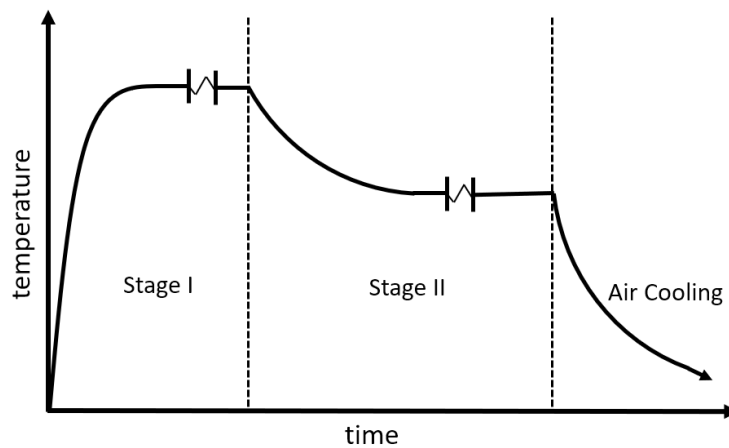


Figure 2.2: A heat treatment cycle for grain refinement in bainitic steel

Cycle no.	Stage I temperature	Stage I duration	Stage II temperature	Stage II duration
1&2	930 °C	3.5 h	620 °C	48 h
3	900 °C	3.5 h	620 °C	48 h
4	900 °C	3.5 h	610 °C	48 h
5	870 °C	3 h	610 °C	37 h
6&7	860 °C	3.5 h	610 °C	40 h

Table 2.2: Heat treatment cycles employed for grain refinement for the bainitic steel, the corresponding optical microscopic images showing this grain refinement progress are in appendix figure 6.1

The bainitic plate was then machined into long 8 mm diameter cylindrical rods. These rods were then austenised at 870°C for 1.5 h, and isothermally treated at 325°C for 1 h for bainitic transformation. Finally, each rod was cut into 12-mm-long cylindrical specimens as shown in figure 2.1(a).

2.2 Hydrogen charging

Four specimens were charged simultaneously as illustrated in figure 2.3. Before charging, each specimen was grinded using 800 and 2500 sand paper to achieve a smooth surface. They were then spot-welded onto a four-pronged stainless wire holder. Platinum wire was used as the counter electrode which curls around the inner wall of the glass beaker, fixed by a Teflon scaffold. The top surfaces of each specimen and the stainless-steel wire holder were painted with lacomit to prevent electrical contact with the charging solution.

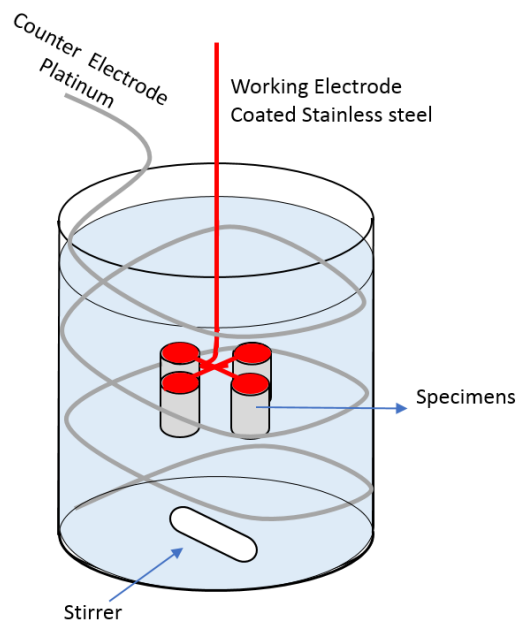


Figure 2.3: Hydrogen charging setup

A 3.5 wt % NaCl + 0.3 wt % NH_4SCN in water was used as the charging solution. A constant current density of 5 mA cm^{-2} was applied during charging. For longer charging time conditions, the solution was refreshed every two days, and each specimen's surface was re-grinded with 2500 sand paper to remove any compound which could potentially hinder hydrogen charging.

2.3 Compression

Compression was applied using an Instron low cycle fatigue machine to induce martensitic transformation in the specimens. Crosshead speed of 0.1 mm/s and 0.05 mm/s were used respectively for the 8 mm diameter and 4 mm diameter cylindrical samples to achieve a similar strain rate. Unless stated otherwise, most specimens in this project were compressed along their longitudinal directions to the machine limit of 95 kN. In this case, compression is used instead of tension to apply strain because it is compatible with the cylindrical sample shape which has been used in most of the previous TDA work in the group. In addition, it takes shorter time to set up compression tests. Therefore, changes in hydrogen desorption due to straining are more likely captured.

2.4 Metallography using optical microscopy

For optical microscopy, each specimen was grinded using 800, 2500 papers and polished with 6 μm , 3 μm and 1 μm polishing cloth. After being cleaned with distilled water and ethanol, different etchants were applied depending on the type of steel:

Duplex steel: 30 % oxalic acid was used to etch it electrolytically. As shown in figure 2.4, each specimen was immersed in the solution. A platinum wire was used as the counter electrode and a 316 stainless steel pin was used to make electrical contact with the sample surface. A constant potential of 3 V was applied for 15 to 20 s.

Austenitic steel: 70 % nitric acid was used to etch it electrolytically. The same setup in figure 2.4 was used. A constant potential of 2 V was applied for around 10 s.

Bainitic steel: etching was done by wiping the sample surface three to four times with a cotton cloth soaked with 2 % nital.

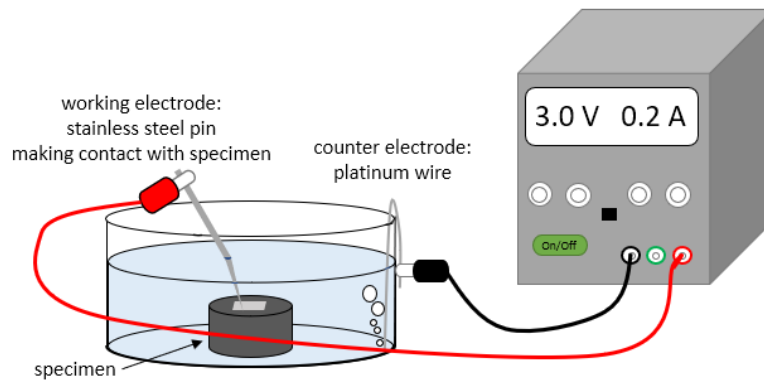


Figure 2.4: Electrochemical etching setup

2.5 Scanning electron microscopy

Each scanning electron microscopy (SEM) specimen was grinded, polished and etched as described in section 2.4. It was then fixed onto an aluminium stub using carbon tape and placed onto the SEM sample stage. All images were acquired using the Nova NanoSEM. For both secondary and back scattering modes, an emission power of 15 to 20 kV and a spot size of 5.5 were used. EDX analysis was also performed.

2.6 X-ray diffraction

Each X-ray diffraction specimen was grinded using 800, 2500 papers and polished with 6 μm and 3 μm polishing cloth. It was cleaned with ethanol and then placed flat on a single-crystal silicon disk. A Bruker D8 Advance was used to scan 2θ from 38° to 126° with a step size of 0.025° , each step detection lasts for 192 s. High Score Plus was used for data fitting and phase fraction analysis. Each XRD peak is fitted using a pseudo-Voigt function. The March/Dollase model [65] was employed to fit any textured specimen with favoured or unfavoured directions. Unless stated otherwise, for compressed samples, each specimen was cut into two halves and the XRD was performed on the centre-plane which experiences the most deformation thus transformation across the specimen.

2.7 Hydrogen desorption analysis

Immediately after charging, each specimen was grinded with 2500 sand papers and rinsed with water and isopropanol. It was then weighed and installed into the tube furnace within the TDA setup. 15-min purging using helium carrier gas was applied to remove the air introduced during sample installation. Desorption detection usually starts around 20 min after hydrogen charging. Each desorption test comprises two parts: room-temperature desorption detection and constant-heating-rate TDA detection. These parts vary for different tests, as described in table 2.3:

Test type	Room-temperature hydrogen desorption	Constant-heating-rate TDA
As charged	5 h	
Effect of compression	5 h, compression, then another 2 h	50 °C h ⁻¹ , from 25 °C to 600 °C
Effect of aging	N/A	
Activation energy determination	N/A	50 °C h ⁻¹ , from 25 °C to 600 °C 100 °C h ⁻¹ , from 25 °C to 600 °C 200 °C h ⁻¹ , from 25 °C to 600 °C

Table 2.3: Hydrogen desorption detection processes for different types of tests

For ‘effect of compression’ tests, after 3 h of detection at room temperature, the test specimen was taken out of the TDA setup and compressed. It was then reinserted into the setup and purged with helium for another 10 min. This whole process usually took around 15 to 20 min. The specimen’s room-temperature desorption was then further detected for another 2 h before the ‘constant-heating-rate TDA’ started. For ‘effect of aging’ tests, unless stated otherwise, each aged specimen was aged for the same amount of time as its charging time. For example, the specimen charged for 16 d was also aged for another 16 d before desorption detection.

2.8 Microprinting

Thin disks of 2 mm cut from the test rods in figure 2.1 (a) were used for microprinting. The backside of each disk was welded with a stainless steel wire, the frontside of the sample was grinded and polished to 1 μm and etched as described in section 2.4. Lacomit was used to paint the specimen leaving only the frontside exposed (for diffusion path tests, the backside was left exposed). Hydrogen can easily diffuse through Lacomit. However, in this case, lacomit can prevent water contact with the painted metal surfaces reasonably well thus prevent hydrogen generation via water reduction reaction. Each specimen was then charged individually in a similar setup as described in section 2.2. After charging, both the paint and the wire were removed. The sample was transferred to the dark room. Meanwhile in the dark room, 2 g of ArBr emulsion was placed in a small beaker with 4 ml of 5 wt % NaNO_2 solution. The mixture was stirred and heated on a hotplate maintained at 40°C for 20 min.

In the dark room, the sample surface was first covered with the mixed AgBr emulsion via wire looping method as shown in Figure 2.5, then Then left for 40 min. After that, the specimens were dipped into formalin (40 wt % HCHO) for 3 s to harden the gelatin layer and were immediately immersed in a fixing solution (15 wt % $\text{Na}_2\text{S}_2\text{O}_3$ + 10 wt % NaNO_2) for 5 min to remove the unreacted AgBr. Finally, the sample surface was rinsed with water and ethanol. SEM was used to examine the surface.

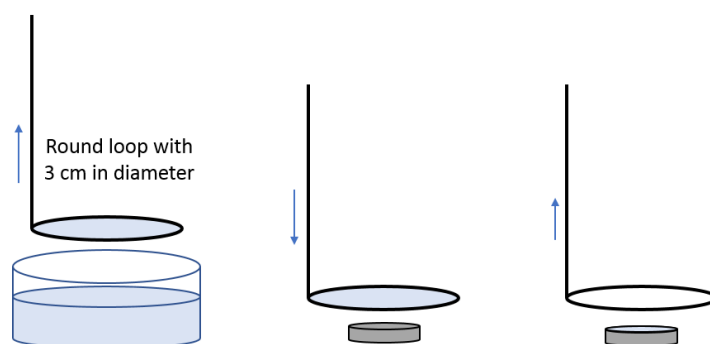


Figure 2.5: Wire looping method for applying AgBr emulsion

3 Results and Discussion

3.1 Starting material characterisation

3.1.1 Duplex steel

The microstructure of the duplex steel consists of austenite grains in a matrix of δ ferrite as marked in figure 3.1.

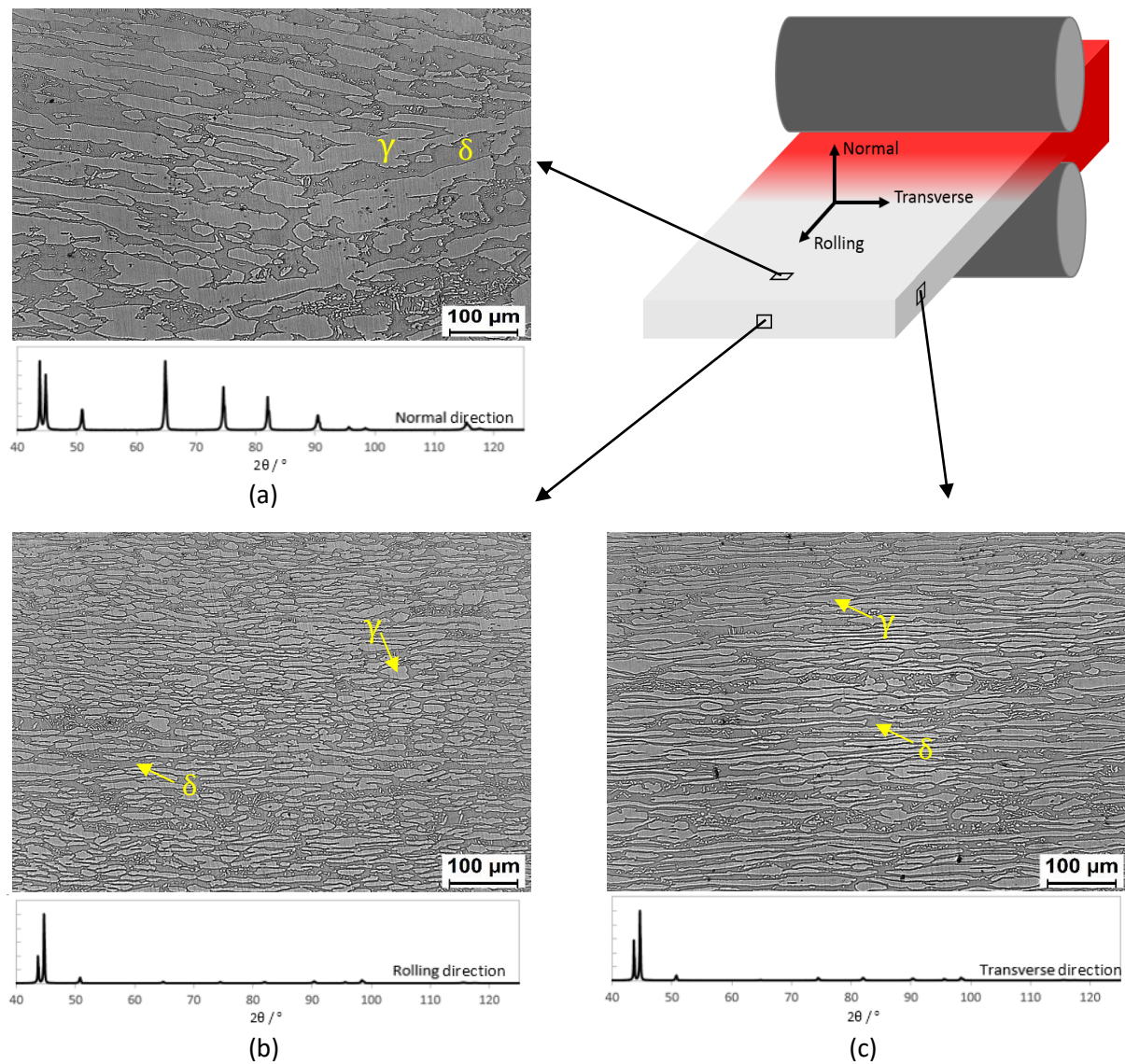


Figure 3.1: Optical microstructure images and normalized (maximum peak as 1) XRD results of the as-received duplex stainless steel from different directions: (a) normal direction, (b) rolling direction, (c) transverse direction, the corresponding normalized logarithm XRD results are in appendix 6.4

These austenite grains elongate along both rolling and transverse directions, more along the rolling direction. In figure 3.1, significant difference was found among the XRD spectra measured from different directions of the steel plate. This is compiled in figure 3.2.

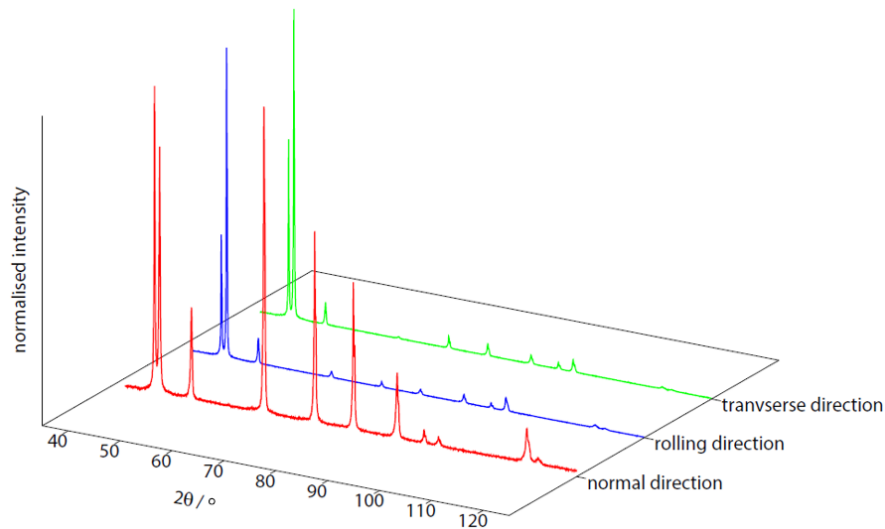


Figure 3.2: Compiled XRD results from three directions of the duplex steel

This difference is due to the texture effect, which resulted from deformation, in this case, hot rolling. During deformation, the crystallographic orientations are no longer fully random, grains reorientate themselves to accommodate the stress environment. Some crystallographic directions become favourably/unfavourably aligned with respect to the straining direction, so the magnitude of their corresponding XRD peak will be different for different directions. However, as shown in table 3.1, the phase fraction values obtained from XRD are the same when the texture is taken into account.

Direction	Ferrite fraction	Austenite fraction	Ferrite March/Dollase direction	Austenite March/Dollase direction
Normal	0.42 ± 0.03	0.58 ± 0.04	favoured: 121 & 010	favoured: 011 & 010
Rolling	0.41 ± 0.02	0.59 ± 0.03	favoured: 011 & 010	favoured: 111 & 010
Transverse	0.41 ± 0.02	0.59 ± 0.03	favoured: 011, unfavoured: 010	favoured: 111, unfavoured: 010

Table 3.1: Phase fraction analysis for different directions of the duplex steel. The corresponding fittings are in appendix 6.11

A bimodal austenite grain size distribution can be more clearly observed in SEM, as marked in figure 3.3. Secondary γ grains are much smaller and unlike primary γ grain, secondary γ grains do not preferentially elongate along the rolling direction. This suggests that these grains were formed at lower temperature and were most likely formed after hot rolling.

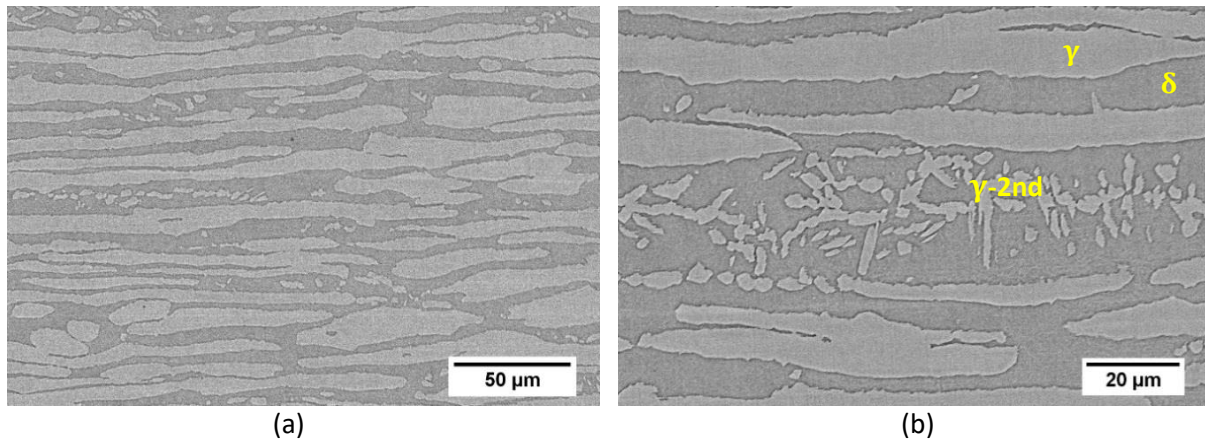


Figure 3.3: SEM images of the duplex steel from transverse direction at different magnification

Using the linear intercept method, and applying equation 20, 23 and 24 from section 2, together with the phase fraction results from table 3.1, the mean grain size of primary austenite along different direction can be characterized, the details are in appendix 6.23:

$$\bar{L}_{\text{Rolling}} = 63.0 \pm 10 \mu\text{m}, \bar{L}_{\text{Normal}} = 8.3 \pm 0.8 \mu\text{m}, \bar{L}_{\text{Transverse}} = 30.55 \pm 10 \mu\text{m}$$

3.1.2 Austenitic steel

All austenite grains became equiaxed after 30 min annealing at 1050 °C, as shown in figure 3.4. Transgranular elongated features can be seen for direction 2 and 3, as indicated with red arrows. (Direction 1, 2 and 3 are arbitrarily defined from the as-received cubic sample) These features were later identified as δ ferrite using SEM-EDX. For direction 1, δ ferrite grains are not elongated.

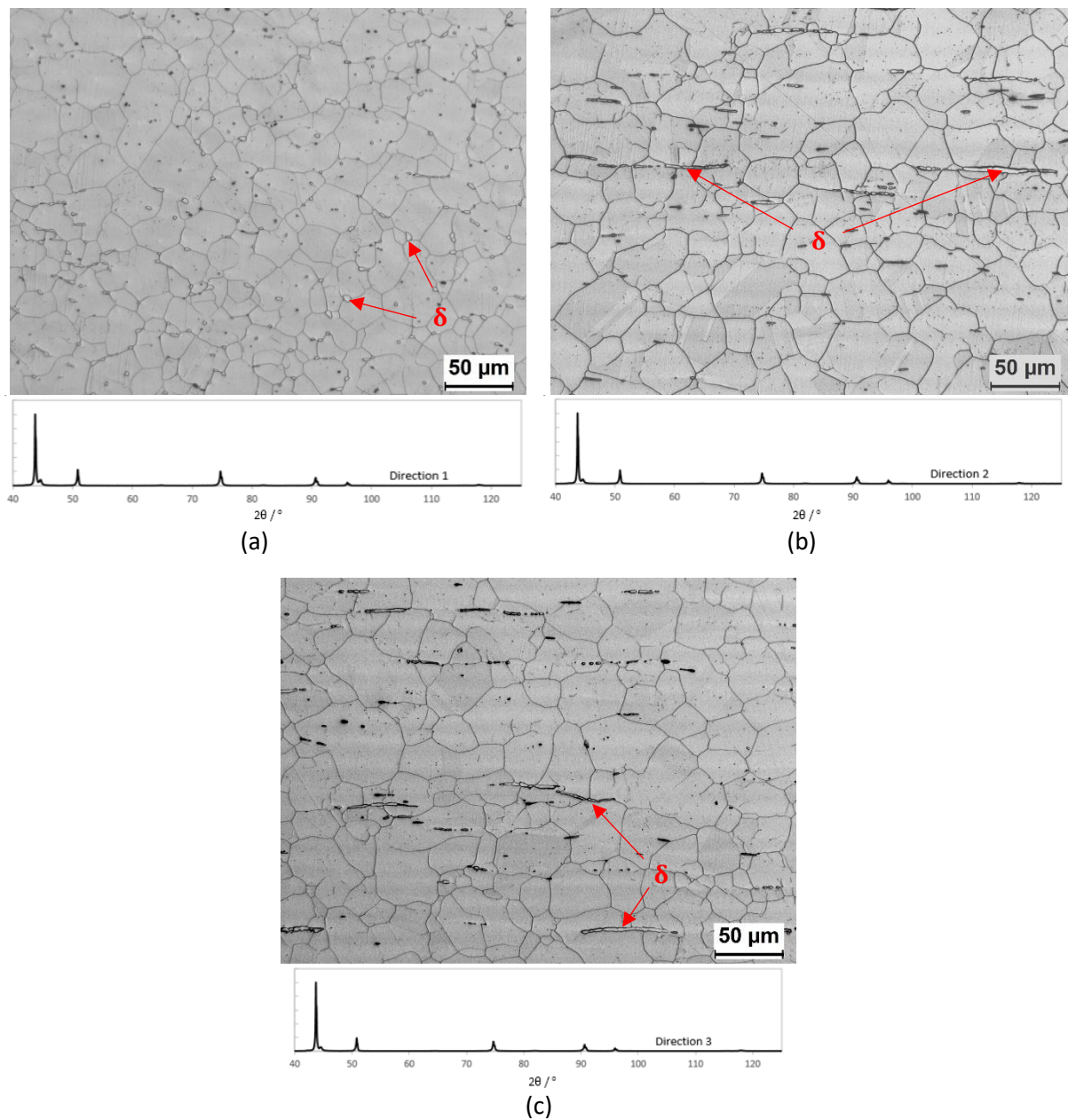


Figure 3.4: (a) –(c) Optical microstructure images and normalized XRD results of the as-annealed austenitic steel from three orthogonal directions (a) direction 1, (b) direction 2, (c) direction 3, these are arbitrarily defined directions from the as-received cubic sample, the corresponding normalized logarithm XRD results are in appendix 6.5

Little texture in the austenite was observed from XRD results, as compiled in figure 3.5, where no significant difference was found among spectra for different directions.

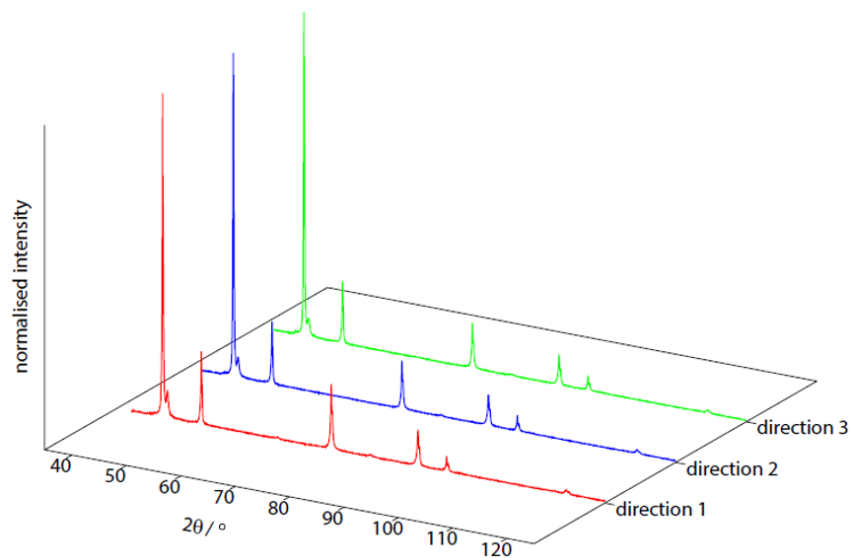


Figure 3.5: Compiled XRD results from the three directions of the austenitic steel

XRD was also performed on a 4 mm diameter sample from direction 3 for better future comparison since most of the later XRD on austenitic steel specimens were performed on 4 mm diameter samples. Overall, specimen size does not significantly affect XRD or the phase fraction obtained from it, this is shown in table 3.2. However, in normalized logarithm plots, as shown in figure 3.6, due to the higher background/intensity ratio in the smaller specimen's spectrum, some peaks seem reduced. For example, γ (400) and α (200) peaks of the 4 mm diameter specimen can barely distinguish themselves from the background.

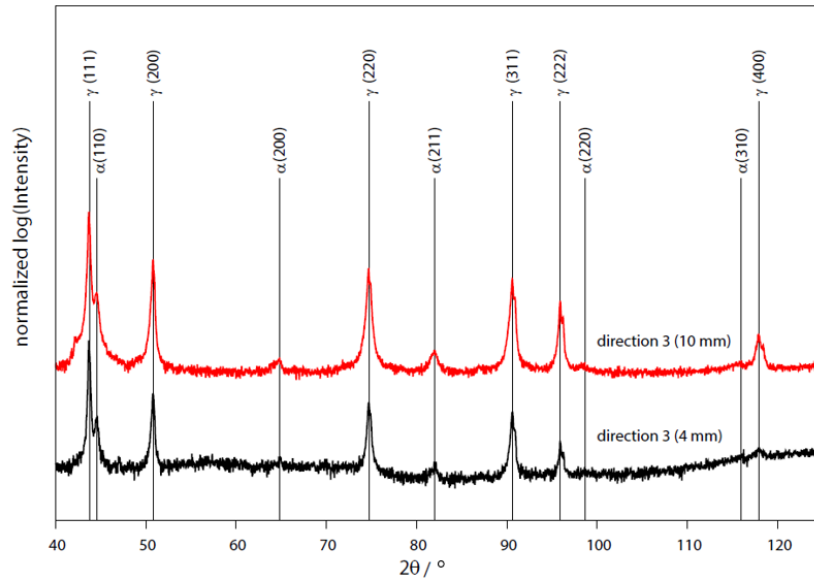


Figure 3.6: Comparison of normalized logarithm XRD from direction 3 of as-homogenized austenitic steel between a 10 mm side-length square sample and a 4 mm diameter circular sample

Direction	Ferrite fraction	Austenite fraction	Ferrite March/Dollase direction	Austenite March/Dollase direction
1	0.09 ± 0.02	0.91 ± 0.05		
2	0.08 ± 0.01	0.92 ± 0.05		
3	0.07 ± 0.01	0.93 ± 0.05	N/A	unfavoured: 010
3 (4 mm)	0.07 ± 0.01	0.93 ± 0.02		

Table 3.2: Phase fraction analysis for different directions of the austenitic steel, the corresponding fittings are in appendix 6.12

A small amount (less than 0.1) of ferrite is present in this austenitic steel, as shown in table 3.2. This is in accordance with other 304-related work [66] and further proves that the elongated features in figure 3.4 are ferrite grains. Measurements from different directions give the same phase fraction, as expected.

Two typical features of 304 austenitic steel are shown in figure 3.7: annealing twins and δ ferrite. Two annealing twins within an austenite grain are indicated by yellow arrows in (a). δ ferrite grains, as indicated by red arrows in (b), are the elongated features in figure 3.4. A small ferrite grain was magnified and EDX was performed as shown in (c) and (d). The higher Cr content within the feature confirms that it is δ ferrite. These ferrite grains are attributed to segregation that is present after the limited homogenization.

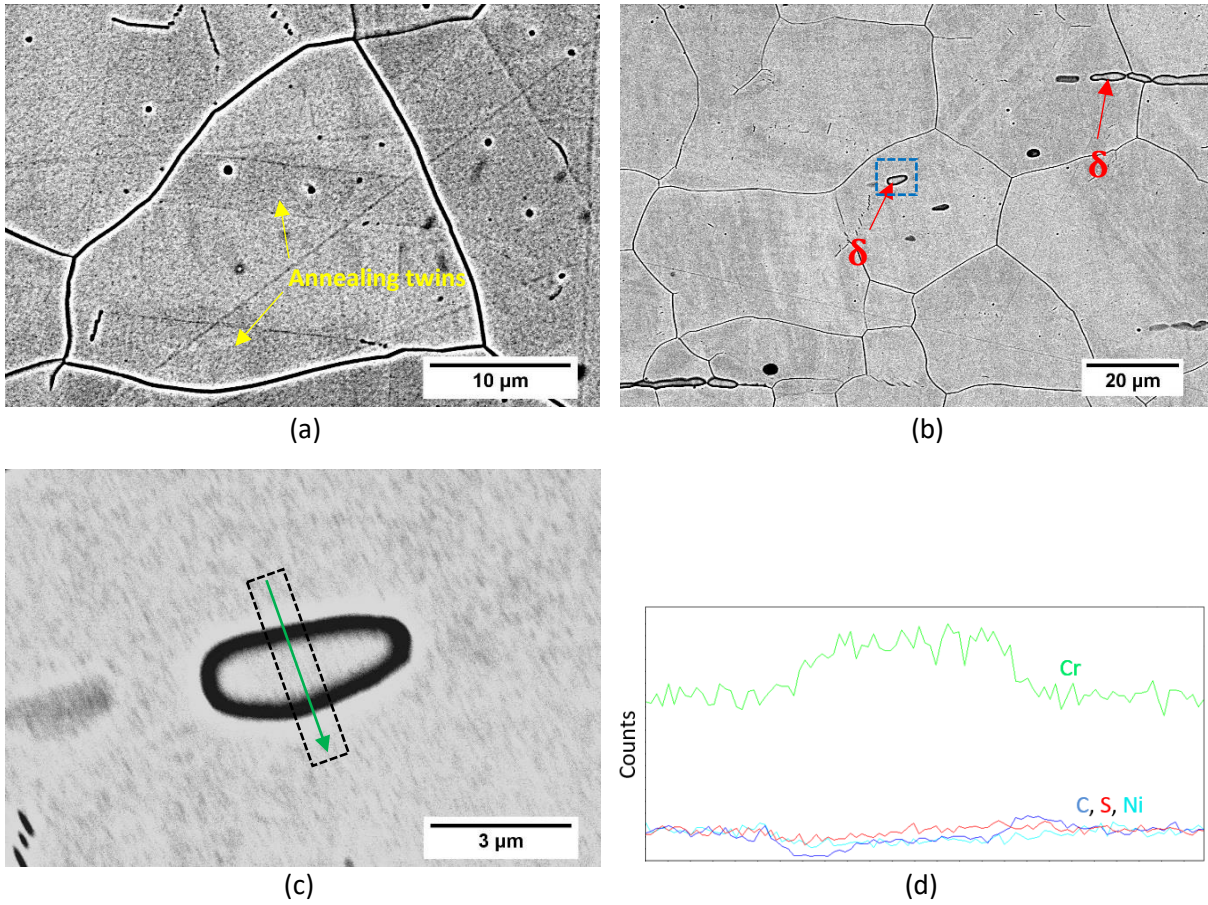


Figure 3.7: SEM images of the austenitic steel: (a): annealing twins inside an austenite grain, (b): delta ferrite, (c): magnified image from the dotted blue box in (b), (d): EDX line scan following the green arrow in (c)

From the linear intercept method, by applying equation 20 and 23 from section 2, the grain size can be characterized, the details are in appendix 6.24:

$$\bar{L}_{\text{average}} = 26.9 \pm 2 \mu\text{m}$$

3.1.3 Bainitic steel

Bainitic ferrite plates are the main constituent of the microstructure of the bainitic steel, as shown in figure 3.8. Some blocky retained austenite was also observed, indicated by the yellow arrows. This correlates well with the XRD spectrum in figure 3.9 and the phase fraction obtained from it, as shown in table 3.3, showing the material contains only around 10 vol% of austenite.

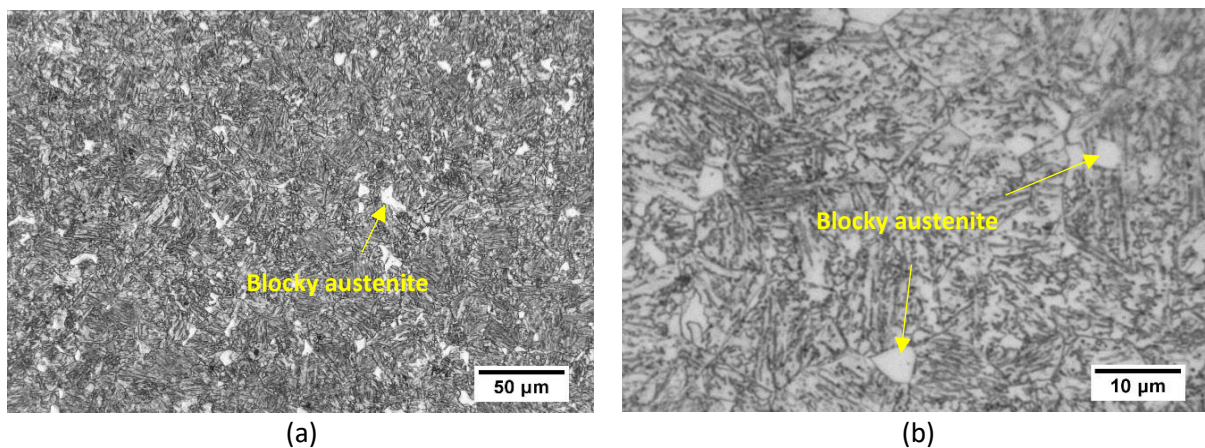


Figure 3.8: Optical microstructure images of the as-prepared bainitic steel

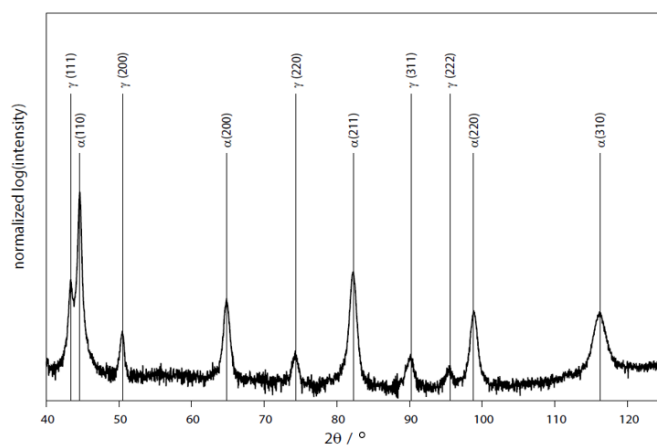


Figure 3.9: Normalized logarithm XRD of the as-prepared bainitic steel

Phase analysis based on XRD was performed:

Direction	Ferrite fraction	Austenite fraction	Ferrite March/Dollase direction	Austenite March/Dollase direction
N/A	0.90 ± 0.02	0.10 ± 0.04	N/A	N/A

Table 3.3: Phase fraction analysis for the bainitic steel, the corresponding fittings are in appendix 6.13

SEM images in figure 3.10 also show that most of the microstructure consists of bainitic ferrite and film austenite, a magnified image of this feature is shown in figure 3.10 (c). Film austenite is the retained austenite between bainite plates, enriched in carbon content due to bainitic transformation around it and therefore stabilized. Blocky austenite was also observed as marked with yellow arrows in (b). A magnified image of a blocky retained austenite grain with smooth surface is in (d).

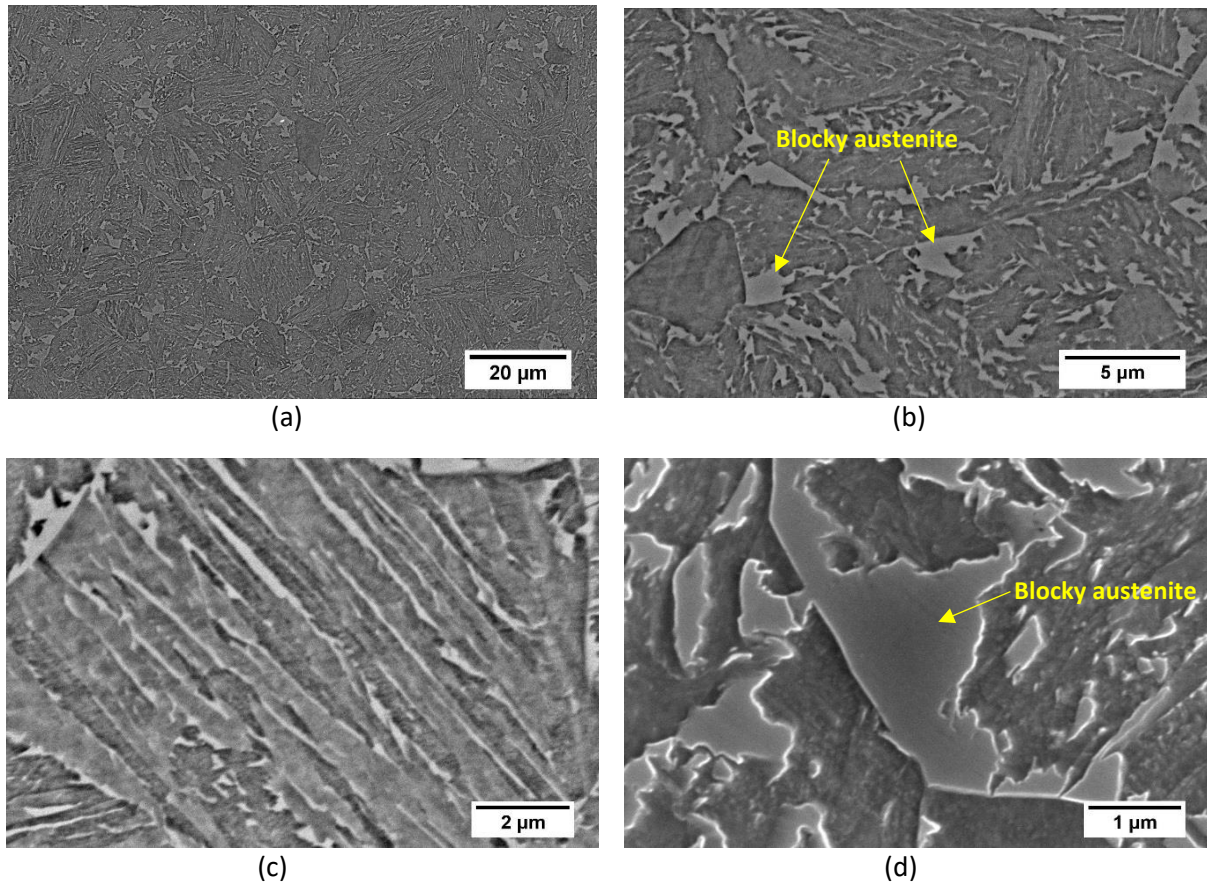


Figure 3.10: SEM images of the as-prepared bainitic steel. (a) & (b): overviews of microstructure at lower magnifications, (c): Bainite plates and film austenite, (d): blocky retained austenite

Using the linear intercept method and applying equation 25 from section 2, the bainite plate thickness t can be obtained, the details are in appendix 6.25:

$$t = \frac{2}{\pi} \times \bar{L} = 0.32 \pm 0.03 \mu\text{m}$$

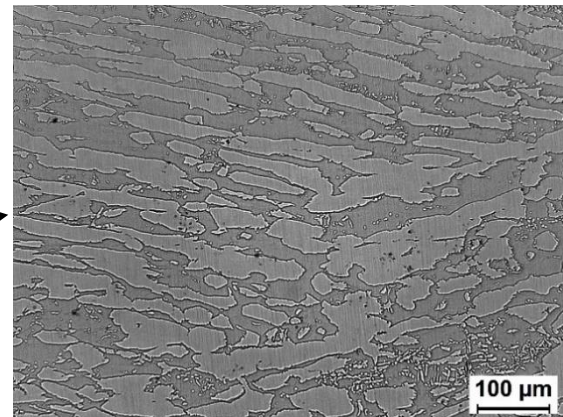
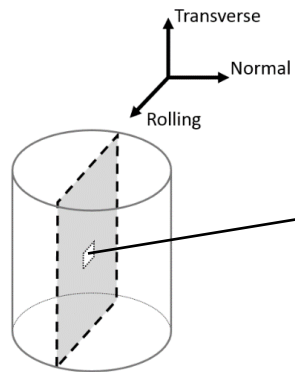
Further applying equation 26, the ferrite/austenite interphase surface area per unit volume, S_B , was found [44]:

$$S_V = \frac{V_B}{t} \approx 2.81 \times 10^6 \text{ m}^{-1}$$

3.2 Deformation-induced martensitic transformation

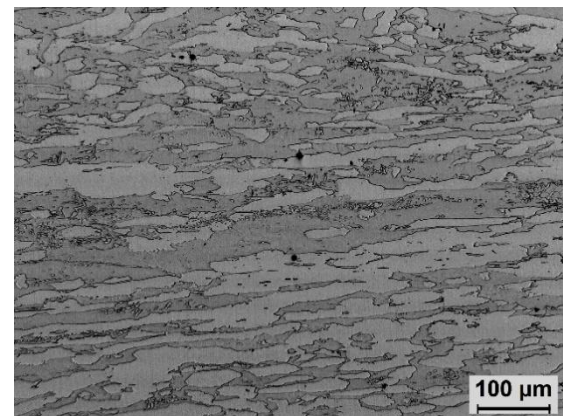
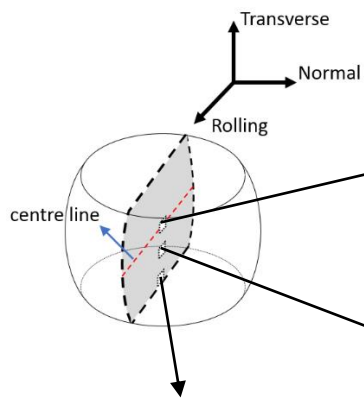
3.2.1 Duplex steel

Before Compression:

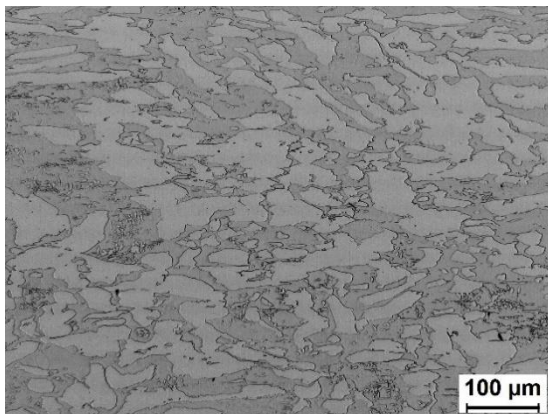


(a)

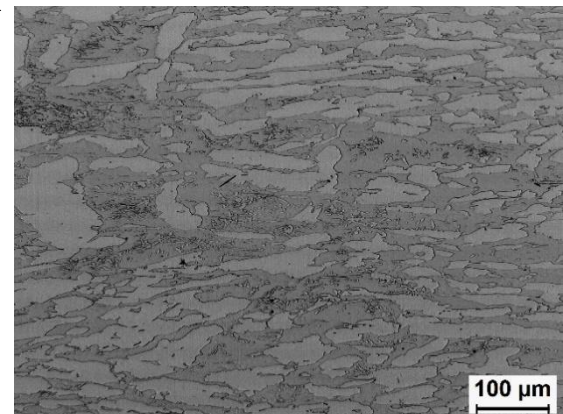
After Compression along transverse direction:



(b)



(c)



(d)

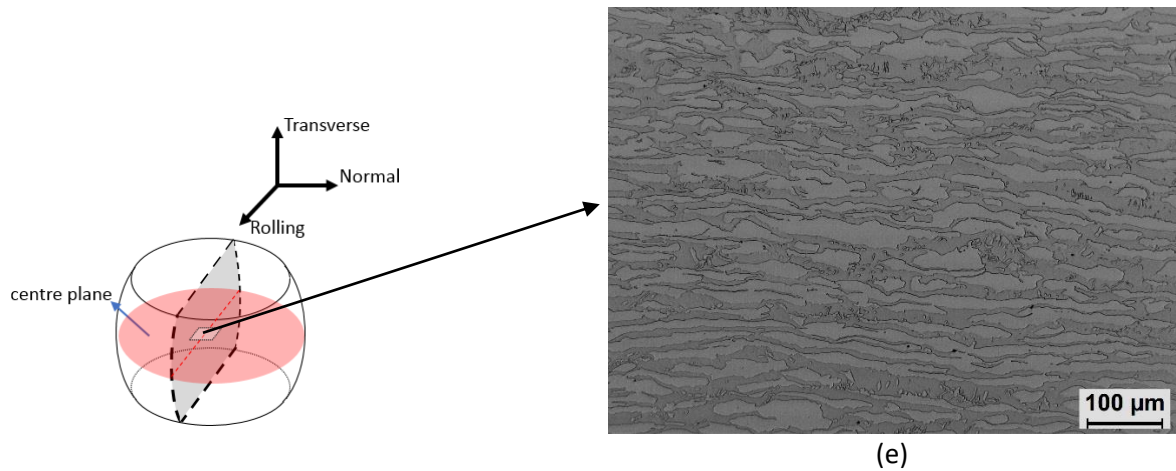


Figure 3.11: The microstructure of a duplex specimen before and after compression. (a) - (d) are images from the normal plane, (e) is an image from the transverse plane. (a): before compression, (b) & (e): centre of the compressed specimen, (c): bottom of the compressed specimen, (d): mid-way between bottom and centre of the compressed specimen

Each specimen was compressed along the transverse direction. The austenite grains experienced an overall reduction in the thickness in this direction. This can be seen clearly by comparing figure 3.11 (a) with (b). This change indicates that austenite grains experienced plastic deformation during compression. However, no other significant change in microstructure was observed. Macroscopically, rather than barrelling, duplex steel specimens tend to shear along the normal direction during compression, as shown in figure 3.12.

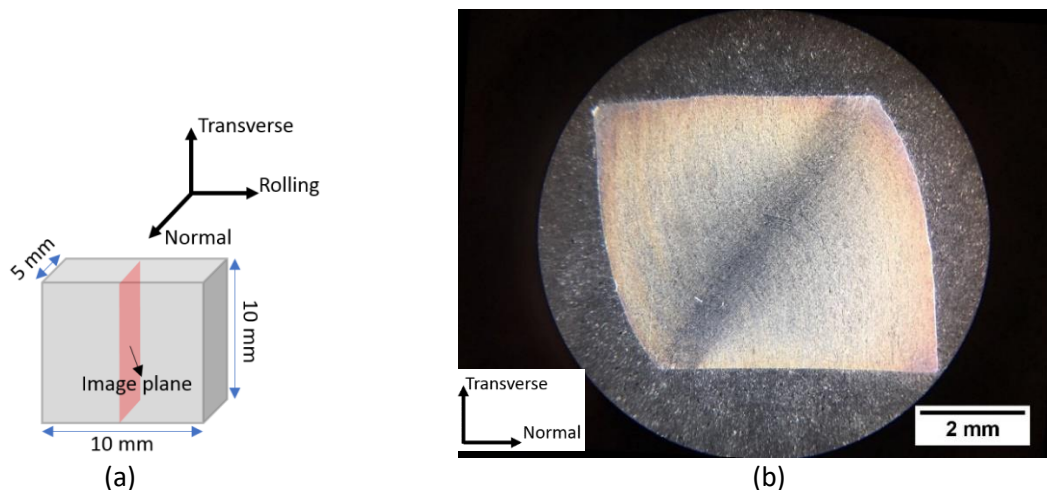


figure 3.12: Cross-sectional image of a duplex steel specimen of 5 mm x 10 mm x 10 mm after compression in the transverse direction (a) schematic of the specimen before compression (b) the crystallographic image of the cross-section of the specimen after compression (the red plane in (a))

XRD was performed on the centre transverse plane of the deformed sample, i.e. the plane marked red in figure 3.11. It is compared with that of the as-received transverse plane in figure 3.13:

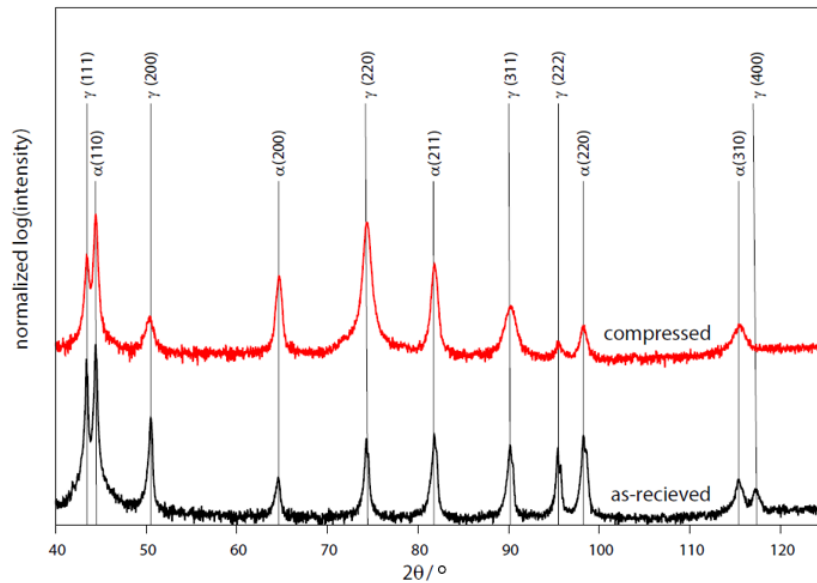


Figure 3.13: XRD of the as-received duplex steel before and after compression

Another as-received duplex steel specimen was dipped in liquid nitrogen for 15 min to see if there is any change in XRD. This is shown in figure 3.14. Any possible bainitic or martensitic transformation will manifest itself by showing an overall reduction in the relative intensity for peaks correspond to austenite while an overall increase in the relative intensity for peaks correspond to ferrite.

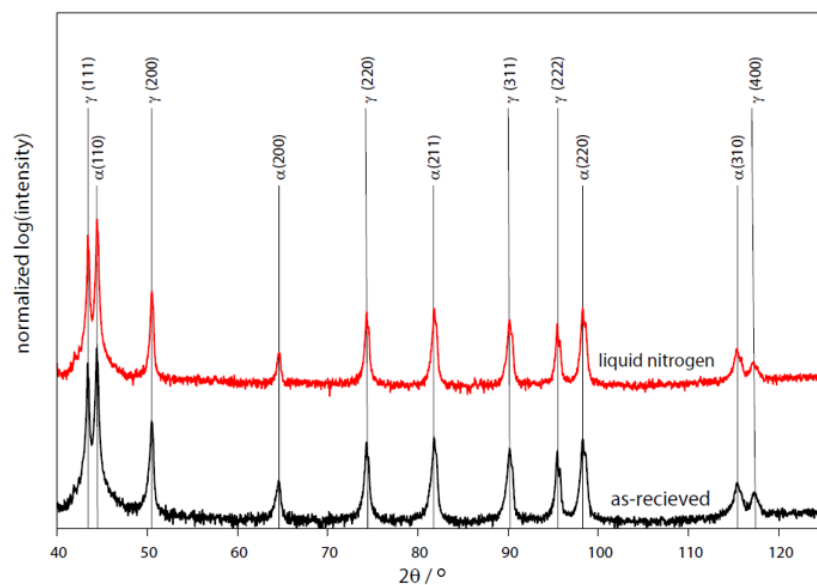


Figure 3.14: XRD of the as-received duplex steel before and after dipping in liquid nitrogen for 15 min

Figure 3.13 and 3.14 show that the XRD spectra changed significantly after compression, but nothing significantly changed after dipping in liquid nitrogen. Further quantification, as shown in table 3.4, indicates that the phase fraction does not change for either compression or liquid nitrogen quenching. This suggests no martensitic transformation took place in this duplex steel.

Condition	Ferrite fraction	Austenite fraction	Ferrite March/Dollase direction	Austenite March/Dollase direction
As-received	0.38 ± 0.02	0.62 ± 0.04	favoured: 011, unfavoured: 010	favoured: 111
compression	0.42 ± 0.04	0.58 ± 0.05	favoured: 121, 010	favoured: 011, unfavoured: 010
Liquid nitrogen	0.40 ± 0.02	0.60 ± 0.04	favoured: 011, unfavoured: 010	favoured: 111

Table 3.4: Phase fraction analysis for the duplex steel after compression and after liquid nitrogen quenching, the corresponding fittings are in appendix 6.14

SEM was also performed on the compressed specimens. No martensite was identified at the centre of the compressed specimen. This further confirms that there is no deformation-induced martensitic transformation.

3.2.2 Austenitic steel

Compared with figure 3.4, the deformed specimen, as shown in figure 3.15, does not have such smooth morphology. This attributes to the formation of slip bands and deformation-induced martensite. Slip bands were mostly observed at the less strained region, i.e. bottom of the compressed specimen, while martensite was observed at the more strained region. The difference in morphology between these two features can be seen at higher magnification by comparing figure 3.16 (a) and (b).

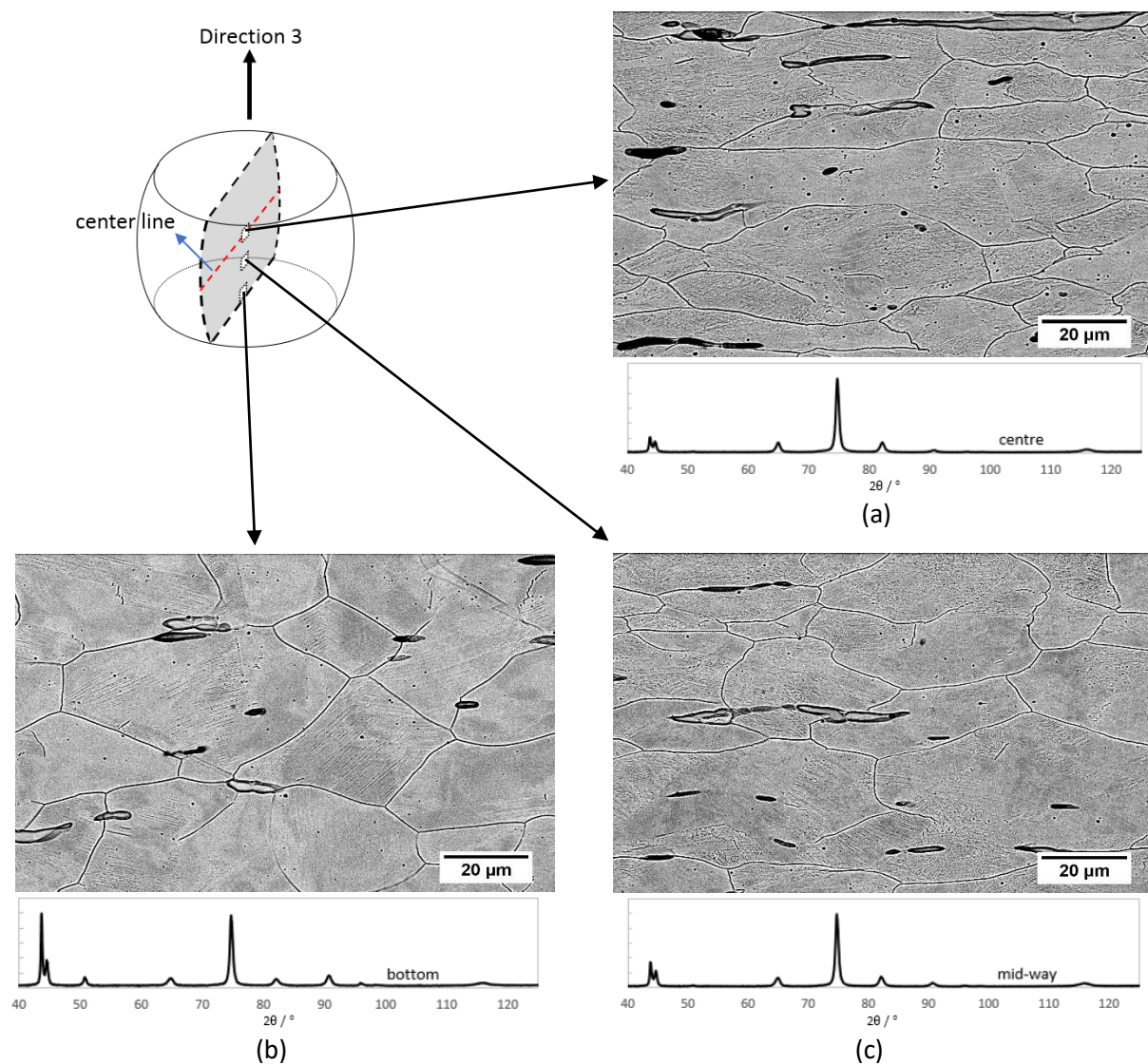


Figure 3.15: SEM microstructure images and corresponding XRD of an 8 mm diameter austenitic steel specimen before and after compression. (a): centre of the compressed specimen; (b): bottom of the compressed specimen; (c): mid-way between bottom and centre of the compressed specimen. The corresponding optical images are in appendix 6.3

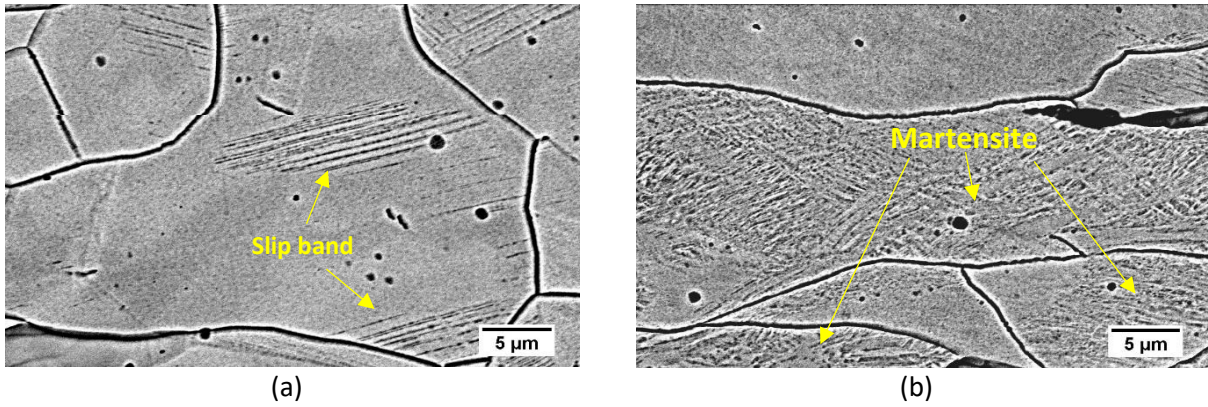


Figure 3.16: (a): slip bands formed in the lightly deformed region in the austenite specimen; (b): martensite formed in the heavily deformed region in the austenite specimen

XRD in figure 3.17 further confirms that compression can induce martensitic transformation in austenitic steel. More transformation was found towards the centre of the compressed specimen, where greater deformation was experienced.

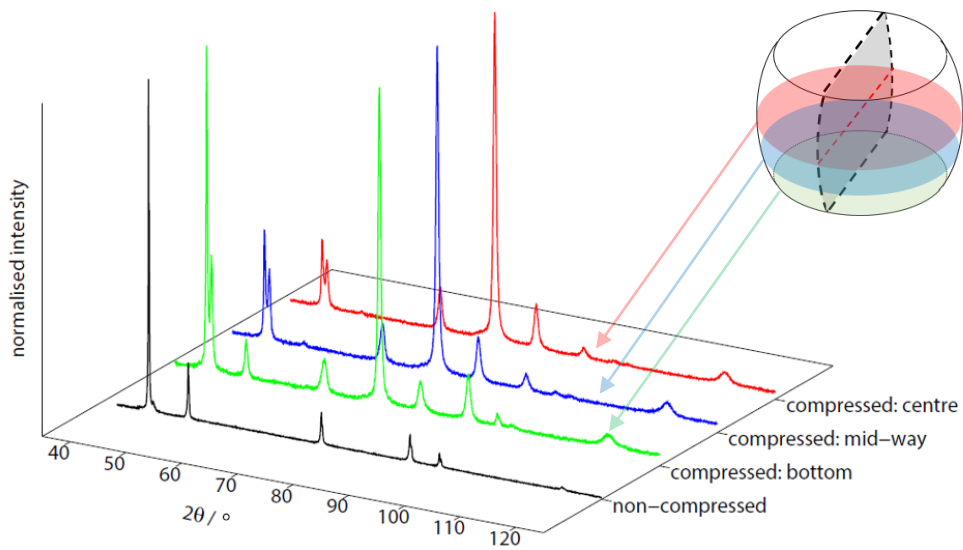


Figure 3.17: Compiled XRD results from figure 3.15 of different sections of a compressed 8 mm diameter austenitic specimen, its corresponding 2D normalized logarithm plot is in appendix 6.6

With the same total applied load, 4 mm diameter specimens were, as expected, more deformed than 8 mm diameter specimens after compression. 75 - 80 % reduction in length can be achieved. Figure 3.18 shows that, for the compressed 4 mm diameter specimen, almost all austenite has transformed into martensite in the centre of the specimen.

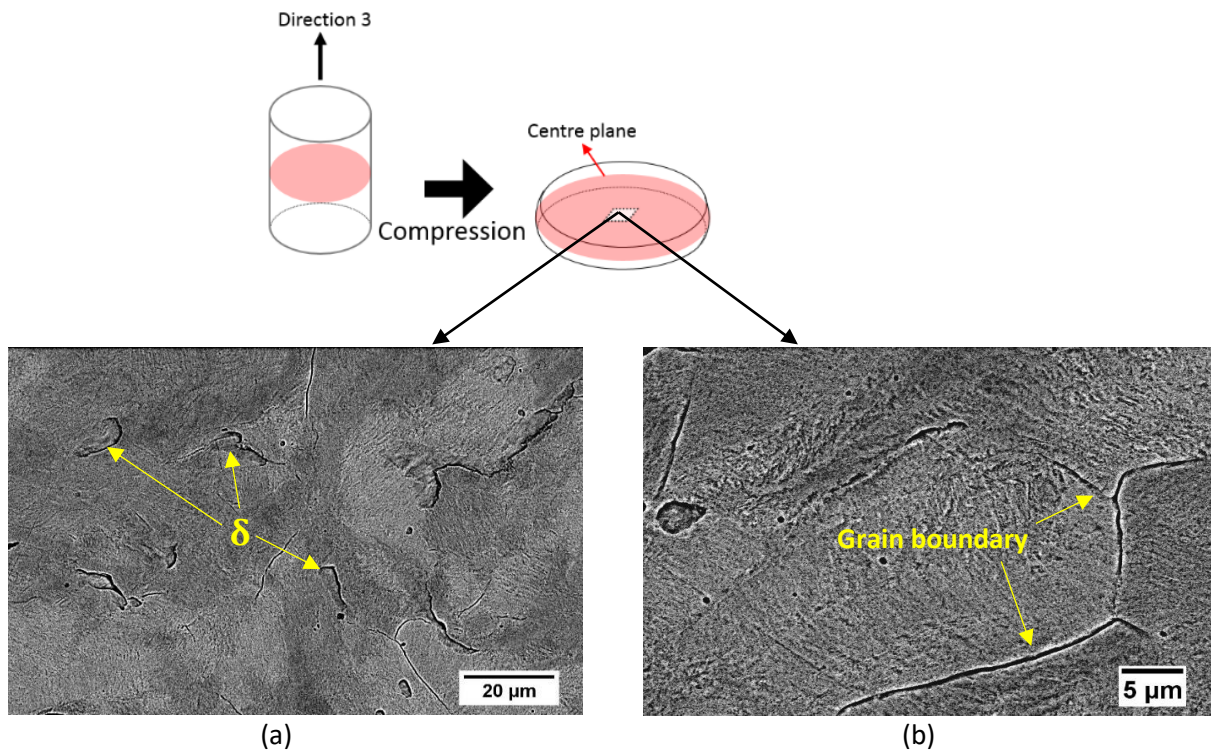


Figure 3.18: SEM microstructure images of a compressed 4 mm diameter austenitic steel specimen at different magnifications, the corresponding optical images are in appendix 6.3

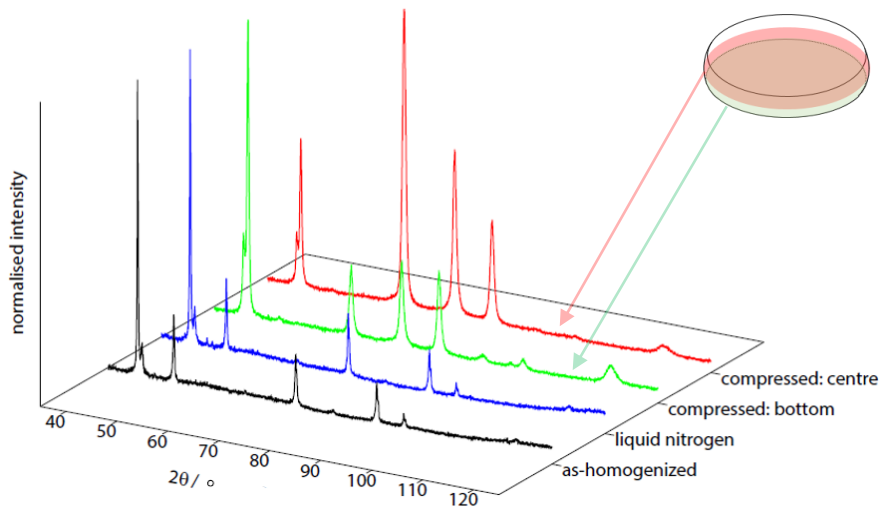


Figure 3.19: Compiled XRD results of 4 mm diameter austenitic specimens after compression or after quenching in liquid nitrogen, its corresponding 2D normalized logarithm plot is in appendix 6.7

Figure 3.19 shows the difference in the normalized XRD spectra of austenitic steels after being dipped in liquid nitrogen or after compression. The phase fraction obtained from it is shown in table 3.5. These correlate well with the previous SEM and optical images. Little transformation was found after dipping the specimen in liquid nitrogen. Compression, on the other hand, induces significant martensitic transformation. And the amount of transformation depends on the deformation experienced: 4 mm diameter specimens experience more transformation than 8 mm specimens and the transformation is more significant towards the centre of each compressed specimen.

Condition	Ferrite fraction	Austenite fraction	Ferrite March/Dollase direction	Austenite March/Dollase direction
8 mm as-homogenized	0.06 ± 0.03	0.94 ± 0.01		
4 mm as-homogenized	0.07 ± 0.01	0.93 ± 0.02	N/A	unfavoured: 010
4 mm liquid nitrogen	0.09 ± 0.01	0.91 ± 0.02		
8 mm compressed: bottom	0.18 ± 0.04	0.82 ± 0.01		
8 mm compressed: mid-way	0.33 ± 0.04	0.67 ± 0.01		
8 mm compressed: centre	0.44 ± 0.01	0.56 ± 0.01	favoured: 121, 010	favoured: 011, unfavoured: 010
4 mm compressed: bottom	0.57 ± 0.01	0.43 ± 0.02		
4 mm compressed: centre	0.82 ± 0.01	0.18 ± 0.03		

Table 3.5: Phase fraction analysis for 4 mm diameter and 8 mm diameter austenitic steel specimens after compression or after liquid nitrogen quenching, the corresponding fittings are in appendix 6.15

3.2.3 Bainitic steel

Compared with the smooth surface of the undeformed blocky retained austenite shown in figure 3.10 (d), deformation-induced martensite can be seen after compression in figure 3.20. Martensite-austenite constituents from partial transformation were also observed, as indicated in figure 3.20 (b), where the remaining retained austenite is marked with a red arrow. The difference in morphology between transformed and untransformed austenite can be distinguished well.

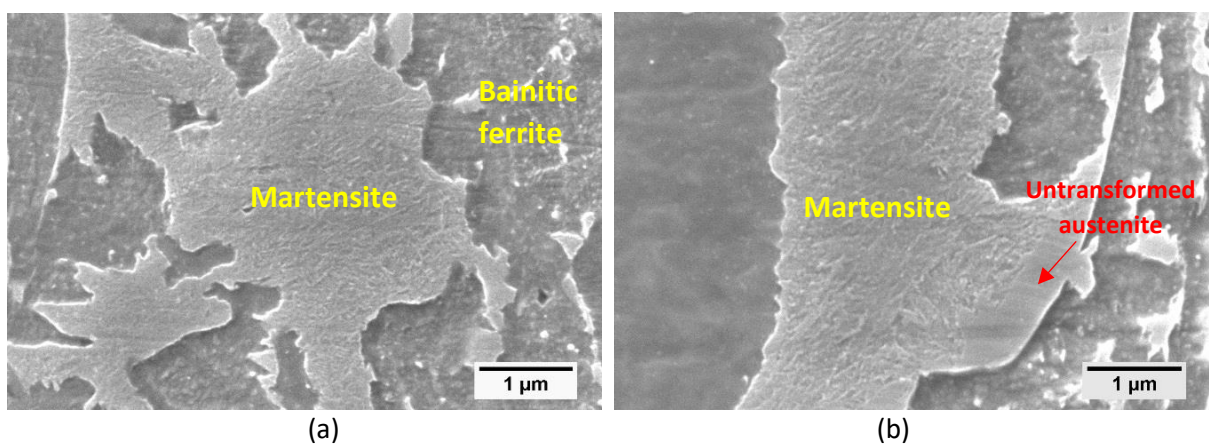


Figure 3.20: Deformation-induced martensite in a compressed bainitic steel specimen. (a): an almost completely transformed blocky retained austenite grain (b): a martensite-austenite constituent, partial martensitic transformation leaving some untransformed retained austenite

The situation for bainitic steel is similar to that for austenitic steel: liquid nitrogen does not induce significant phase transformation, yet compression does. And more martensite is formed towards the centre of the compressed specimen. This trend can be seen in figure 3.21 and the corresponding phase analysis is in table 3.6.

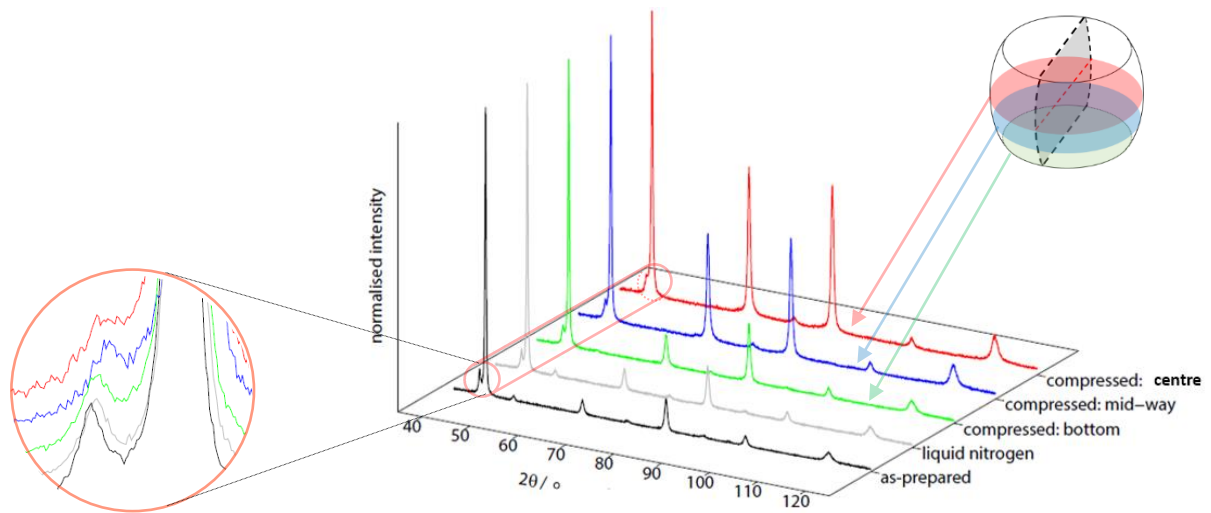


Figure 3.21: Compiled XRD results of bainitic specimens after compression or after quenching in liquid nitrogen

Condition	Ferrite fraction	Austenite fraction	Ferrite March/Dollase direction	Austenite March/Dollase direction
as-homogenized	0.90 ± 0.02	0.10 ± 0.04	N/A	N/A
liquid nitrogen	0.90 ± 0.01	0.10 ± 0.03	N/A	N/A
compressed: bottom	0.94 ± 0.05	0.06 ± 0.01		
compressed: mid-way	0.96 ± 0.01	0.04 ± 0.03	favoured: 121, 011	favoured: 110
compressed: centre	0.98 ± 0.01	0.02 ± 0.04		

Table 3.6: Phase fraction analysis for bainitic steel specimens after compression or after liquid nitrogen quenching, the corresponding fittings are in appendix 6.16 (the error range for each condition arises from the difference between the actual peaks and their fitting and was calculated by the software. Apart from the as-homogenized condition, in which case two specimens' XRD were performed, each condition only has one specimen tested)

3.3 The effect of hydrogen charging time

3.3.1 Duplex steel

Figure 3.22 and table 3.7 indicate no significant difference among the XRD of specimens charged for different times and the phase fraction obtained from them. This suggests that prolonged hydrogen charging does not induce any phase transformation in duplex stainless steel.

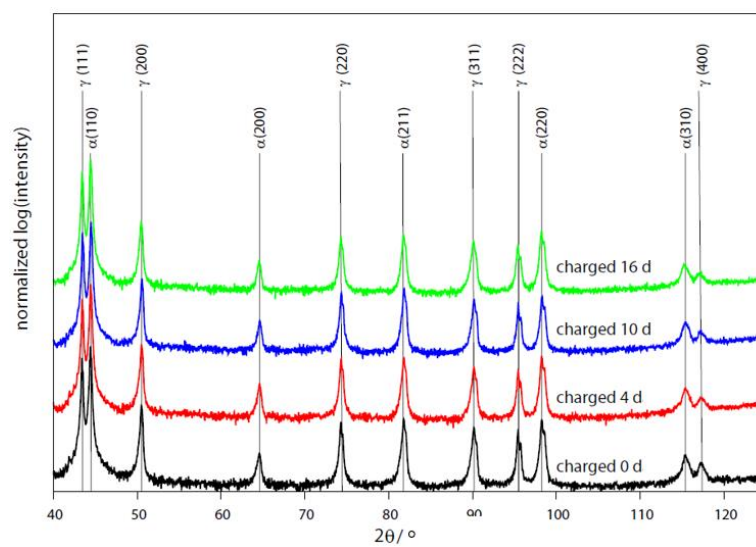


Figure 3.22: Normalized logarithm XRD plots for duplex steel specimens charged for different times

Condition	Ferrite fraction	Austenite fraction	Ferrite March/Dollase direction	Austenite March/Dollase direction
as-received	0.41 ± 0.02	0.59 ± 0.03		
charged 4 d	0.41 ± 0.02	0.41 ± 0.04	favoured: 011, unfavoured: 010	favoured: 111, unfavoured: 010
charged 10 d	0.42 ± 0.02	0.58 ± 0.04		
charged 16 d	0.40 ± 0.02	0.60 ± 0.04		

Table 3.7: Phase fraction analysis for duplex steel specimens charged for different times, the corresponding fittings are in appendix 6.17

Figure 3.23 (a) shows a typical room-temperature hydrogen desorption profile: The signal initially increases and reaches a maximum within 50 to 80 min, followed by a gradual decrease. The gradually decreasing trend is because, as the hydrogen content within the specimen decreases, the hydrogen concentration gradient reduces. Therefore, the hydrogen diffusion rate, i.e. the desorption rate also decreases, following Fick's Law.

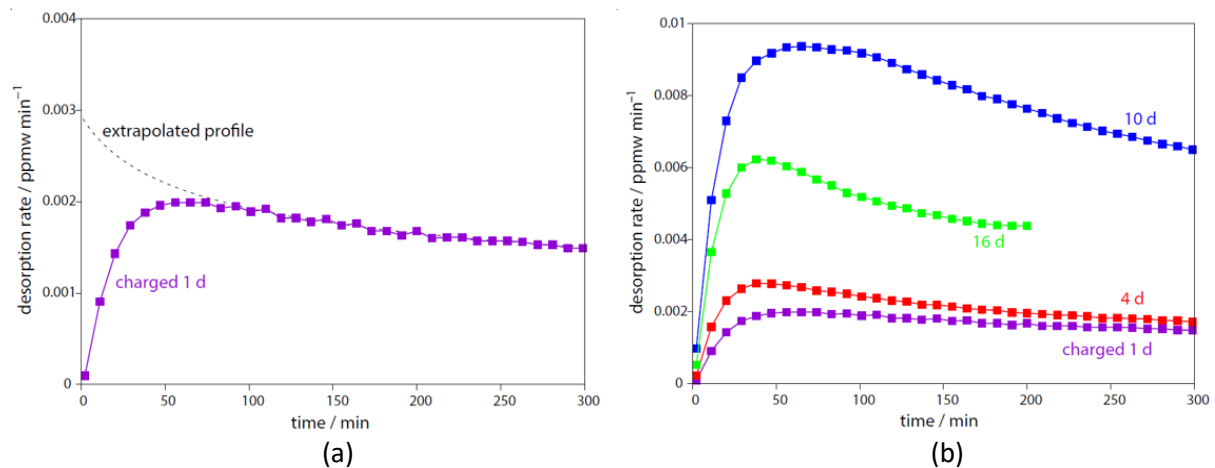


Figure 3.23: (a): detected and extrapolated room-temperature hydrogen desorption profile of a duplex steel specimen charged for 1 d, (b): compiled room-temperature hydrogen desorption spectra of duplex steel specimens charged for different times

However, the initial low desorption rate, starting from almost 0, deviates from this trend. This is due to the purging process. Purging largely removes and dilutes the existing hydrogen within the sample chamber. This purging effect gradually wears off as more hydrogen desorbs from the test specimen and the signal finally becomes stabilized after 50 to 80 min. The actual initial hydrogen desorption rate can be estimated by back-extrapolating the stabilized signal using a power law. This is shown as the dotted curve in figure 3.23 (a). This extrapolation method was also used to predict any future desorption rate at room-temperature. For example, based on the desorption profile of the first 3 h, the desorption rate after 10 h can be estimated. This will be demonstrated later for compressed specimens. Figure 3.23 (b) compares the room-temperature hydrogen desorption spectra of duplex steel specimens charged for different times. No strong correlation between charging time and room-temperature desorption rate was found in this case.

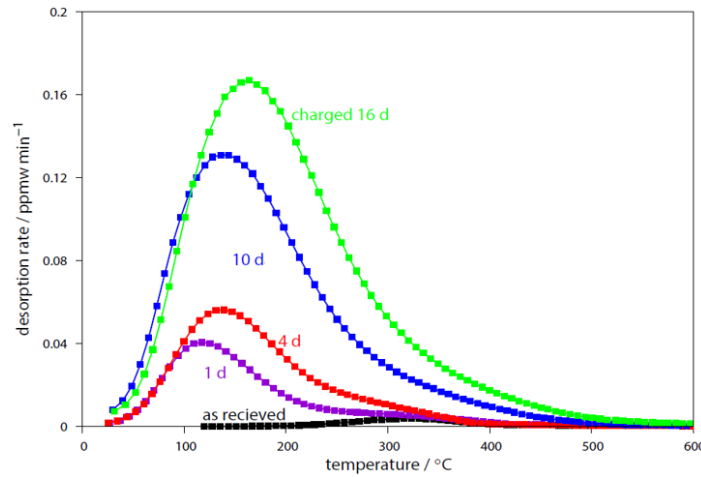


Figure 3.24: Constant-heating-rate TDA of duplex steel specimens charged for different times followed by aging at room temperature for 5.5 h

Each constant-heating-rate TDA spectrum contains a significant peak with a high-temperature tail. This indicates the existence of another high-temperature peak. This tail most likely arises from the irreversible traps within this material. The as-received specimen also contains this high-temperature peak, in which hydrogen could have been introduced and become trapped during the manufacturing and processing stages. Figure 3.24 shows that longer charging time introduces more hydrogen into the steel and shifts the main peak toward higher temperatures. This trend is plotted in figure 3.25. The peak shift indicates an overall shift of hydrogen to more energetically stable sites. This could either be because longer time allows hydrogen to diffuse around to get trapped at stronger trap sites or because longer time allows hydrogen to diffuse further into the austenite grains.

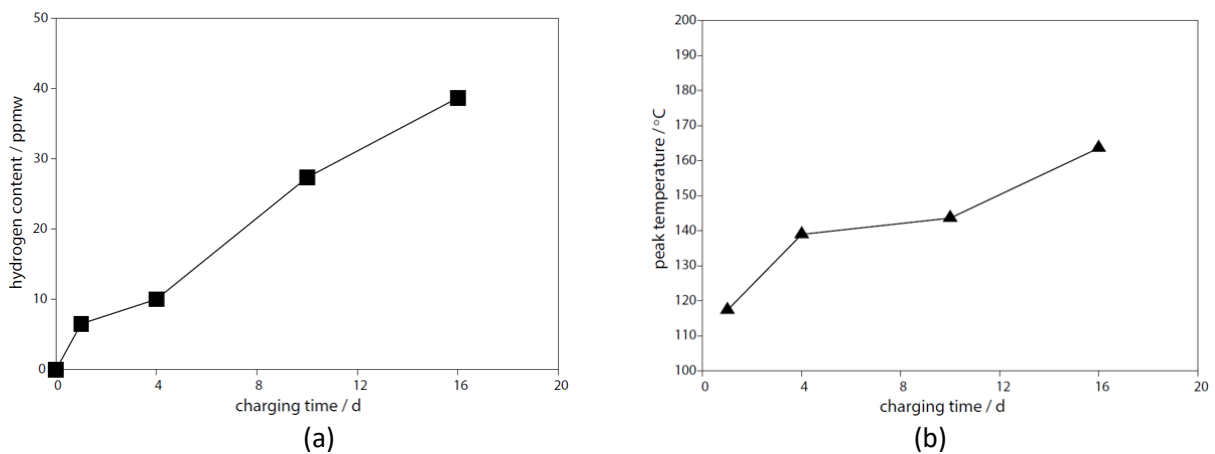


Figure 3.25: Variation in (a) total hydrogen content (b) peak temperature of constant-heating-rate TDA of duplex steel specimens charged for different times

Diffusion simulation using MATLAB was attempted, trying to simulate the diffusion profile within the material with respect to charging time. A correlation between the diffusion profile and the total hydrogen content might then be established to better understand the charging process. In the diffusion simulation for duplex steel, it is assumed that the primary austenite grains are the main contributors to hydrogen absorption since the solubility of hydrogen in austenite is 2-3 orders of magnitude higher than that in ferrite. In this model, it is assumed that grain boundary does not contribute significantly as a hydrogen segregation site. It is also assumed that all hydrogen in austenite is charged via the δ ferrite matrix where the diffusivity is much greater. Given the huge difference in the diffusivity of hydrogen in ferrite and in austenite, the diffusion time of hydrogen in ferrite matrix is insignificant compared with that in austenite. An illustration of this model is in figure 3.26:

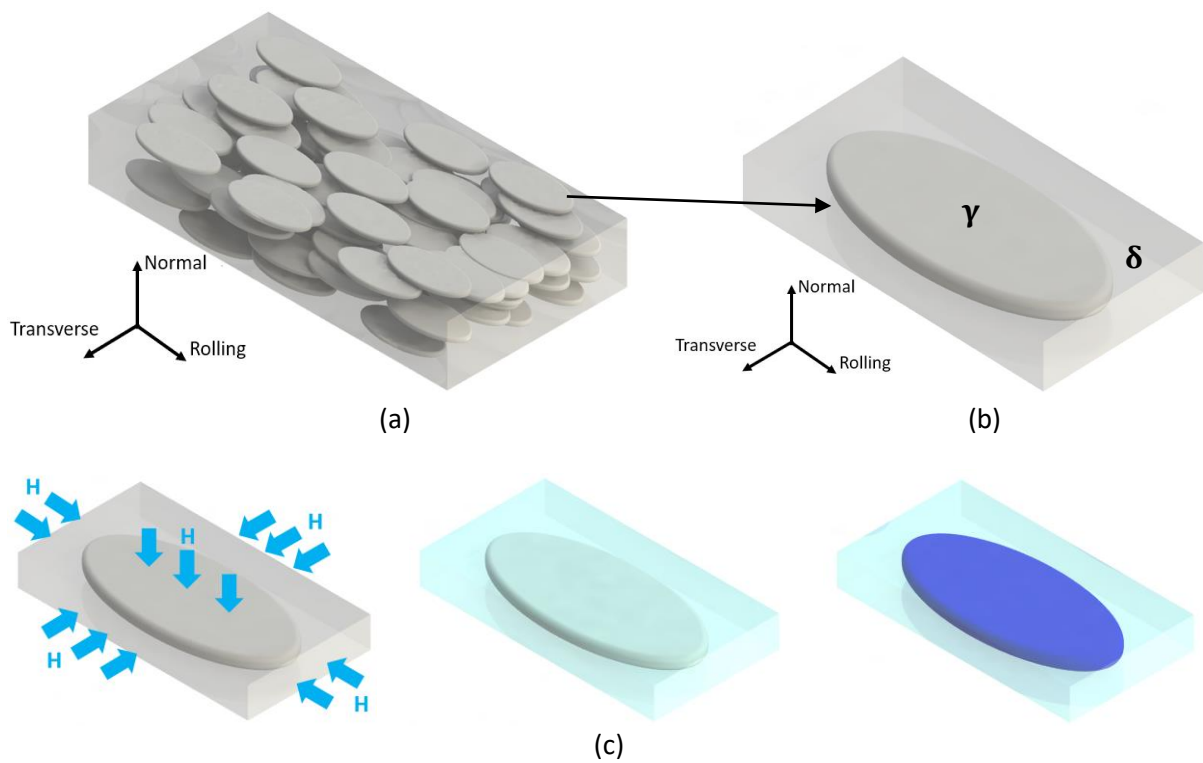


Figure 3.26: (a): a schematic of the duplex steel's microstructure, (b): schematic of one austenite grain within the ferrite matrix, (c): illustration of the hydrogen absorption process during hydrogen charging

After hot rolling, all austenite grains are compressed along the normal direction and elongated along the transverse and the normal directions. A typical austenite grain of such is shown in figure

3.26 (b). Assuming an elliptical sheet shape for all austenite grains, the actual average grain size along different directions can be estimated from the linear intercept values:

$$\begin{aligned}\bar{L}_{\text{Rolling,actual}} &\approx 80 \mu\text{m} \\ \bar{L}_{\text{Transverse,actual}} &\approx 40 \mu\text{m} \\ \bar{L}_{\text{Normal,actual}} &\approx \bar{L}_{\text{Normal}} \approx 8 \mu\text{m}\end{aligned}$$

The proof of this estimation is in appendix 6.26. The average linear intercept value along the normal direction is the smallest, of around $8 \mu\text{m}$. This value is representative of the actual grain size along this direction. The grain dimension along the transverse and the normal directions is much smaller than that along the rolling direction and the diffusion of hydrogen to the grain centre along these two directions also takes much shorter time. Therefore, in this diffusion model, only hydrogen diffusion along normal and transverse directions are taken into account. This is illustrated in figure 3.27:

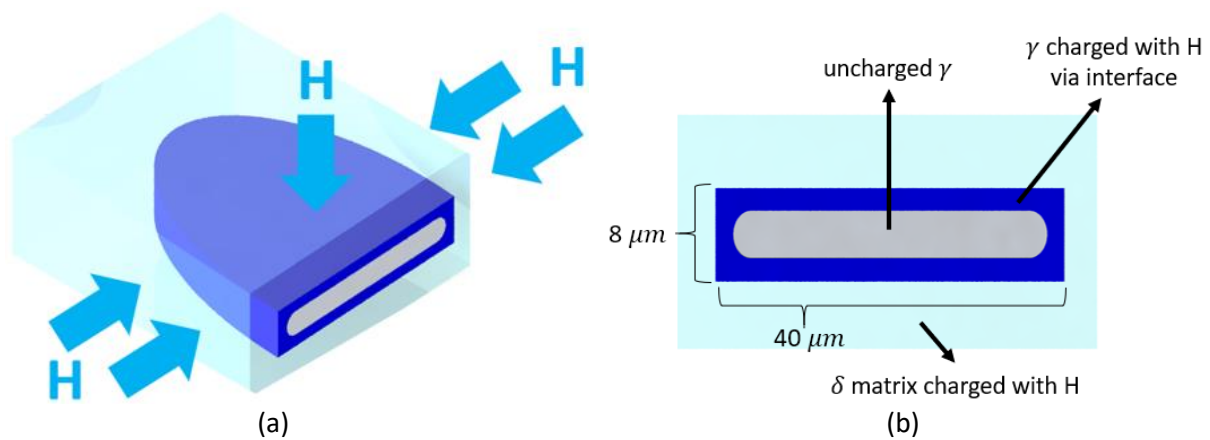


Figure 3.27: (a): Illustration of hydrogen infusion into an austenite grain during hydrogen charging, (b) is a 2D image of (a) from the front viewing plane

Figure 3.27 (b) shows the infusion of hydrogen into an austenite grain from the transverse and the normal directions. This study used a simple and standard MATLAB diffusion model which is readily available online [67] with editable variables like boundary conditions, specimen dimensions, diffusion coefficient, diffusion time etc. This model only considers diffusion in one phase with a single value diffusion coefficient. The corresponding hydrogen diffusion simulation results are shown in figure 3.28:

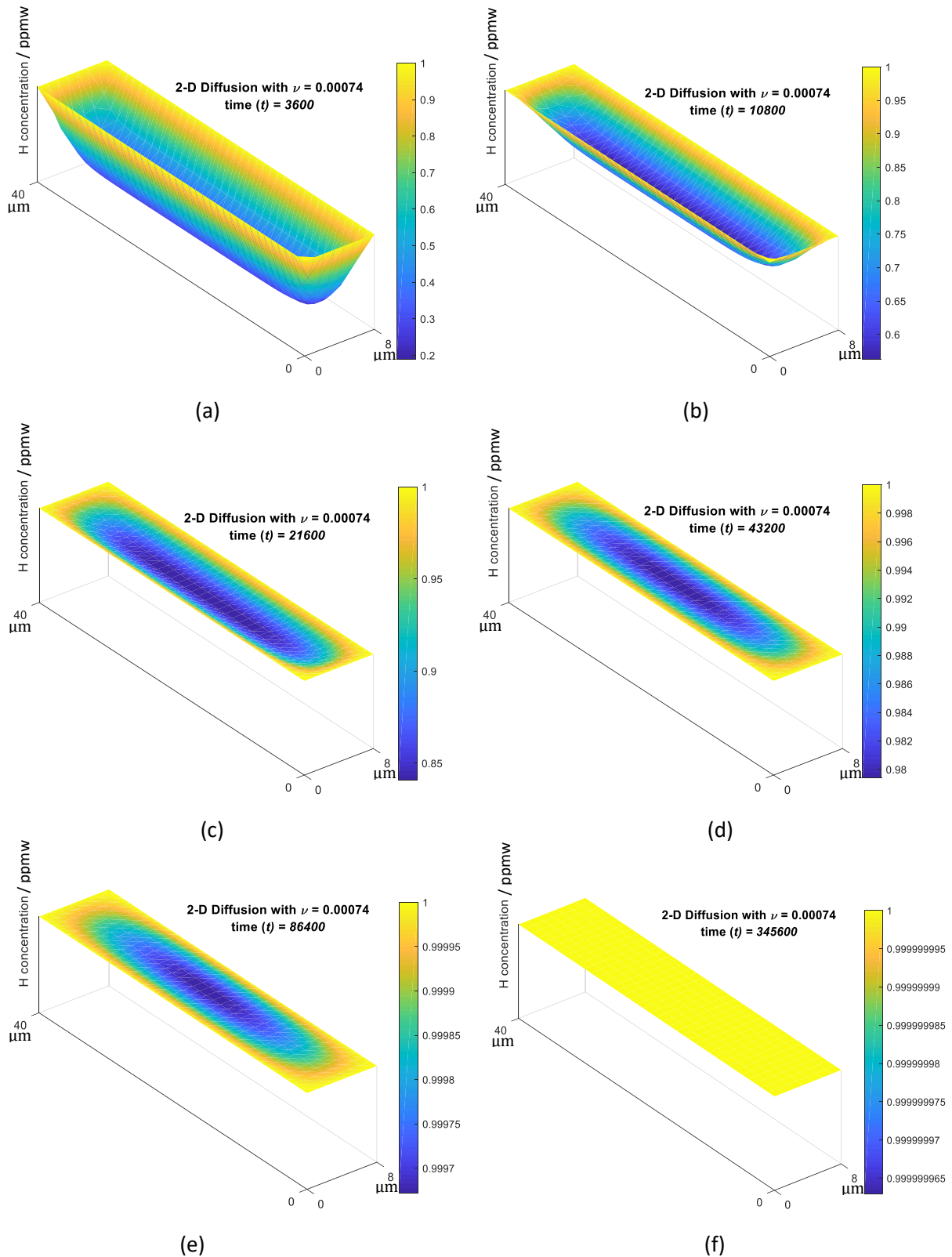


Figure 3.28: Simulated hydrogen concentration profile across an austenite grain after charging for (a) 1 h, (b) 3 h, (c) 6 h, (d) 12 h, (e) 24 h, (f) 4 d. ν is the diffusion coefficient with unit of ' $\mu\text{m}^2 \text{s}^{-1}$ ' and time (t) is with unit of 's'

In this diffusion simulation, a constant boundary condition was used, i.e. hydrogen concentration remains the same at the ferrite/austenite grain boundary with respect to time. Diffusivity values $D_\gamma = 7.4 \times 10^{-16} \text{ m}^2 \text{ s}^{-1}$ and $D_\alpha = 5.8 \times 10^{-8} \text{ m}^2 \text{ s}^{-1}$ from section 2 was employed. In this case, no matter what boundary concentration value is used (here a low concentration of 1 ppmw was used), the hydrogen concentration profile in austenite will stabilize and will not increase significantly only after 12 h of charging, as indicated in figure 3.28. This is rather counterintuitive since figure 3.24 and figure 3.25 (a) show that the total hydrogen content kept increasing significantly from 1 d to 16 d of charging. This model does not take traps into account. Therefore, a possible explanation is that the ferrite/austenite interfaces contribute greatly to the diffusion process of hydrogen as a trap site. It slows down the infusion of hydrogen from ferrite to austenite. Also, with longer charging time, more hydrogen could have accumulated at the ferrite/austenite interface. Therefore, the austenite grain's boundary hydrogen concentration, rather than staying at a constant value, could have increased with respect to charging time.

Further exploration of this diffusion process is beyond the scope of this project, but it is worth looking into in the future.

3.3.2 Austenitic steel

Figure 3.29 shows that, after charging, the relative intensity of the XRD peaks which correspond to the ferrite phase increased. This is most evident in the specimen which has been charged for 4 d, as indicated. This suggests that hydrogen charging might have induced martensitic transformation in this austenitic steel. This is also supported by the resultant phase fraction analysis in table 3.8, where all the charged specimens show increase in ferrite fraction. However, there is no direct correlation between the charging time and the amount of transformation. As shown here that, the ferrite/martensite phase fraction is lower for the 10-day and 16-day charging conditions than for the 4-day condition. This implies that ferrite/martensite transformed back to austenite after longer charging time, which is impossible. Such inconsistency is most likely due to the variation in individual specimens' starting phase fraction.

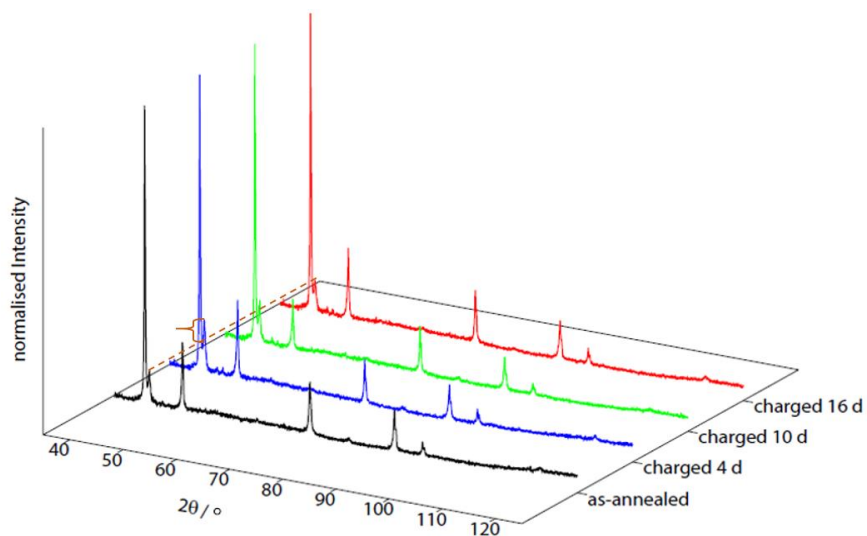


Figure 3.29: Normalized XRD plots for austenitic steel specimens charged for different times then aged at room temperature for 5.5 h

Condition	Ferrite/martensite fraction	Austenite fraction	Ferrite March/Dollase direction	Austenite March/Dollase direction
as-annealed	0.07 ± 0.01	0.93 ± 0.02		
charged 4 d	0.14 ± 0.01	0.86 ± 0.02		
charged 10 d	0.12 ± 0.01	0.88 ± 0.02	N/A	unfavoured: 010
charged 16 d	0.11 ± 0.01	0.89 ± 0.02		

Table 3.8: Phase fraction analysis for austenitic steel specimens charged for different times, the corresponding fittings are in appendix 6.18

The shape of the room-temperature hydrogen desorption profiles, as shown in figure 3.30, resemble those of the duplex steel specimens. No strong variation was found among the room-temperature hydrogen desorption spectra of specimens charged for different times.

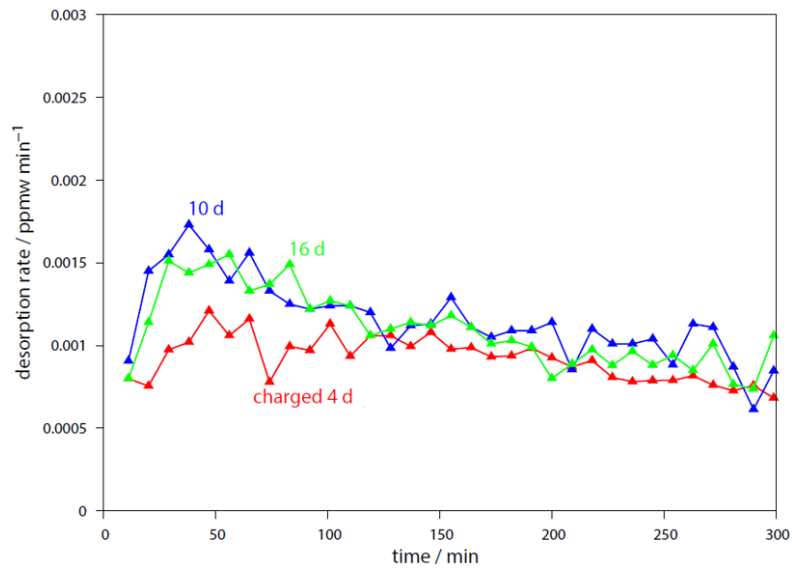


Figure 3.30: Compiled room-temperature hydrogen desorption spectra of austenitic steel specimens charged for different times

As shown in figure 3.31, each constant-heating-rate TDA spectrum of a charged austenitic steel specimen contains 2 peaks: a low-temperature peak at 100 °C to 150 °C with higher intensity and another high-temperature peak at 300 °C to 400 °C.

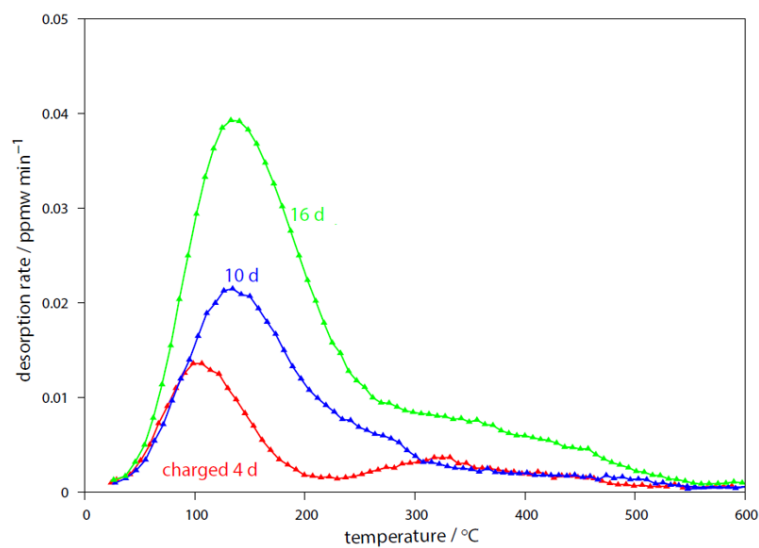


Figure 3.31: Constant-heating-rate TDA of austenitic steel specimens charged for different times then aged at room temperature for 5.5 h

Similar to the duplex steel's case, longer charging time introduces more hydrogen into the austenitic steel and shifts the peak toward higher temperature, as demonstrated in figure 3.32:

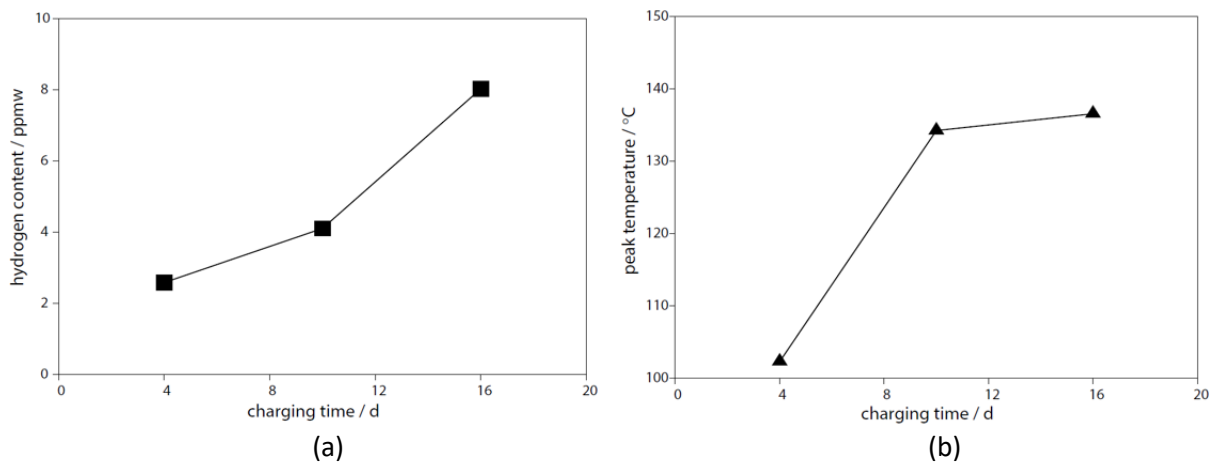


Figure 3.32: Variation in (a) total hydrogen content, (b) peak temperature of constant-heating-rate TDA, of austenitic steel specimens charged for different times then aged at room temperature for 5.5 h

1D diffusion simulation was employed. For the austenitic steel specimens, it is assumed that the hydrogen infusion is mainly dependent on the bulk diffusion in austenite, i.e. grain boundaries and delta ferrite have an insignificant effect. Such a model is illustrated in figure 3.33:

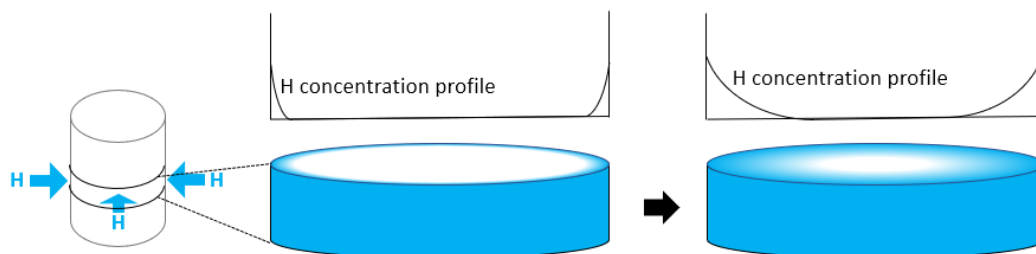


Figure 3.33: Hydrogen infusion into a 4 mm diameter austenite steel specimen during hydrogen charging and the corresponding hydrogen concentration profiles (this is only an illustration of how H profile changes during hydrogen charging, the actual diffusion length in austenite is only hundreds of microns after weeks of charging)

After fitting different values, the best boundary hydrogen concentration was found to be 230 ppmw so the simulated total hydrogen content values, calculated from the simulated hydrogen concentration profile, best match the experimental total hydrogen content values, obtained from TDA measurements. These total hydrogen content values obtained from simulated and experimental results are compared in figure 3.35.

Simulated hydrogen profiles based on the boundary hydrogen concentration of 230 ppmw are

shown in figure 3.34:

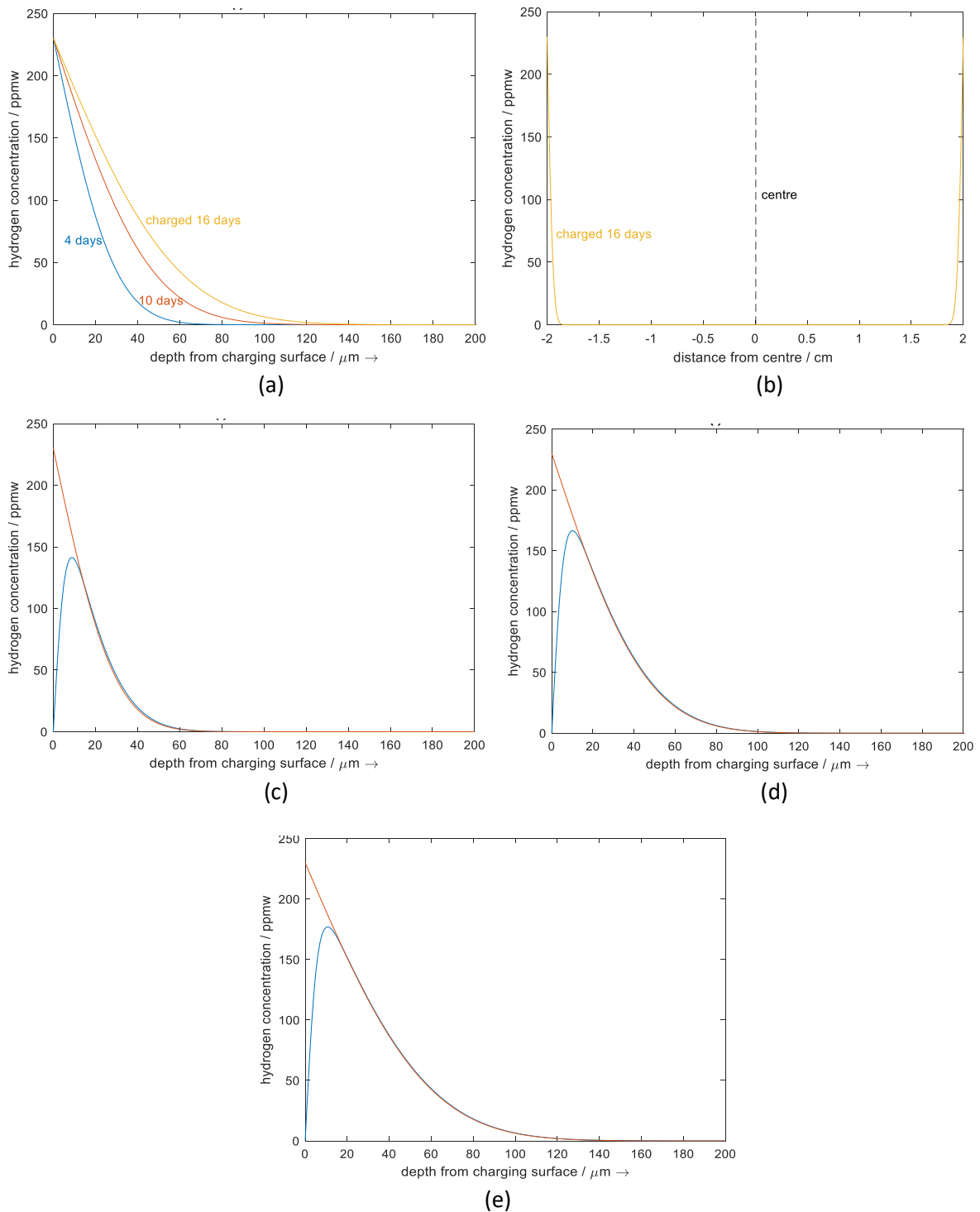


Figure 3.34: Simulated hydrogen concentration profile in the austenitic steel. (a): charged for 4 d, 10 d and 16 d, (b): concentration profile across the whole 4 mm diameter specimen after 16 d of charging, (c): charged for 4 d (red) then aged for 5.5 h (blue), (d): charged for 10 d (red) then aged for 5.5 h (blue), (e): charged for 16 d (red) then aged for 5.5 h (blue)

All these total hydrogen content values of the charged austenitic steel, either by the TDA measurements, or by the diffusion simulation, were obtained from specimens aged for 5.5 h after being charged. (5.5 h is the total time for installation, purging and room-temperature hydrogen desorption detection) The simulated profiles in figure 3.34 perfectly match the calculated hydrogen profiles using equation 4 by applying the same boundary hydrogen concentration. The penetration depth of hydrogen increases after longer charging times as shown in (a). The corresponding total hydrogen content also increases. For each charging time, after 5.5 h of degassing, the hydrogen profile close to the surface drops significantly since now the surface has shifted from a hydrogen-rich boundary condition to a hydrogen-free condition. However, the hydrogen profile away from the surface does not seem to change much after degassing. This can be seen in figure 3.34 (c)-(e).

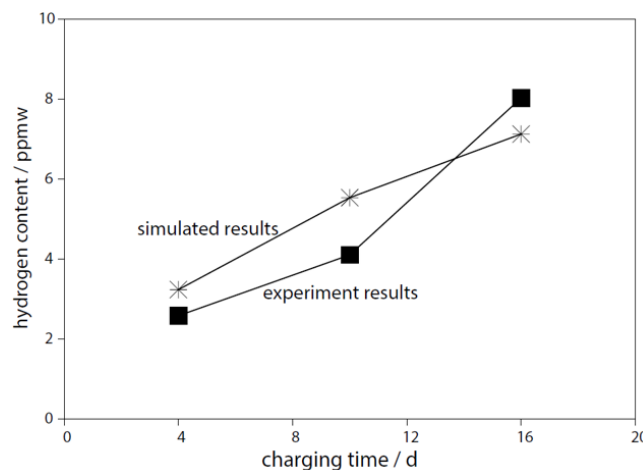


Figure 3.35: Comparison between the simulated and experimental total hydrogen content values of austenite steel specimens charged for different times then aged at room-temperature for 5.5 h

The corresponding total hydrogen content of a specimen after charging and degassing can be calculated using the simulated hydrogen profile in figure 3.34. Figure 3.35 shows a relatively good agreement between the simulated and the experimental results (from TDA). The differences between the two arise from the fact that the diffusion simulation only considers bulk diffusion in austenite phase, while the actual diffusion process during charging and TDA detection is much more complicated. For example, any compound formed during charging on the specimen surface can alter the boundary condition, and the δ ferrite phase and its interphase with the austenite matrix can also potentially change how hydrogen diffuses within the material.

3.3.3 Bainitic steel

There is no significant change in XRD and corresponding phase fraction analysis after prolonged charging. This is shown in figure 3.36 and table 3.9.

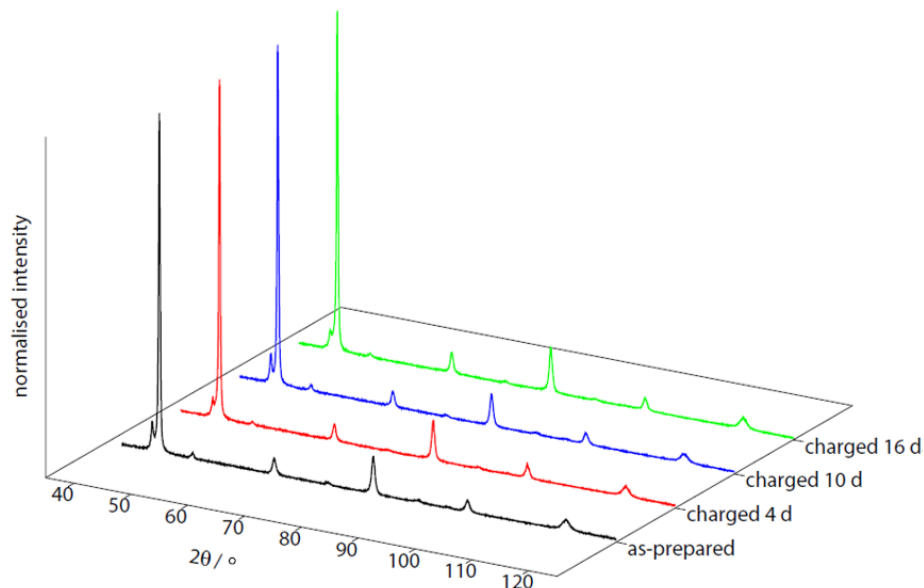


Figure 3.36: Normalized XRD plots for bainitic steel specimens charged for different times

Condition	Ferrite/martensite fraction	Austenite fraction	Ferrite March/Dollase direction	Austenite March/Dollase direction
as-prepared	0.90 ± 0.02	0.10 ± 0.04		
charged 4 d	0.92 ± 0.01	0.08 ± 0.03	N/A	N/A
charged 10 d	0.93 ± 0.01	0.07 ± 0.03		
charged 16 d	0.94 ± 0.01	0.06 ± 0.02		

Table 3.9: Phase fraction analysis for bainitic steel specimens charged for different times, the corresponding fittings are in appendix 6.19

The shape of the room-temperature hydrogen desorption profiles, as shown in figure 3.37, resemble that of the other two types of steel, though the desorption rates are much lower. No strong variation was found among the room-temperature hydrogen desorption spectra of specimens charged for different times, except for the specimen only charged for 1 d, whose desorption rate is lower than the others. This is because it has relatively low total hydrogen content, as shown later in figure 3.39.

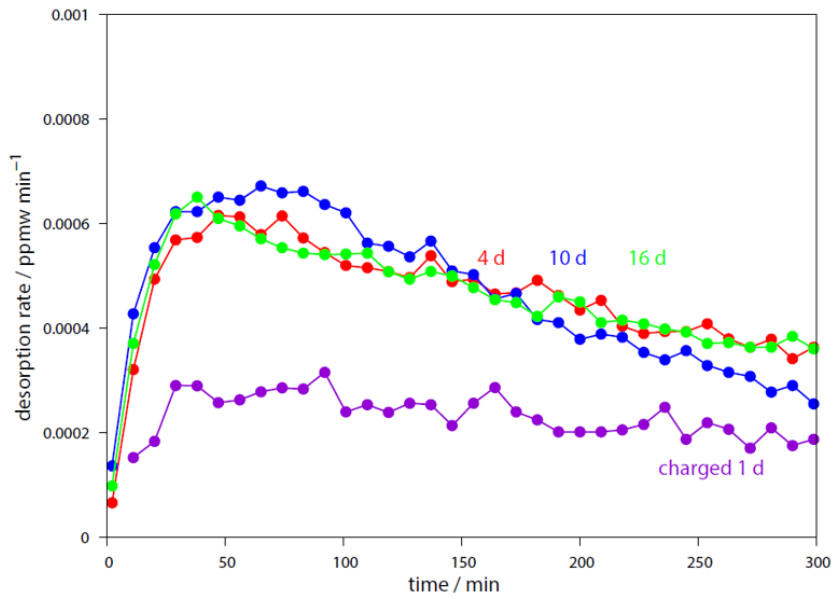


Figure 3.37: Compiled room-temperature hydrogen desorption spectra of bainitic steel specimens charged for different times

Figure 3.38 shows an increase in hydrogen desorption rate in the as-prepared bainitic steel from 320 °C to 600 °C. This is unexpected since 48 h homogenization at 1200 °C must have released all the hydrogen. This background peak was also observed in all the charged and compressed bainitic specimens. Previous work also reported this background peak being observed in other types of steel and its nature was discussed in detail by Fielding [47].

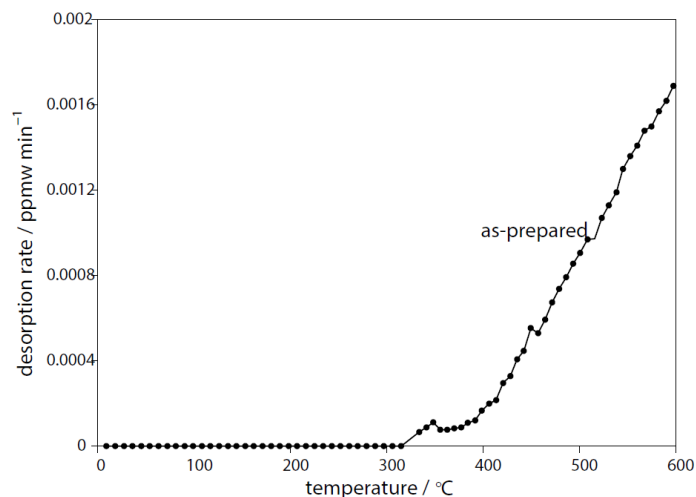


Figure 3.38: Typical constant-heating-rate TDA of the as-prepared bainitic steel with no hydrogen charging

This background peak does not depend on hydrogen charging conditions. However, it depends on specimen's surface area rather than its weight. Therefore, it most likely results from the surface reaction between the TDA carrier gas and the specimen surface. It has been speculated that either water or methane gas from the carrier gas could potentially react with the specimen and released hydrogen. This background peak has very high magnitude compared with other peaks in this bainitic steel, yet it is not always very consistent. Therefore, for this material, only peaks detected below 300 °C will be studied, since any possibly existing peak at higher temperature cannot be distinguished from this background peak.

Figure 3.39 shows that, each constant-heating-rate TDA spectrum contains a single peak at around 100 °C to 120 °C. A comparison of total hydrogen content and peak temperature among bainitic steel specimens with different charging times is shown in figure 3.40.

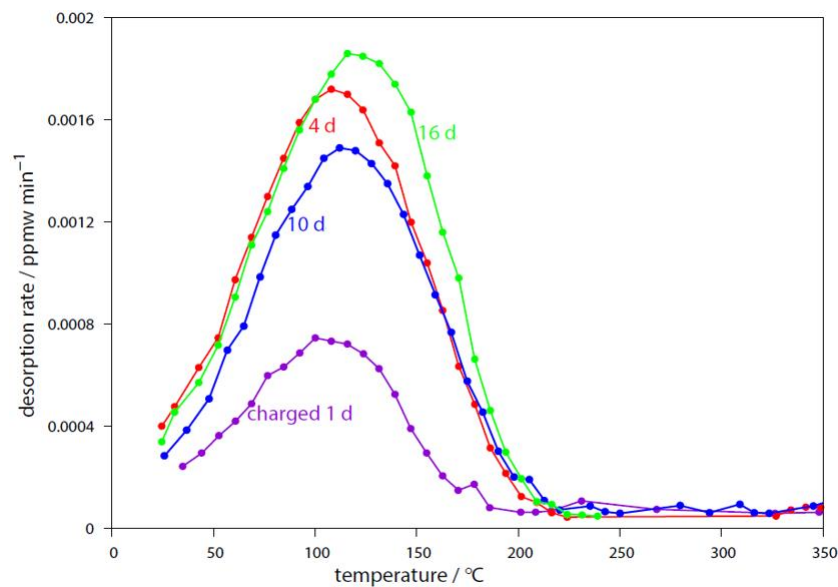


Figure 3.39: Constant-heating-rate TDA of bainitic steel specimens charged for different times then aged at room temperature for 5.5 h

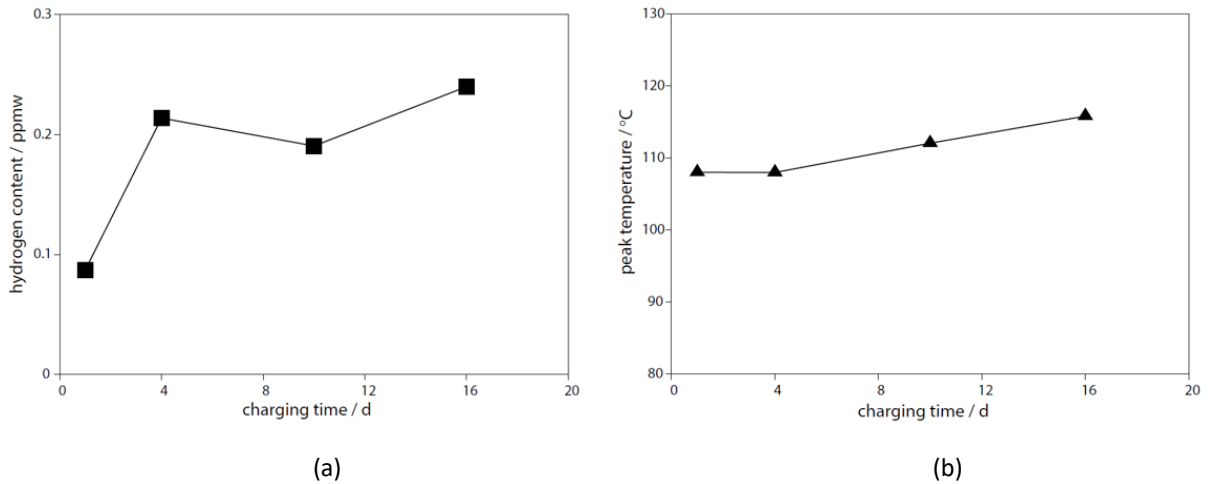


Figure 3.40: Variation in (a) total hydrogen content, (b) peak temperature, of constant-heating-rate TDA of bainitic steel specimens charged for different times

The total hydrogen content in the charged bainitic steel specimens is much lower compared with the other two types of steel, less than 0.5 ppmw. The total hydrogen content is lower for the specimen charged for only 1 day. The other specimens which have been charged for longer time have similar amount of total hydrogen contents. Also, little difference of the peak temperature among these specimens was found. This could be because the specimens become saturated with hydrogen after 4 days of charging under this charging condition. Since bainitic ferrite has much lower solubility yet much larger diffusivity, it will soon be saturated with low concentration of hydrogen.

3.4 Changes in room-temperature hydrogen desorption and XRD after compression

3.4.1 Duplex steel

There are some minor differences among the XRD spectra in figure 3.41. Their corresponding phase analysis in table 3.10, on the other hand, shows no significant variation. This indicates that charging time does not affect the phase fraction of the duplex steel after compression. The differences among XRD are due to the variation in texture developed in individual specimens during compression.

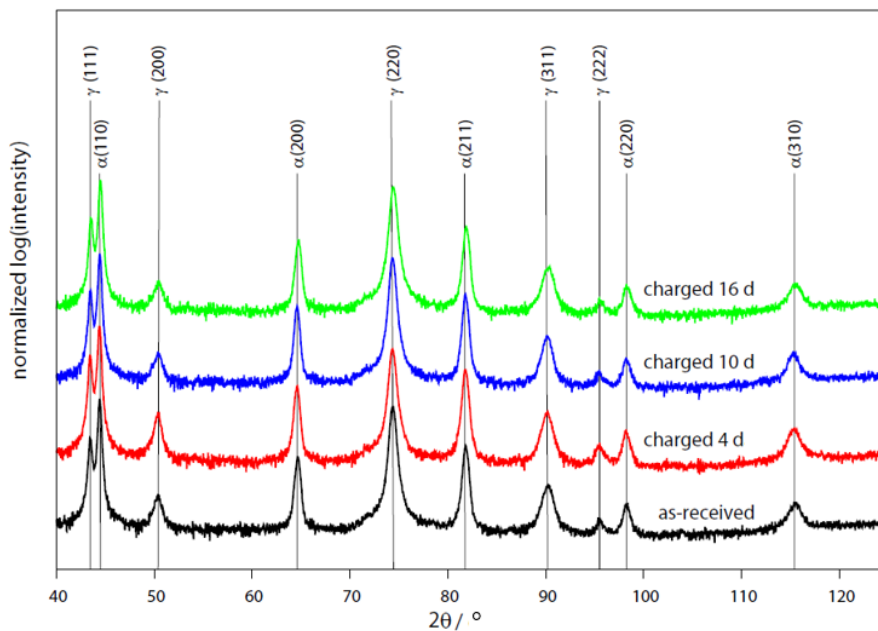


Figure 3.41: Normalized logarithm XRD plots for duplex steel specimens charged for different times then compressed

Condition	Ferrite fraction	Austenite fraction	Ferrite March/Dollase direction	Austenite March/Dollase direction
as-received compressed	0.42 ± 0.04	0.58 ± 0.05		
charged 4 d compressed	0.39 ± 0.03	0.61 ± 0.01	favoured: 121, 010	favoured: 011, unfavoured: 010
charged 10 d compressed	0.40 ± 0.04	0.60 ± 0.03		
charged 16 d compressed	0.42 ± 0.04	0.58 ± 0.05		

Table 3.10: Phase fraction analysis for duplex steel specimens charged for different times then compressed, the corresponding fittings are in appendix 6.20

As shown in figure 3.42, for charged duplex steel specimens, each ‘after-compression’ hydrogen desorption profile, to a great extent, follows the extrapolated profile of the corresponding ‘before-compression’ profile. This is because there is no deformation-induced transformation in this material, as shown in section 3.2.1. Therefore, the hydrogen desorption behaviour has no significant change after compression. However, some ‘after-compression’ hydrogen desorption profiles are a bit lower than extrapolated profiles, as shown in (b) and (c). This is due to the strain-induced defects, which act as hydrogen traps, slowing down the diffusion of hydrogen.

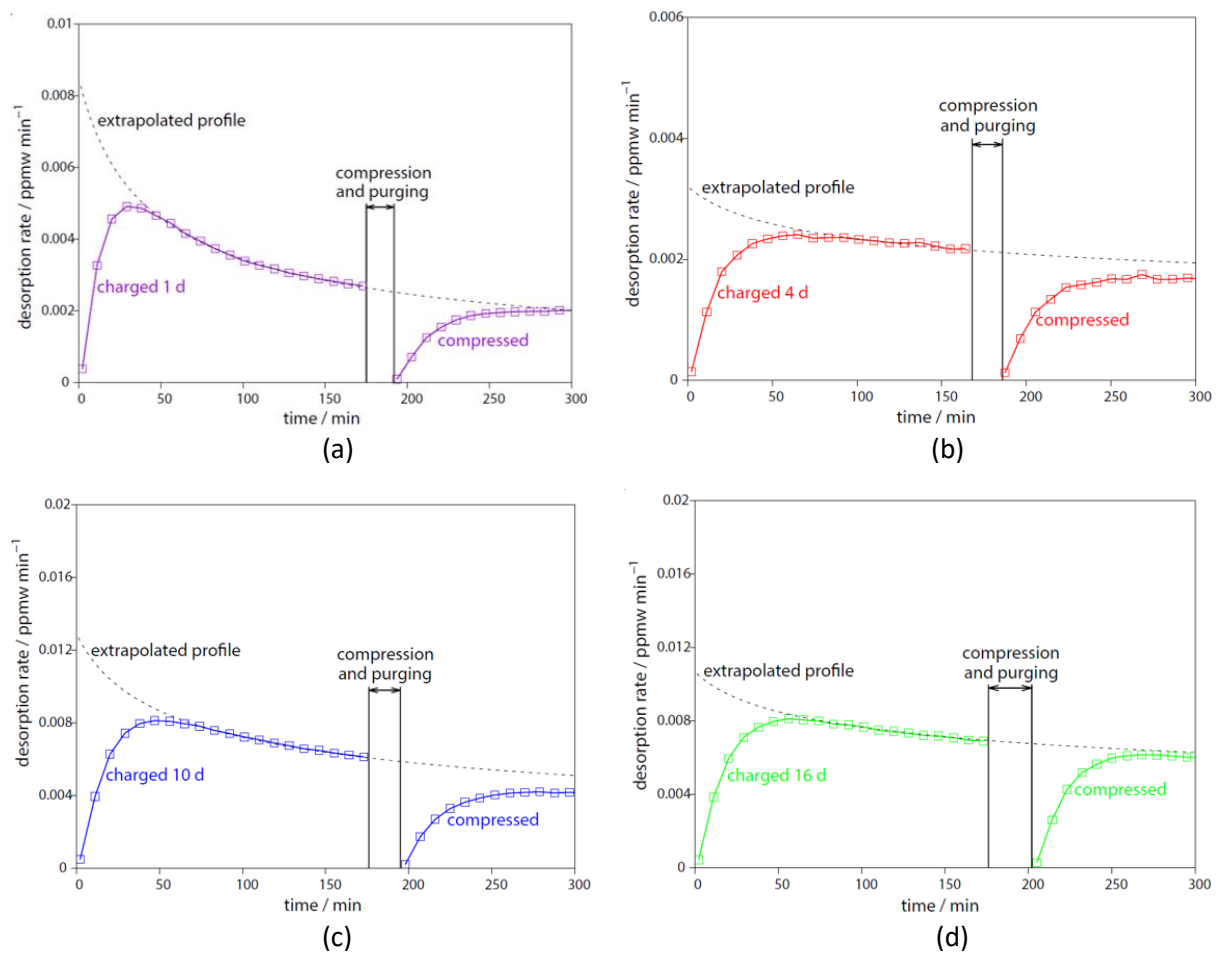


Figure 3.42: Room-temperature hydrogen desorption spectra before and after compression of the Duplex steel specimens charged for different times (a) 1 d (b) 4 d (c) 10 d (d) 16 d

3.4.2 Austenitic steel

As shown in figure 3.43 and table 3.11, the situation for the austenitic steel is the same as for the duplex steel: minor differences exist among XRD spectra due to variation in texture. Charging time does not affect the phase fraction of the austenitic steel after compression, i.e. in this case, hydrogen charging has no significant effect on the amount of martensite formed due to compression.

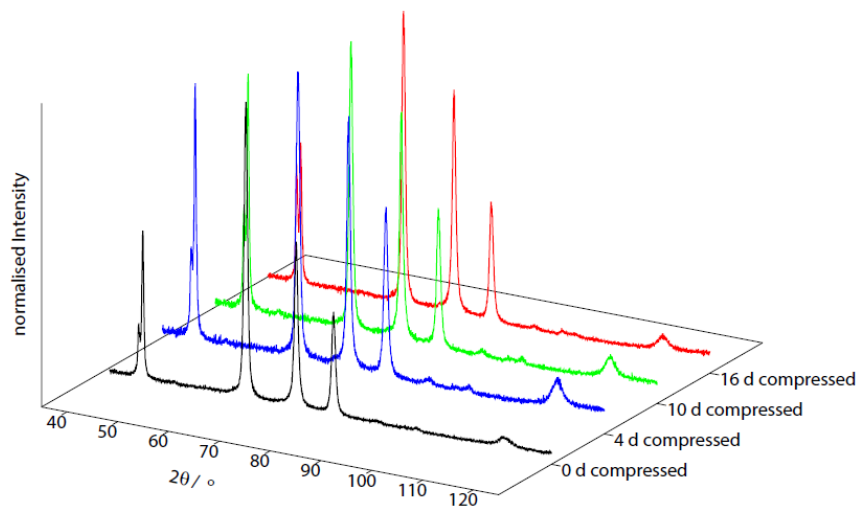
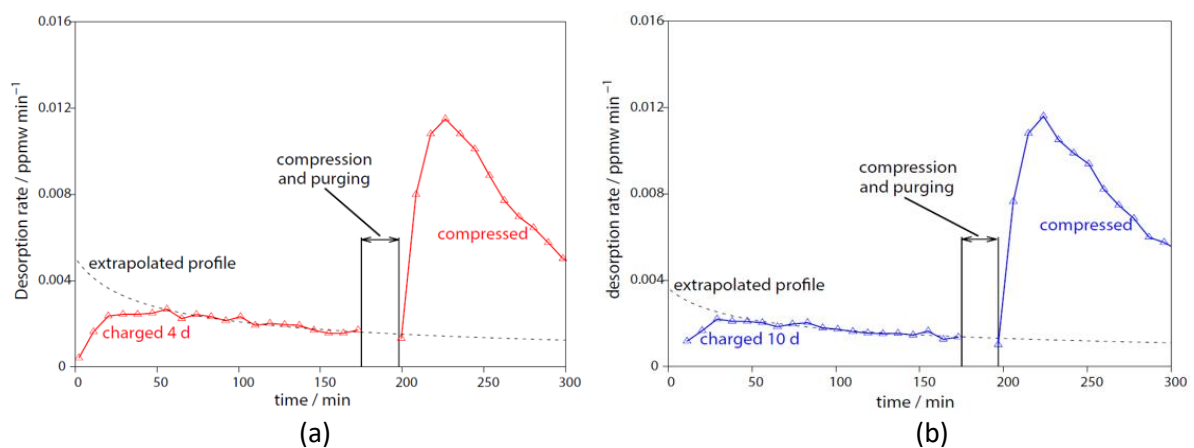


Figure 3.43: Normalized XRD plots for austenitic steel specimens charged for different times then compressed

Condition	Ferrite fraction	Austenite fraction	Ferrite March/Dollase direction	Austenite March/Dollase direction
as-annealed compressed	0.82 ± 0.01	0.18 ± 0.03		
charged 4 d compressed	0.85 ± 0.01	0.15 ± 0.03	favoured: 121, 010	favoured: 011, unfavoured: 010
charged 10 d compressed	0.83 ± 0.01	0.17 ± 0.04		
charged 16 d compressed	0.82 ± 0.01	0.18 ± 0.04		

Table 3.11: Phase fraction analysis for austenitic steel specimens charged for different times then compressed, the corresponding fittings are in appendix 6.21



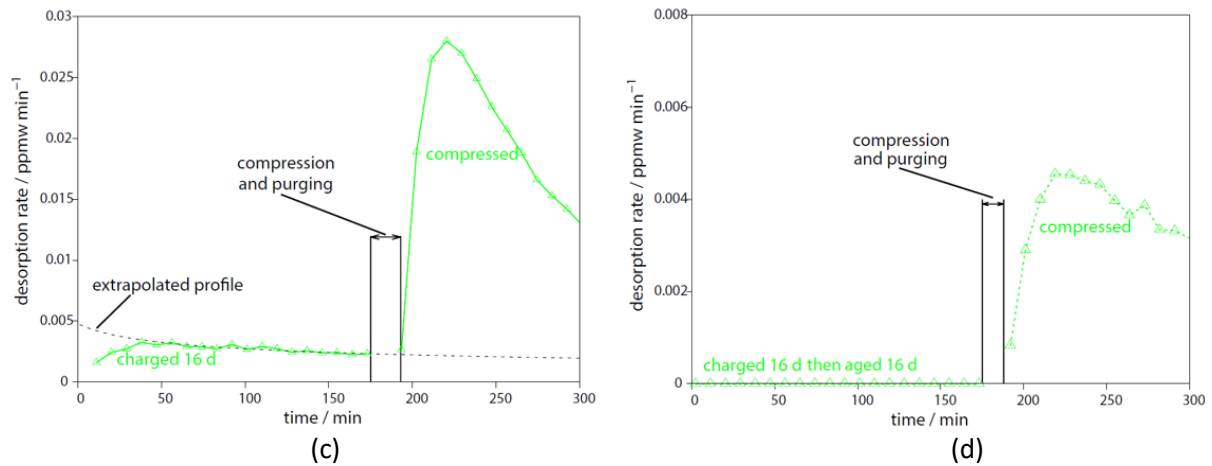


Figure 3.44: Room-temperature hydrogen desorption spectra before and after compression of austenitic steel specimens charged for different times, (a) 4 d, (b) 10 d, (c) 16 d, (d) 16 d then aged for another 16 d before compression

All 'after-compression' hydrogen desorption profiles are much higher than the extrapolated profiles of their corresponding 'before-compression' hydrogen desorption profiles. Such a burst in hydrogen desorption rate is due to the formation of deformation-induced martensite. After compression, most of the austenite transformed into martensite. These newly formed martensite will be oversaturated with hydrogen since martensite has much lower hydrogen solubility. The hydrogen inherited from austenite will become highly mobile within the lattice and desorb rapidly from the specimen.

Figure 3.44 (c) shows that. This burst is more significant in the specimen which has been charged for 16 d since it has the highest total hydrogen content. Figure 3.44 (d) shows a specimen which has been charged for 16 d then aged for another 16 d. After aging, no room-temperature hydrogen desorption was detected. This suggests that most of the diffusible hydrogen near the sample surface has been desorbed from the specimen already. However, after compression, the desorption rate increases sharply. This increase in desorption rate is due to the release of the hydrogen atoms which were originally trapped in the austenite phase and the release of the hydrogen atoms far from the surface in the bulk austenite lattice which did not have the chance to diffuse out during aging. And the newly formed martensite provided an easy path for them to diffuse out.

3.4.3 Bainitic steel

As shown in figure 3.45 and table 3.12, the situation for bainitic steel is the same as for the other two types of steel: minor differences among XRD spectra yet phase analysis shows that the amount of deformation-induced martensite was not affected by charging.

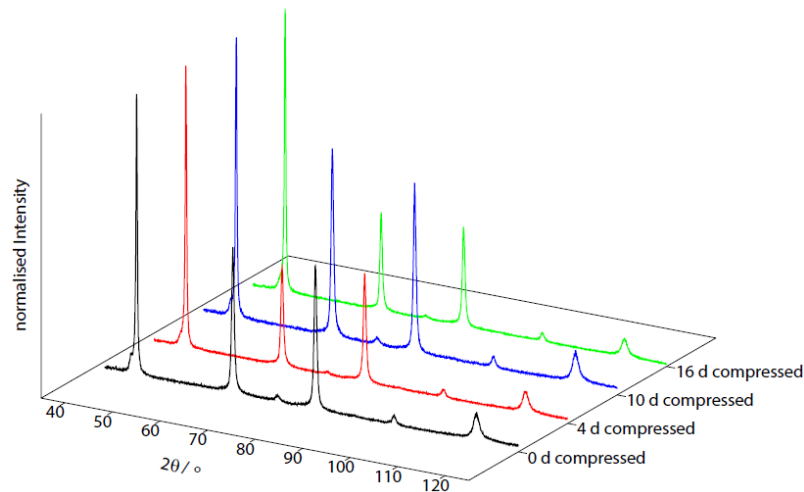


Figure 3.45: Normalized XRD plots for bainitic steel specimens charged for different times then compressed

Condition	Ferrite/martensite fraction	Austenite fraction	Ferrite March/Dollase direction	Austenite March/Dollase direction
as-prepared compressed	0.98 ± 0.01	0.02 ± 0.04		
charged 4 d compressed	0.97 ± 0.01	0.03 ± 0.04	favoured: 121, 011	favoured: 110
charged 10 d compressed	0.97 ± 0.01	0.03 ± 0.04		
charged 16 d compressed	0.97 ± 0.01	0.03 ± 0.04		

Table 3.12: Phase fraction analysis for bainitic steel specimens charged for different times then compressed, the corresponding fittings are in appendix 6.22

For every charged bainitic specimen, the room-temperature desorption stops after compression, as shown in figure 3.46. This is rather unexpected since this bainitic steel also experiences martensitic transformation. So, its room-temperature hydrogen desorption was expected to behave like that of the austenitic steel, i.e. increase after compression, rather than decrease.

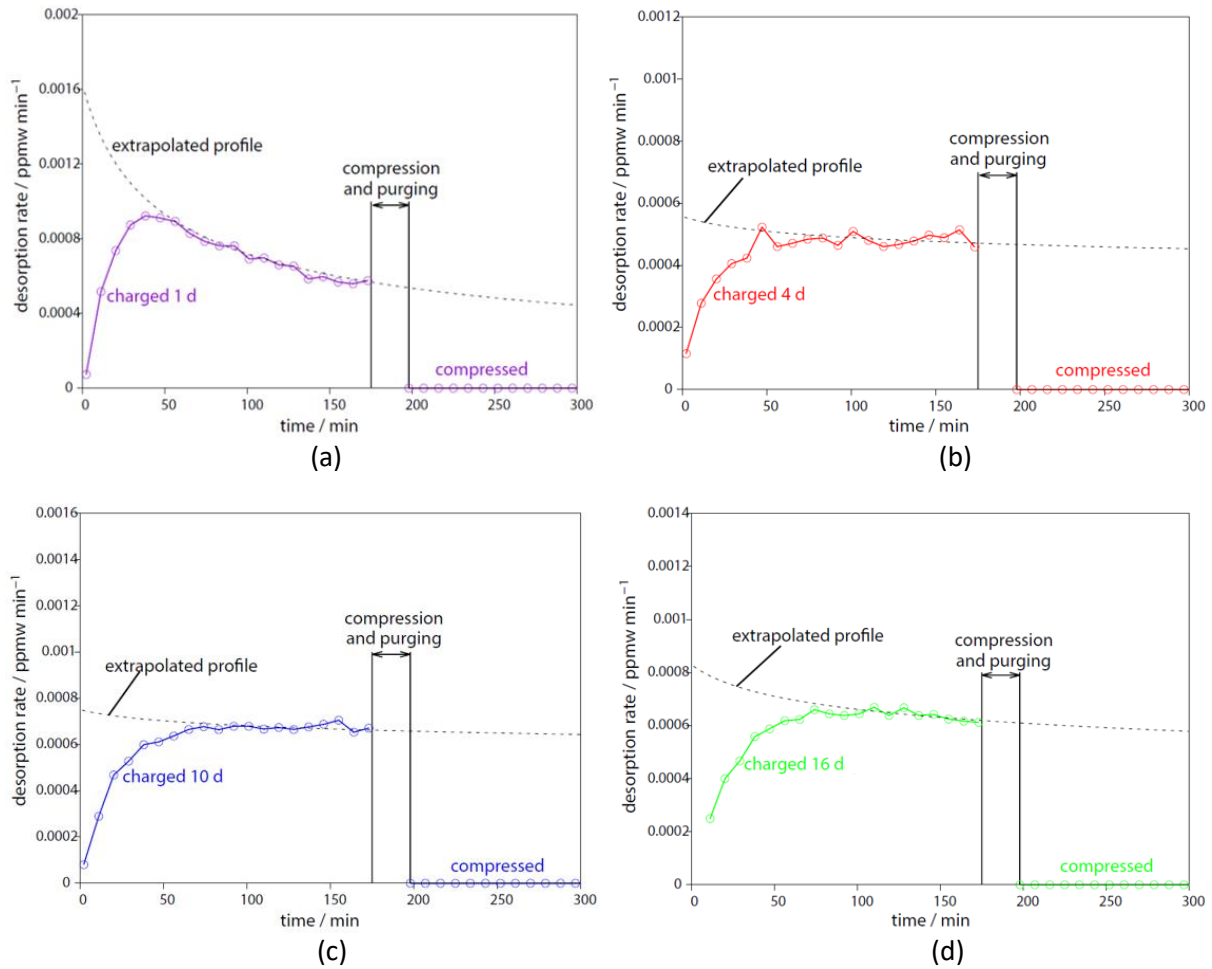


Figure 3.46: Room-temperature hydrogen desorption spectra before and after compression of bainitic steel specimens charged for different times, (a) 1 d, (b) 4 d, (c) 10 d, (d) 16 d

The explanation is that the austenite fraction in the bainitic steel is much lower than in the austenitic steel. After compression, the maximum martensitic transformation achieved was less than 0.08. The newly formed strain-induced defects, dislocations, vacancies etc., act as traps and greatly reduce the diffusion of all the diffusible hydrogen. This includes any possible additional diffusible hydrogen from martensitic transformation. The total hydrogen content in the bainite steel after charging was very low, less than 0.5 ppmw. The capability of these strain-induced traps is much higher than the total diffusible hydrogen. Therefore, almost all the diffusible hydrogen becomes trapped, so hydrogen desorption was no longer detected after compression. Using equations 16 and 17 from section 2, it was found that the dislocation density increased a lot after compression, from around 5×10^{14} to 4×10^{15} m⁻². (details in appendix 6.27)

3.5 Changes in constant-heating-rate TDA after compression

3.5.1 Duplex steel

Figure 3.47 shows that the compressed and uncompressed duplex steels exhibit similar spectra. Deformation has no significant effect on the constant-heat-rate TDA of duplex steel, in accordance with the room-temperature desorption results in section 3.4.1. The compiled TDA spectra for compressed specimens, as shown in figure 3.48, also show the similar trend as in figure 3.24 for uncompressed specimens.

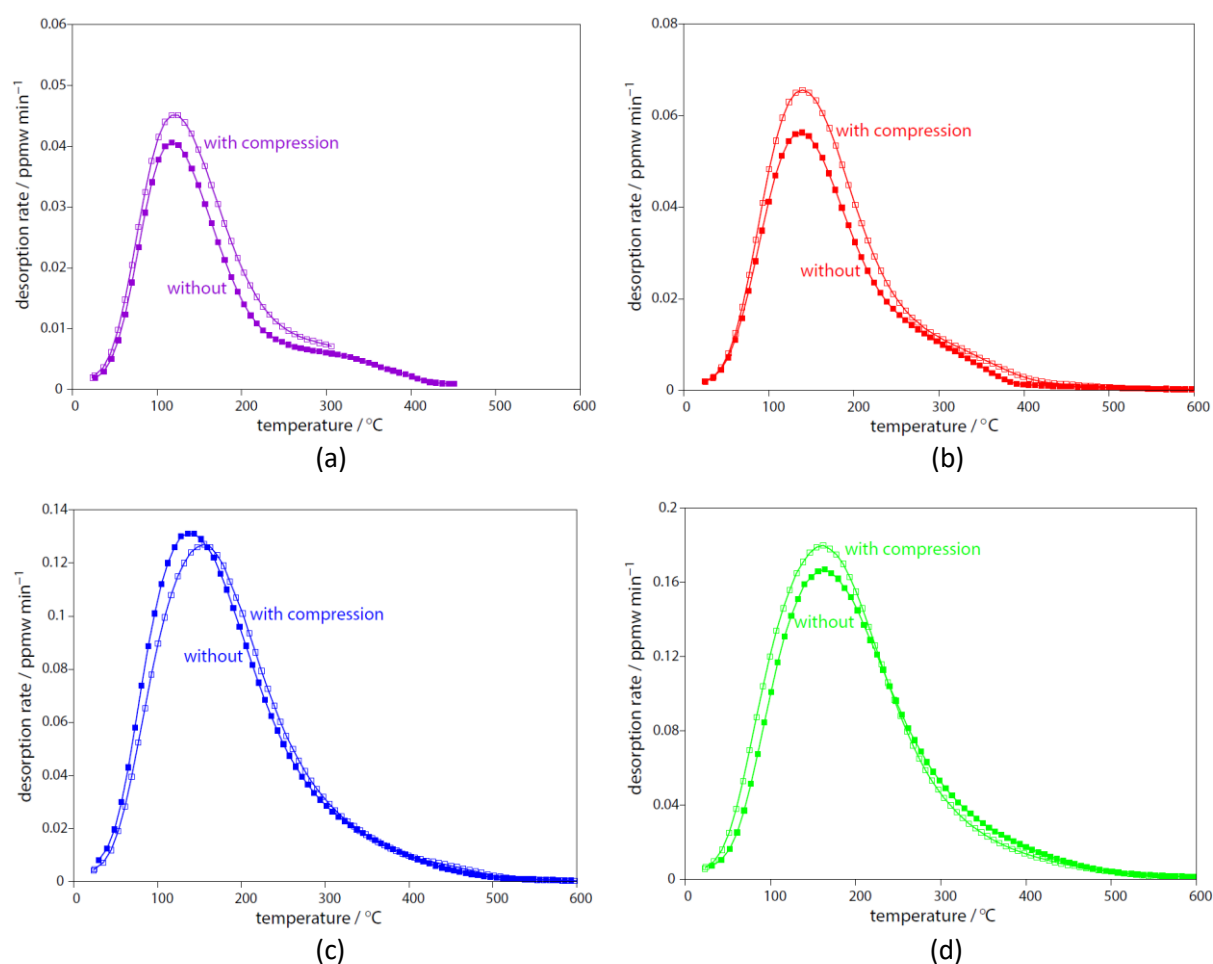


Figure 3.47: Comparison of constant-heating-rate TDA spectra between compressed (hollow square) and uncompressed (solid square) duplex steel specimens charged for different times, (a) 1 d, (b) 4 d, (c) 10 d, (d) 16 d, (e) as-received

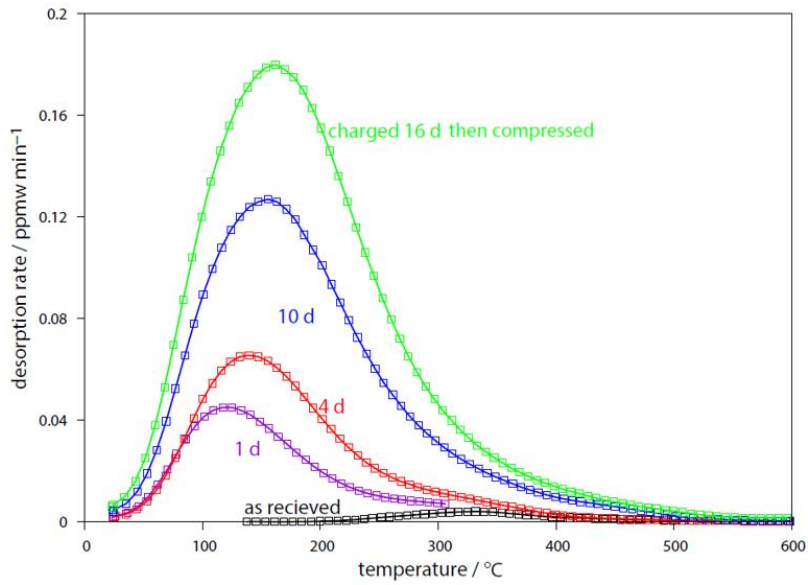


Figure 3.48: Compiled constant-heating-rate TDA spectra of compressed duplex steel specimens charged for different times

And just like for uncompressed specimens, longer charging time increases the total hydrogen content and shifts the peak towards higher temperatures, this is demonstrated in figure 3.49:

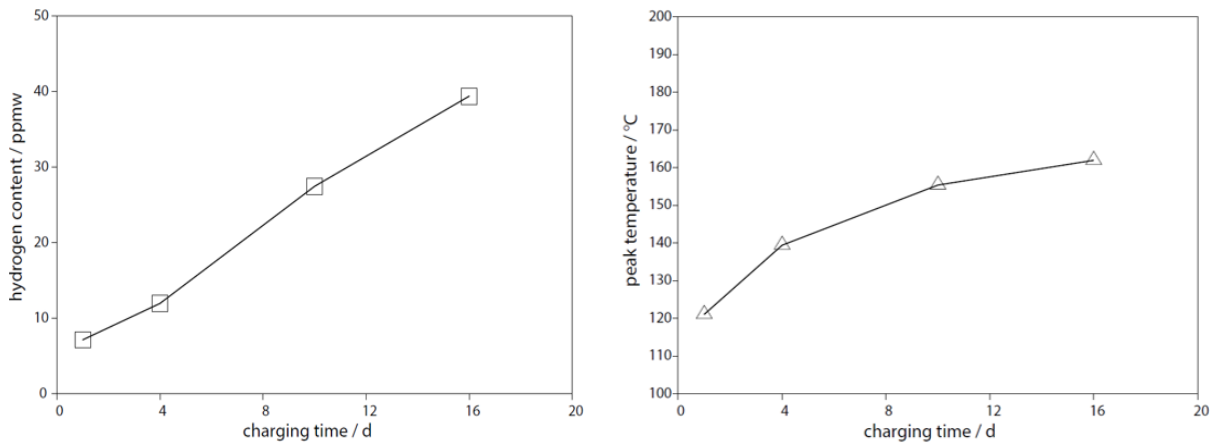


Figure 3.49: Variation in (a) total hydrogen content, (b) peak temperature of constant-heating-rate TDA, of compressed duplex steel specimens charged for different times

3.5.2 Austenitic steel

For every compressed austenitic specimen, both the low-temperature peak and the high-temperature peak were reduced in peak width and were shifted towards lower temperatures of around 80 °C and 250 °C respectively. This is shown in figure 3.50. Such peak shift indicates an overall increase in hydrogen diffusivity, which is consistent with the increase in the room-temperature desorption after compression. As discussed in section 3.4.2, such increase in hydrogen diffusivity is due to the phase transformation of austenite into ferrite which has a much higher hydrogen diffusivity.

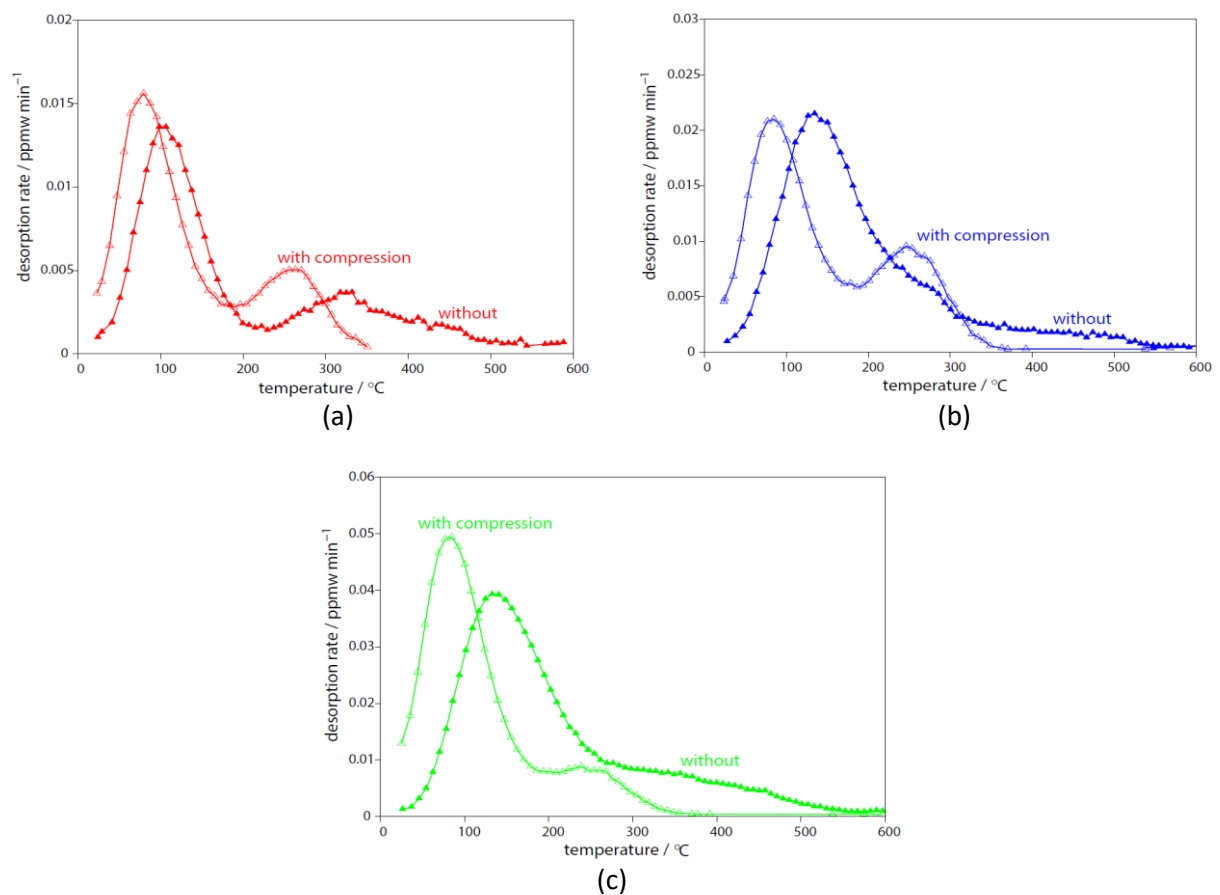


Figure 3.50: Comparison of constant-heating-rate TDA spectra between compressed (hollow triangle) and uncompressed (solid triangle) austenitic steel specimens charged for different times, (a) 4 d, (b) 10 d, (c) 16 d

Figure 3.51 shows the compiled TDA for specimens charged for different times then compressed. Both the low-temperature peak and the high-temperature peak do not shift but their magnitudes become higher for specimens charged for longer time. This is shown in figure 3.52.

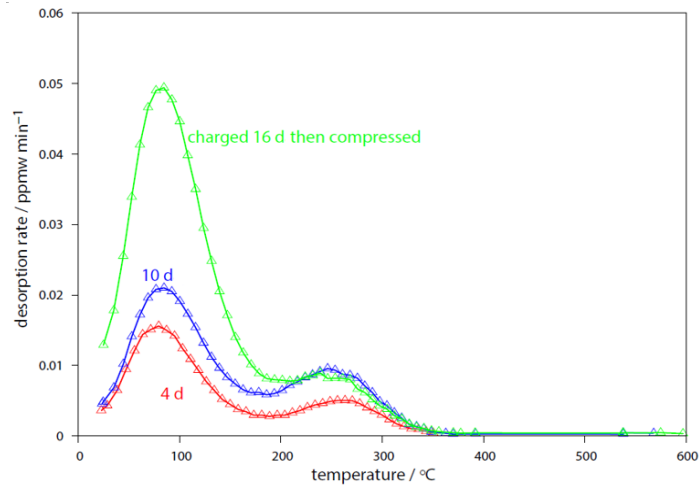


Figure 3.51: Compiled constant-heating-rate TDA spectra of compressed austenitic steel specimens charged for different times

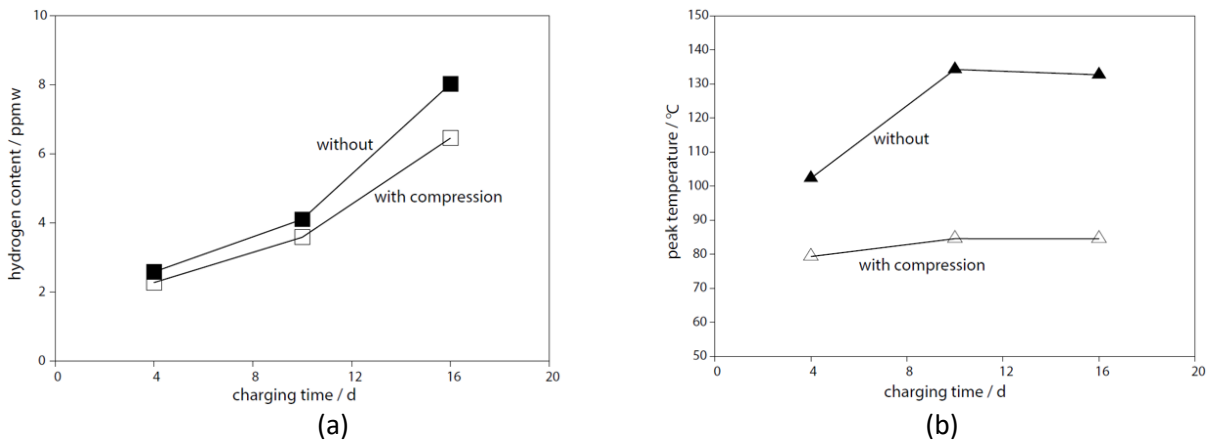


Figure 3.52: Comparison of (a) total hydrogen content, (b) peak temperature of constant-heating-rate TDA, between compressed (hollow shapes) and uncompressed (solid shapes) austenitic steel specimens charged for different times

Figure 3.52 (a) shows that the hydrogen content values of the compressed specimens are lower than those of the uncompressed specimens. This difference arises from the difference in room-temperature hydrogen desorption. When the burst in room-temperature desorption of the compressed specimens is taken into account, the total hydrogen content of the compressed and the uncompressed specimens become more or less the same. In this case, it was not possible to calculate the dislocation density change due to deformation using the Williamson-Hall technique as we did with the bainitic steel. This is because this technique requires the FWHM change measurement of at least 3 significant XRD peaks of one single phase before and after deformation, which is impossible in this case due to the significant phase transformation that took place during deformation.

3.5.3 Bainitic steel

Figure 3.53 shows that, after compression, each specimen's peak was moved to a higher temperature of around 170 °C. This new peak likely arises from strain-induced traps. Because the hydrogen content in the charged bainitic steel is rather low (less than 0.5 ppmw), these traps have enough capacity to trap all the diffusible hydrogen. Therefore, the low-temperature peak originally at 110 °C, which corresponds to the diffusible hydrogen, completely shifted to higher temperatures after compression. This is consistent with the room-temperature desorption results in section 3.4.3. The shift indicates that the binding energy of the newly generated traps is higher than the binding energy of the existing traps in the uncompressed specimens.

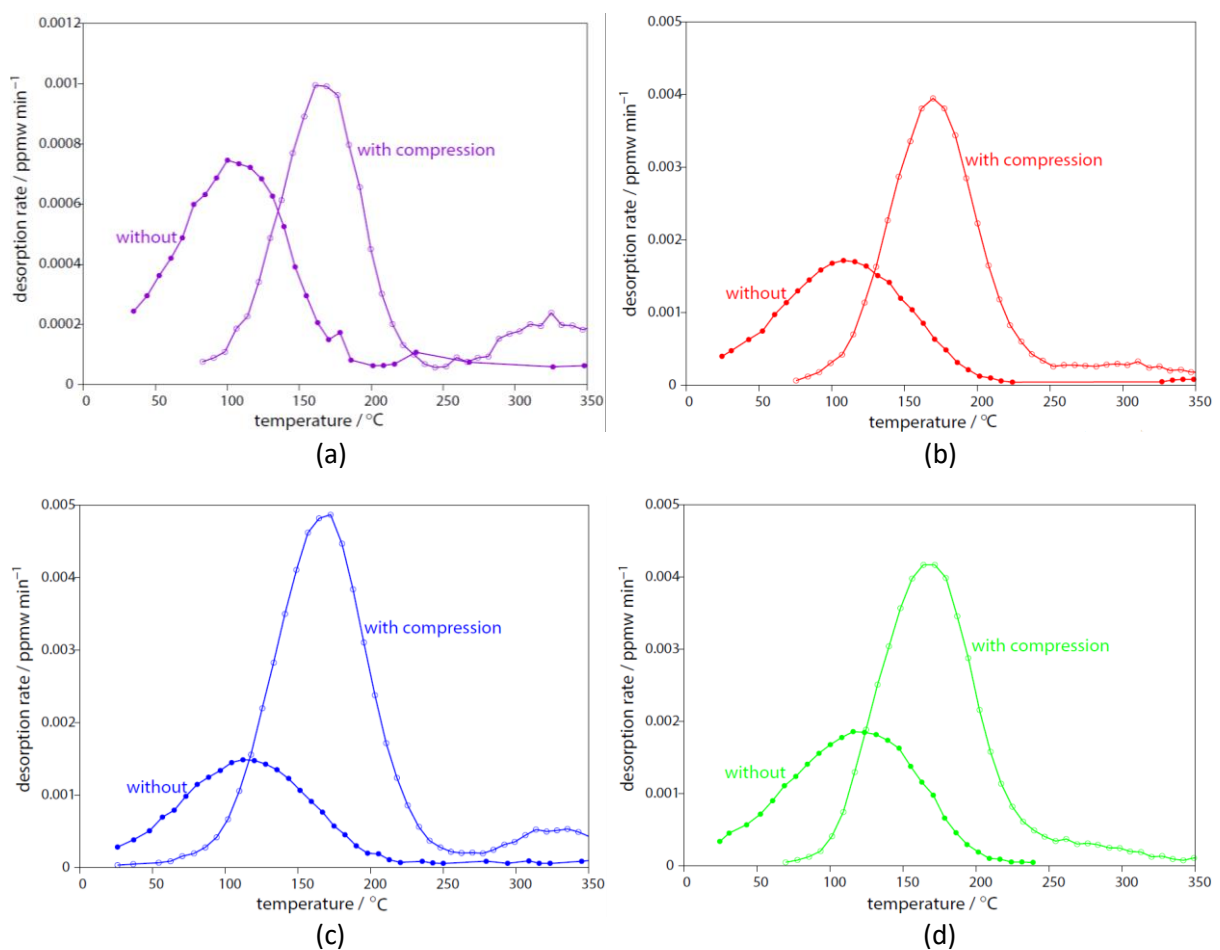


Figure 3.53: comparison of constant-heating-rate TDA spectra between compressed (hollow circle) and uncompressed (solid circle) bainitic steel specimens charged for different times, (a) 1 d, (b) 4 d, (c) 10 d, (d) 16 d

Figure 3.54 compiles the TDA spectra of the bainitic steel specimens charged for different times then compressed. It shows the same trend to that of the uncompressed specimens' spectra in figure 3.39, further confirming hydrogen saturation after 4 d of charging. This trend is also shown in figure 3.55.

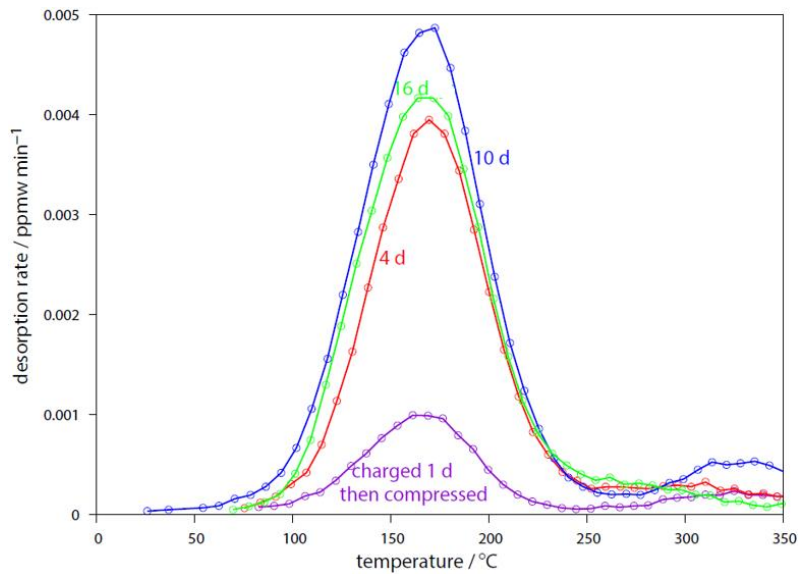


Figure 3.54: Compiled constant-heating-rate TDA spectra of compressed bainitic steel specimens charged for different times

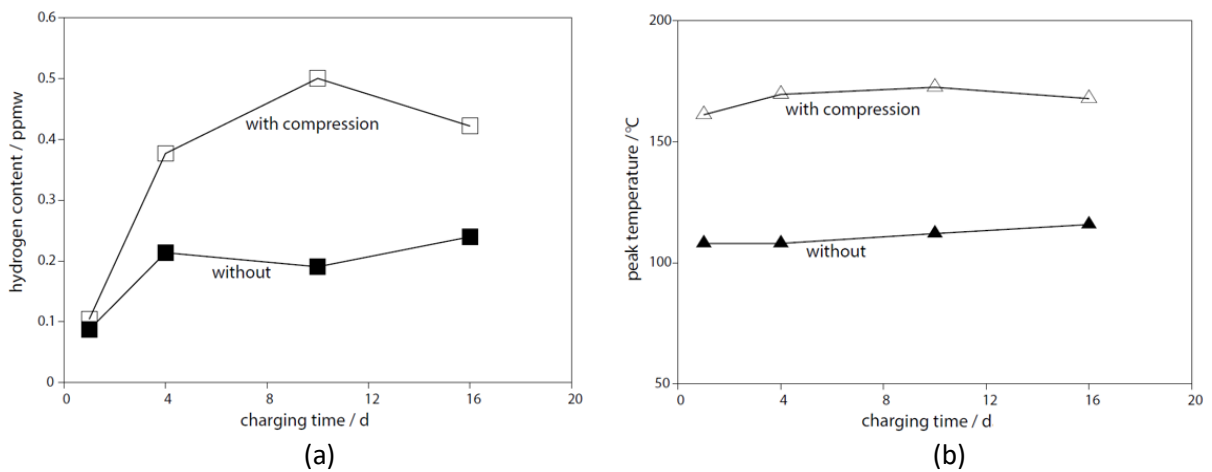


Figure 3.55: Comparison of (a) total hydrogen content, (b) peak temperature of constant-heating-rate TDA, between compressed (hollow shapes) and uncompressed (solid shapes) bainitic steel specimens charged for different times

Figure 3.55 (b) shows that, the total hydrogen content of the compressed specimens is higher than that of the uncompressed specimen. There are two reasons for this difference: Firstly, compression stopped room-temperature desorption. Therefore, hydrogen which is normally detected during room-temperature desorption, is now detected in constant-heating-rate TDA. This is because compression-induced traps have higher binding energy and once hydrogen gets trapped within them, it can no longer diffuse out easily at room temperature. Secondly, there is an additional amount of hydrogen from austenite decomposition in compressed specimens. Such hydrogen might only be released at very high temperatures in uncompressed specimens (higher than 350 °C, therefore not detected)

3.6 Effect of room-temperature aging

3.6.1 Duplex steel

For each charging condition, XRD was first performed on the specimen right after charging. XRD was later performed again on the same specimen after it has been aged for the same amount of time as charging time. No difference between these two sets of spectra was found. This indicates that aging does not affect the microstructure. The result is shown in appendix 6.8.

As shown in TDA spectra in figure 3.56 and in figure 3.57, after aging, all specimens showed reduction in total hydrogen content with the desorption peak shifted towards higher temperature, but a significant amount of hydrogen was still left. This is because the lower temperature part of the peak corresponds to release of the weakly trapped, i.e. more diffusive hydrogen atoms. These atoms desorbed easily during aging.

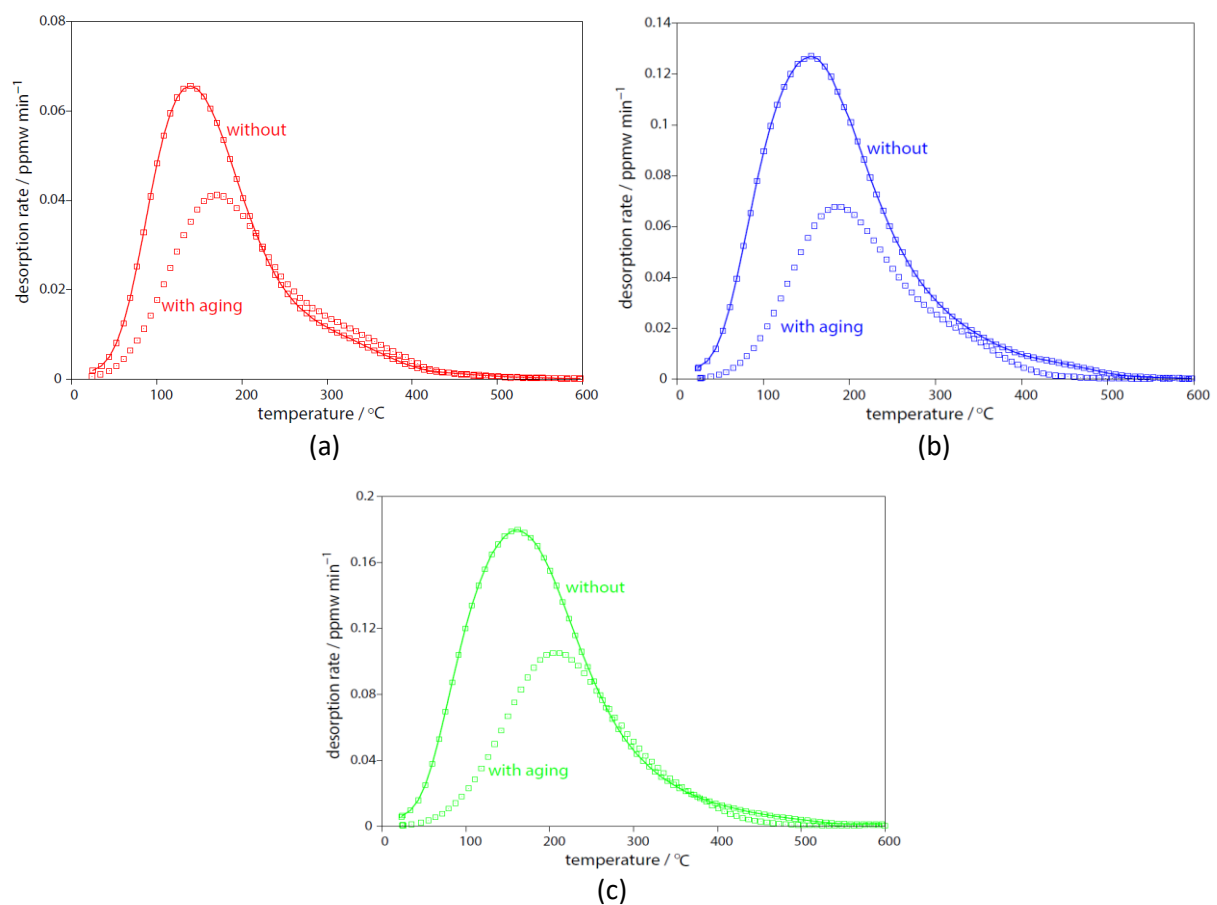


Figure 3.56: comparison of constant-heating-rate TDA spectra between aged (no line) and non-aged (solid line) duplex steel specimens charged for different times, (a) 4 d, (b) 10 d, (c) 16 d

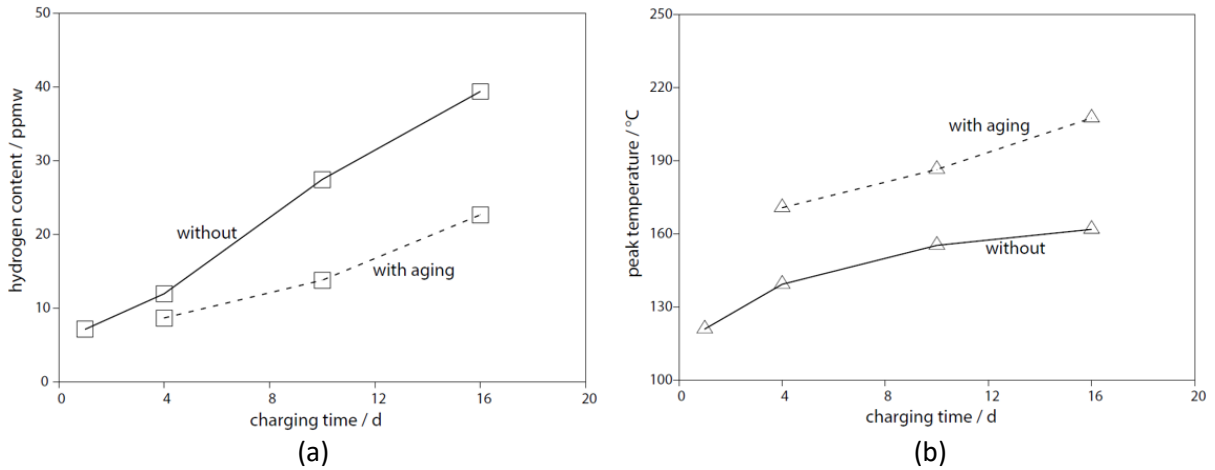
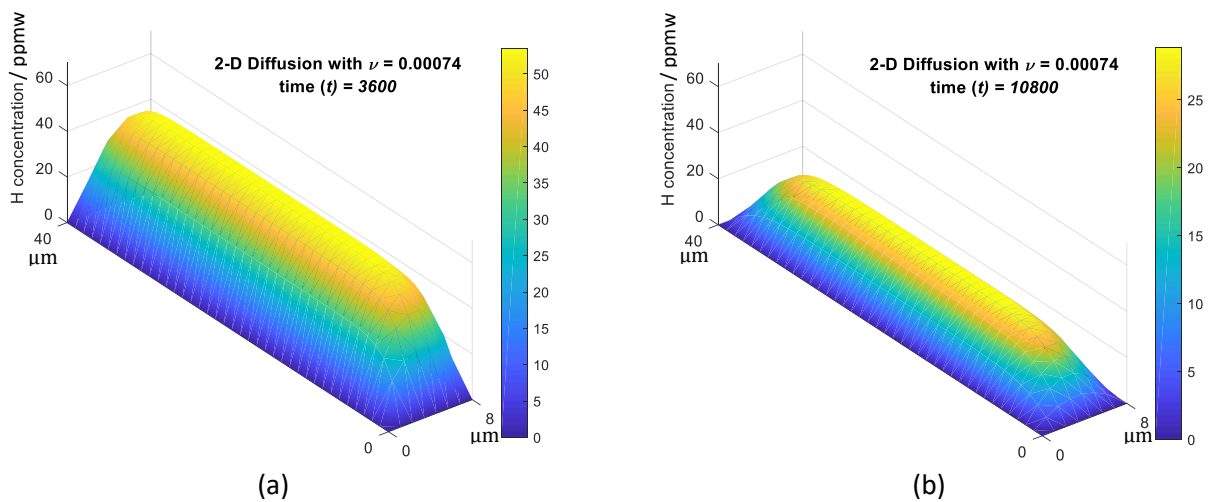


Figure 3.57: Comparison of (a) total hydrogen content (b) peak temperature of constant-heating-rate TDA between aged (dotted line) and non-aged (solid line) duplex steel specimens charged for different times

The same simulation used in section 3.3.1 was employed to simulate the desorption process in this duplex steel. It is assumed that after charging for 4 to 16 d, most hydrogen is in austenite and is evenly distributed within each grain, as simulated in section 3.3.1. Room-temperature desorption simulation was performed on the specimen which has been charged for 16 d: with 39.4 ppmw total hydrogen content and around 0.6 austenite fraction, hydrogen in each austenite grain in around 66 ppmw, which is used as our starting condition. Figure 3.58 shows its hydrogen profiles after aging for different times.



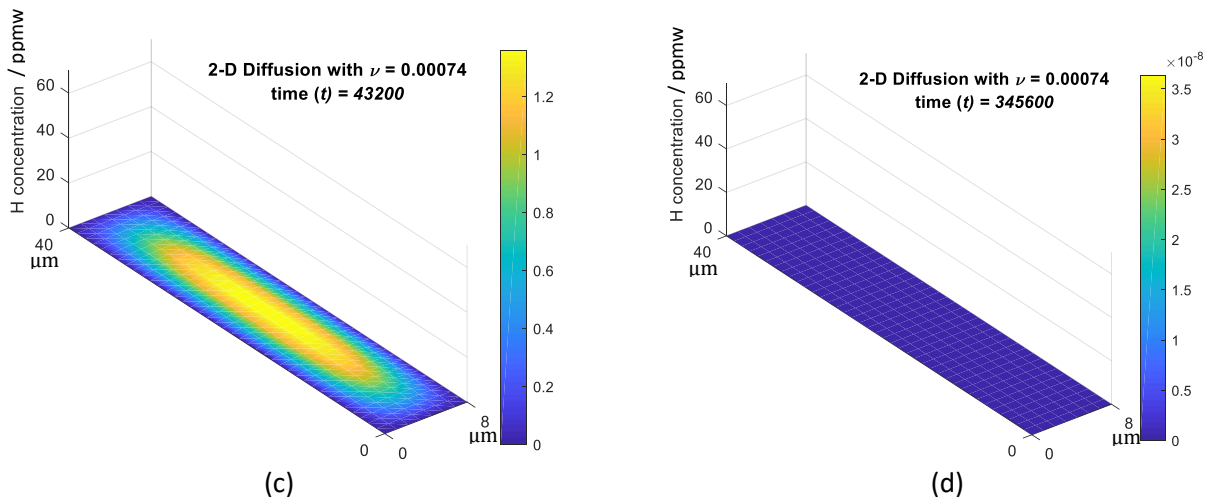


Figure 3.58: Simulated hydrogen concentration profile across an austenite grain after charging for 16 d then aged for different times, (a) 1 h, (b) 3 h, (c) 12 h, (d) 4 d. ν is the diffusion coefficient with unit of ' $\mu\text{m}^2 \text{s}^{-1}$ ' and time (t) is with unit of 's'

Most hydrogen will diffuse out after 12-h aging and all hydrogen will be completely gone after 4-d aging, as shown in figure 3.58 (d). This is very different from our experimental result as shown in figure 3.56 and 3.57. Therefore it is speculated that the ferrite/austenite interface plays an important role during the hydrogen diffusion process. Not only it affects the charging process as discussed in section 3.3.1, this interface can also serve as a barrier during aging, making it difficult for hydrogen to escape from austenite grains into the ferrite matrix.

3.6.2 Austenitic steel

All XRD spectra, like in the duplex steel, show no change after aging. This is shown in appendix 6.9.

Figure 3.59 shows that for charged austenitic specimens, after aging, both the low-temperature TDA peak and the high-temperature TDA peak changed: The low-temperature peak reduces in height and moves towards higher temperature after aging; The high-temperature peak does not shift, yet it increases in height after aging. This is most evident in figure 3.59 (b).

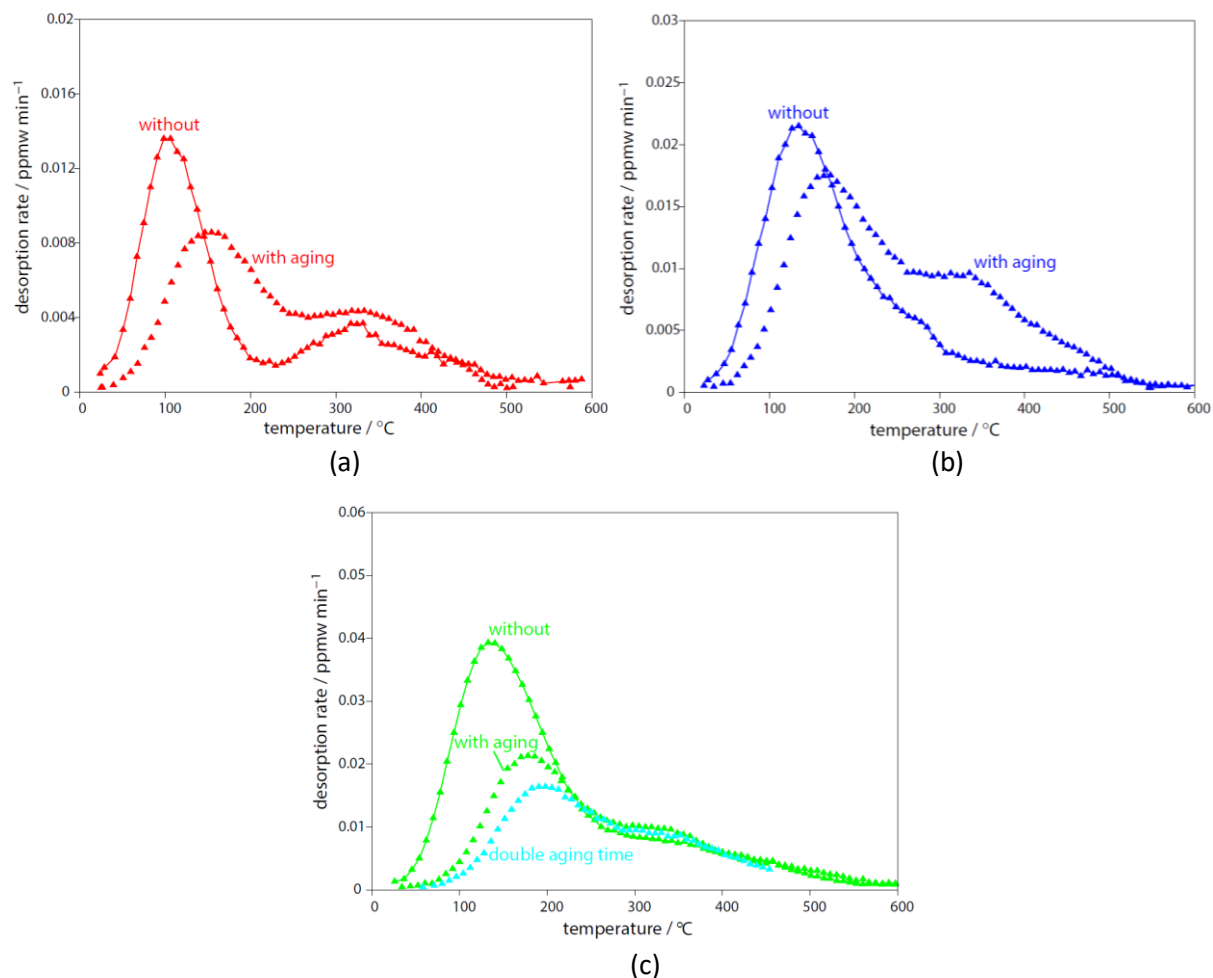


Figure 3.59: Comparison of constant-heating-rate TDA spectra between aged (no line) and non-aged (solid line) austenitic steel specimens charged for different times, (a) 4 d, (b) 10 d, (c) 16 d

The low-temperature peak change is similar to the aging behaviour of the duplex steel and the same theory can be applied here to explain this peak change. I.e. the more diffusive hydrogen diffuses out during aging. The high-temperature peak change is explained as follows: This peak corresponds to the strong/irreversible traps within this material. During aging, although no more new hydrogen is being charged into the material, the existing hydrogen atoms' distribution became more homogenised within the specimen, as shown later in the diffusion simulation in figure 3.61. These hydrogen atoms, as they diffuse further into the specimen, will encounter more of these traps and become trapped in them. And this leads to the increase in these traps' occupancy thus increase in this peak's height.

The changes in low-temperature peak and total hydrogen content are compiled in figure 3.60. In general, the hydrogen content reduced and peak shifts to higher temperature after aging, as expected. However, for specimens charged for 10 d, the total hydrogen content of the specimen with aging is higher than that of the specimen without aging. This is impossible and likely results from experimental errors during hydrogen charging.

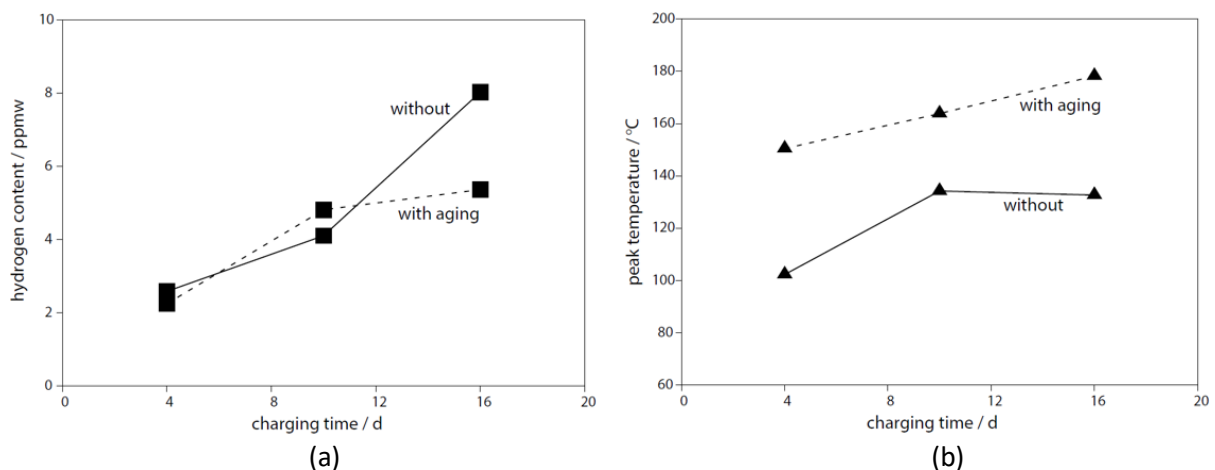


Figure 3.60: Comparison of (a) total hydrogen content, (b) peak temperature of constant-heating-rate TDA, between aged (dotted line) and non-aged (solid line) austenitic steel specimens charged for different times

Applying the diffusion model from section 3.3.2, the hydrogen profile after aging can be simulated, as shown in figure 3.61. Its corresponding total hydrogen content values were calculated and compared with the values obtained from TDA in figure 2.62.

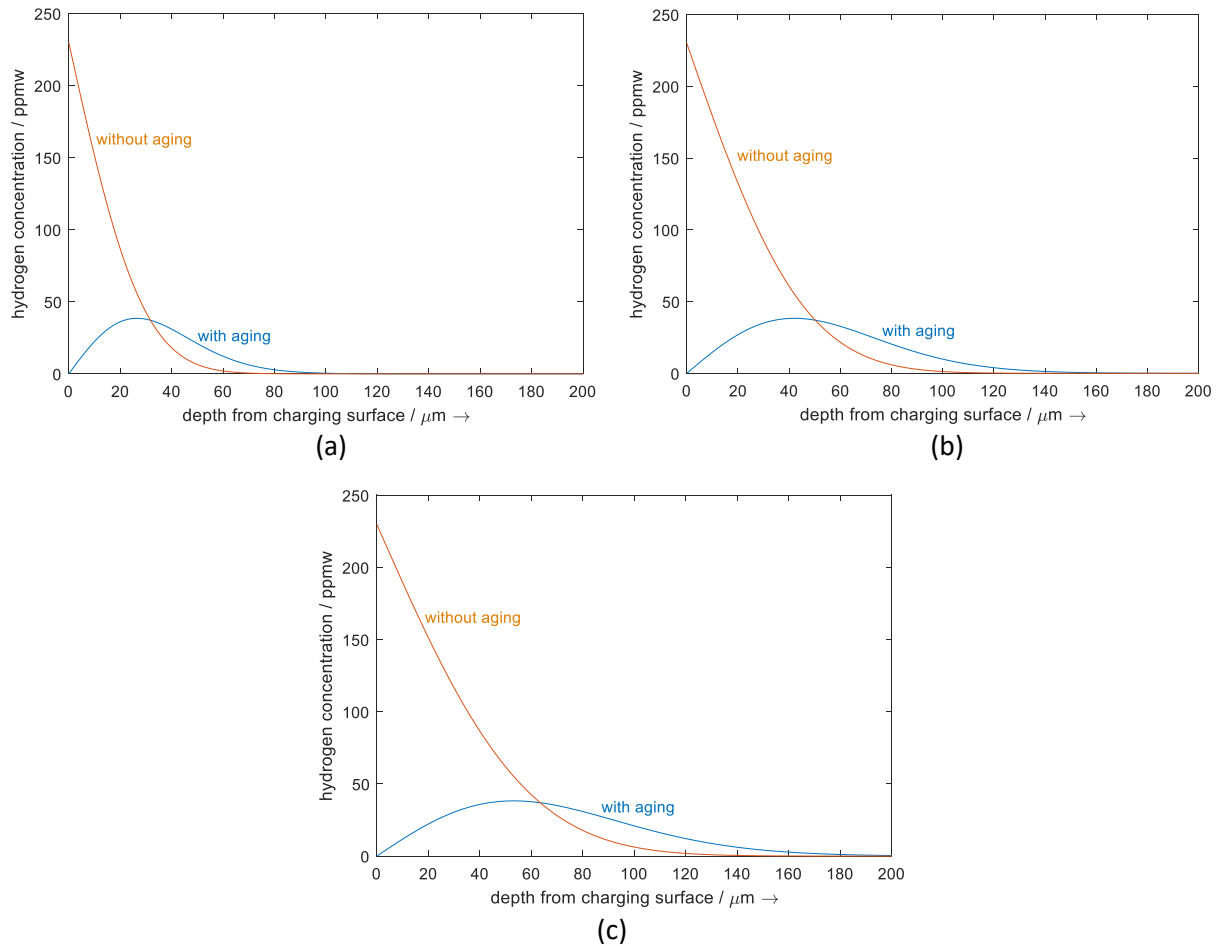


Figure 3.61: Simulated hydrogen concentration profile for austenitic steel specimens charged then aged for the same amount of time, (a) 4 d, (b) 10 d, (c) 16 d, red: without aging, blue: with aging

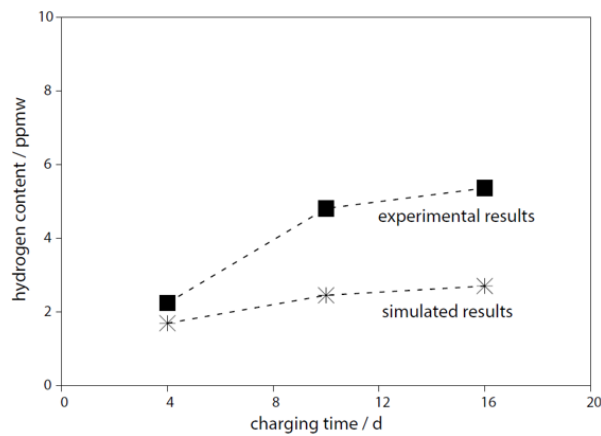


Figure 3.62: Comparison between the simulated and experimental total hydrogen content values of austenite steel specimens charged then aged for the same amount of time

For each charging with aging condition, the simulated total hydrogen content is significantly lower than the experimental result. As mentioned in section 3.3.2, this difference is because the simulation only considers diffusion in bulk austenite, other defects like delta ferrite, grain boundaries[18][20], however, might act as traps and slow down the hydrogen desorption process.

Figure 3.63 shows that, for specimens charged for 16 d, aging significantly reduces the low-temperature peak and shifts it towards higher temperature after being compressed. This indicates a reduction in the amount of newly formed diffusible hydrogen from martensitic transformation. This is because less hydrogen was inherited from austenite since hydrogen in austenite gradually diffuses out during aging. The high-temperature peak, however, was not affected much. This can be interpreted as the traps corresponding to this peak have reached their full hydrogen capacity.

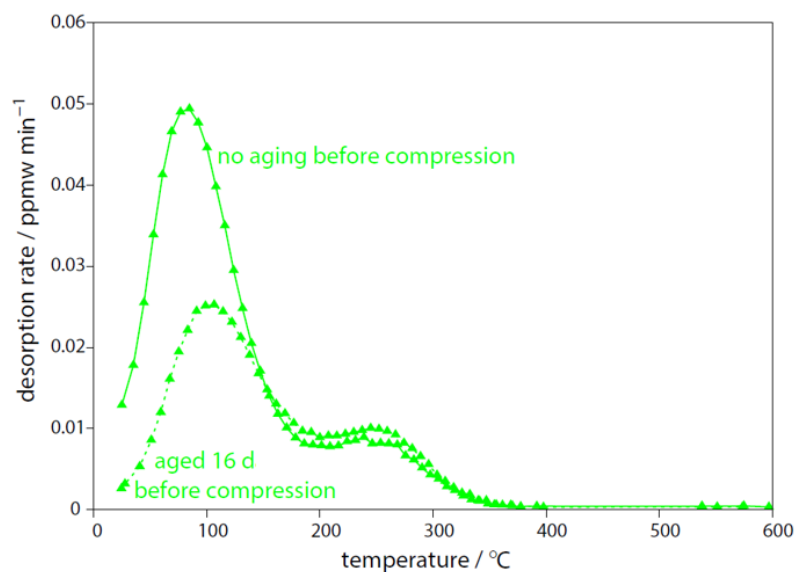


Figure 3.63: Constant-heating-rate TDA spectra of austenitic steel specimens charged for 16 d and compressed, solid line: compression straight after charging, dotted line: aged for another 16 d before compression

(Notice the difference: here in figure 3.63, the aging is done before compression, the spectra for aging after compression are presented below in figure 3.64)

Figure 3.64 shows that, for compressed specimens, aging after compression greatly reduces the low-temperature peak. This peak corresponds to the newly formed diffusive hydrogen in martensite. Due to high diffusivity, the low-temperature peak become almost completely gone after aging. This is most evident when figure 3.64 is compared with figure 3.59 and 3.63. The high-temperature peak, on the other hand, is not affected at all by aging. This is expected since the high-temperature peak corresponds to irreversible/strong hydrogen traps.

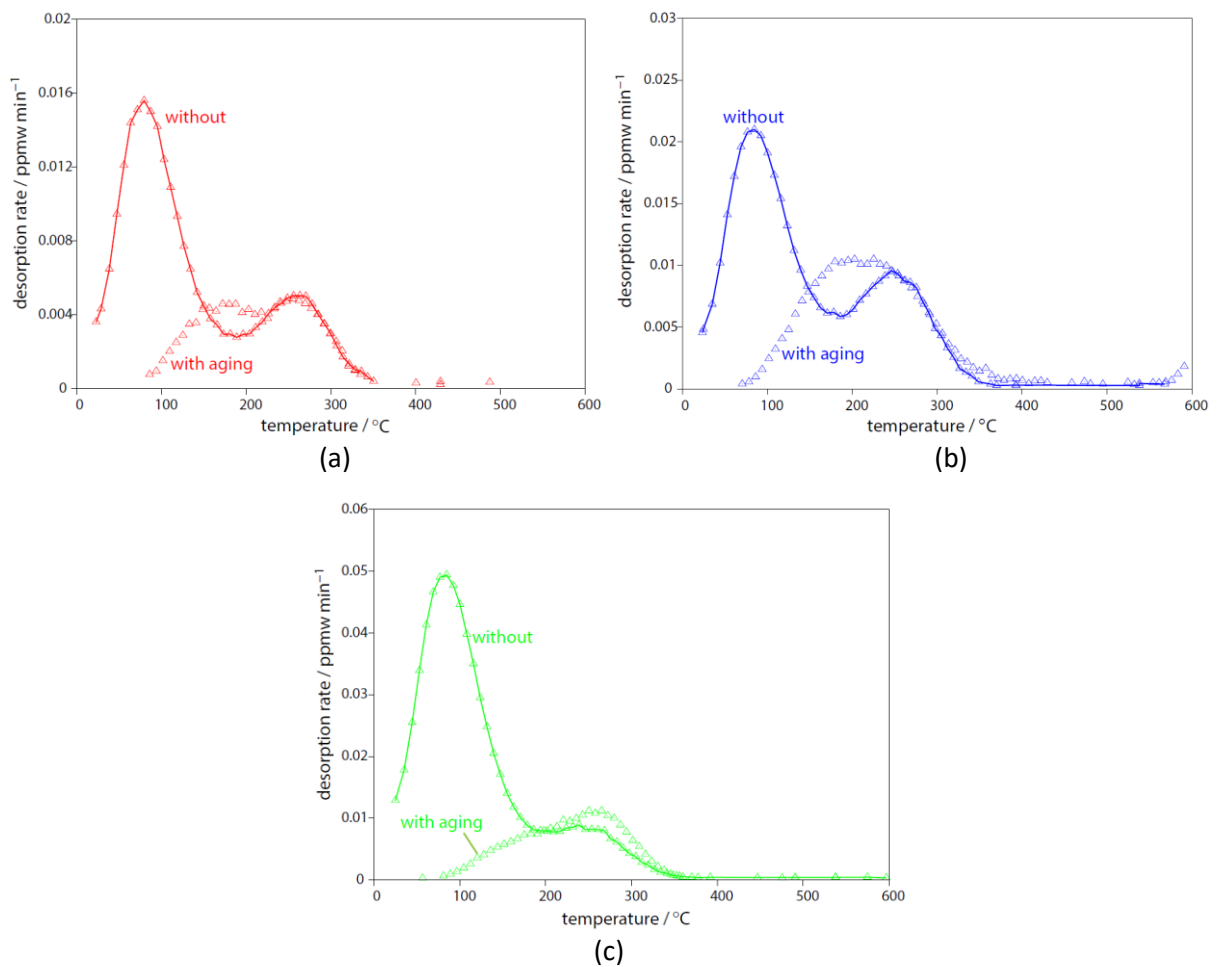


Figure 3.64: Comparison of constant-heating-rate TDA spectra between aged (no line) and non-aged (solid line) compressed austenitic steel specimens charged for different times, (a) 4 d, (b) 10 d, (c) 16 d

The activation energy of the traps corresponding to the high temperature peak was found by running TDA for austenitic specimens charged for 16 d then compressed using different heating rates:

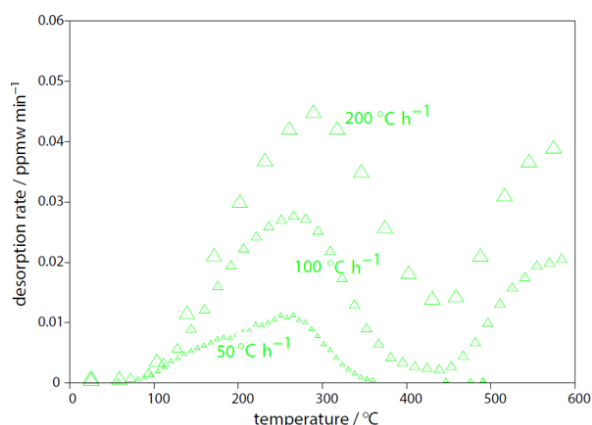


Figure 3.65: Compiled constant-heating-rate TDA spectra of austenitic specimens charged for 16 d then compressed, TDA measured at the different heating rates, small-sized triangle: 50 °C h⁻¹, medium-sized triangle: 100 °C h⁻¹, large-sized triangle: 200 °C h⁻¹

Heating rate (K h ⁻¹)	Heating rate, ϕ (K s ⁻¹)	T _c (°C)	T _c (K)	$1/T_c$	$\ln(\phi/T_c^2)$
50	0.013889	257.77	530.92	0.001884	-7.3073907
100	0.027778	265.7976	538.9476	0.001855	-7.0193956
200	0.055556	289.3572	562.5072	0.001778	-6.7555287

Table 3.13: Peak temperatures from TDA spectra run at different heating rates of austenitic specimens charged for 16 d then compressed

By plotting $1/T_c$ against $\ln(\phi/T_c^2)$ from figure 3.65, as compiled in table 3.13, the traps' activation energy E_a is found using equation 31:

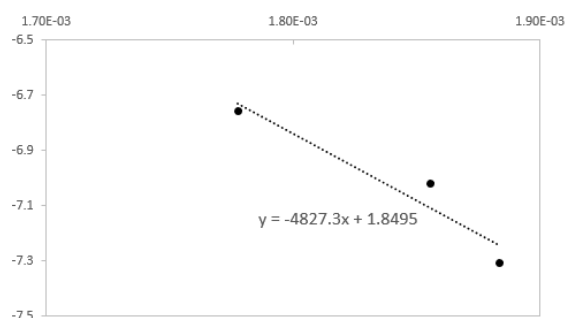


Figure 3.66: Plot of $1/T_c$ against $\ln(\phi/T_c^2)$ from table 3.13

$$\text{Slope} = -\frac{E_a}{R} \approx -4827.3, \text{ therefore, } E_a = 4827.3 \times R = 40.13 \text{ kJ mol}^{-1}$$

3.6.3 Bainitic Steel

For non-compressed specimens, almost all hydrogen desorbed during aging. Due to the time limit, no aging tests on compressed specimens were performed. XRD was performed, showing no change after aging for compressed and non-compressed specimens. This is in appendix 6.10

3.7 Other interesting desorption results from side experiments

3.7.1 Sample size effect on bainitic steel

A smaller, 1/4-sized specimen was cut from the standard 8 mm diameter specimen after being charged and compressed. Its TDA peak is thinner but taller than the standard-sized specimen. And it is around 18°C lower. This is because, in smaller specimens, hydrogen can more easily diffuse to the surface and desorb.

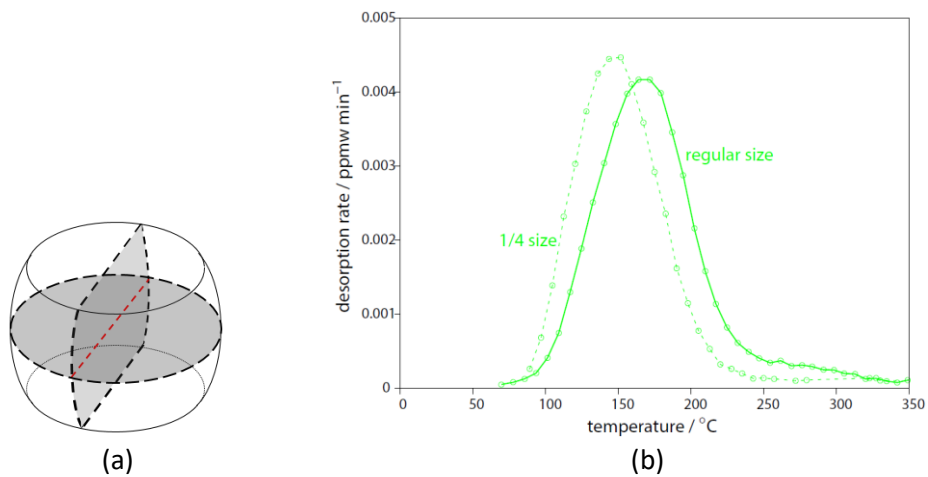


Figure 3.67: Comparison of TDA spectra of compressed bainitic specimens of different size which have been both charged for 16 d

3.7.2 Strain-induced increase in hydrogen content in bainite

(Notice: up until this point, all specimens were compressed after hydrogen charging.)

Figure 3.68 shows a significant increase in the hydrogen content when the specimen is compressed before hydrogen charging. This is due to strain-induced defects as hydrogen traps which increase the material's overall hydrogen solubility.

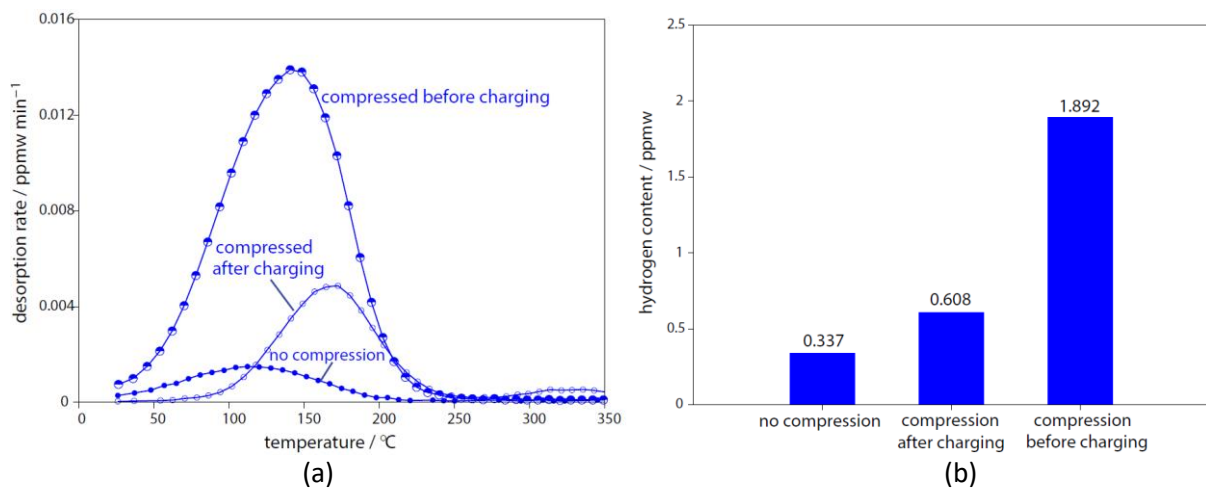


Figure 3.68: Comparison of TDA spectra of bainitic specimens with different compression conditions which have been charged for 10 d

Just like for uncompressed or compression-after-charging specimens, the compressed specimens are saturated with hydrogen after 4 d of charging:

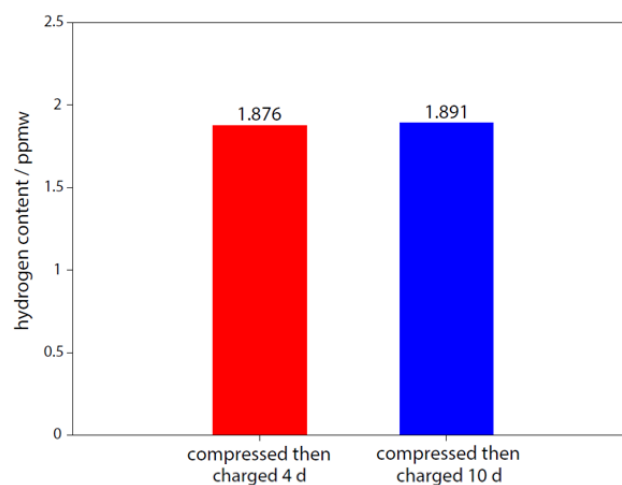


Figure 3.69: Comparison of hydrogen content of bainitic specimens compressed then charged for 4 d (red) or 10 d (blue)

Figure 3.70 shows that, for specimens which have been compressed then charged, the total hydrogen content kept decreasing and the TDA peak shifted towards higher temperature. After 1-month aging, a small peak was still detected, and this peak is in the same position as the peak in section 3.5.3. This is because both types of these peaks result from strain-induced defects.

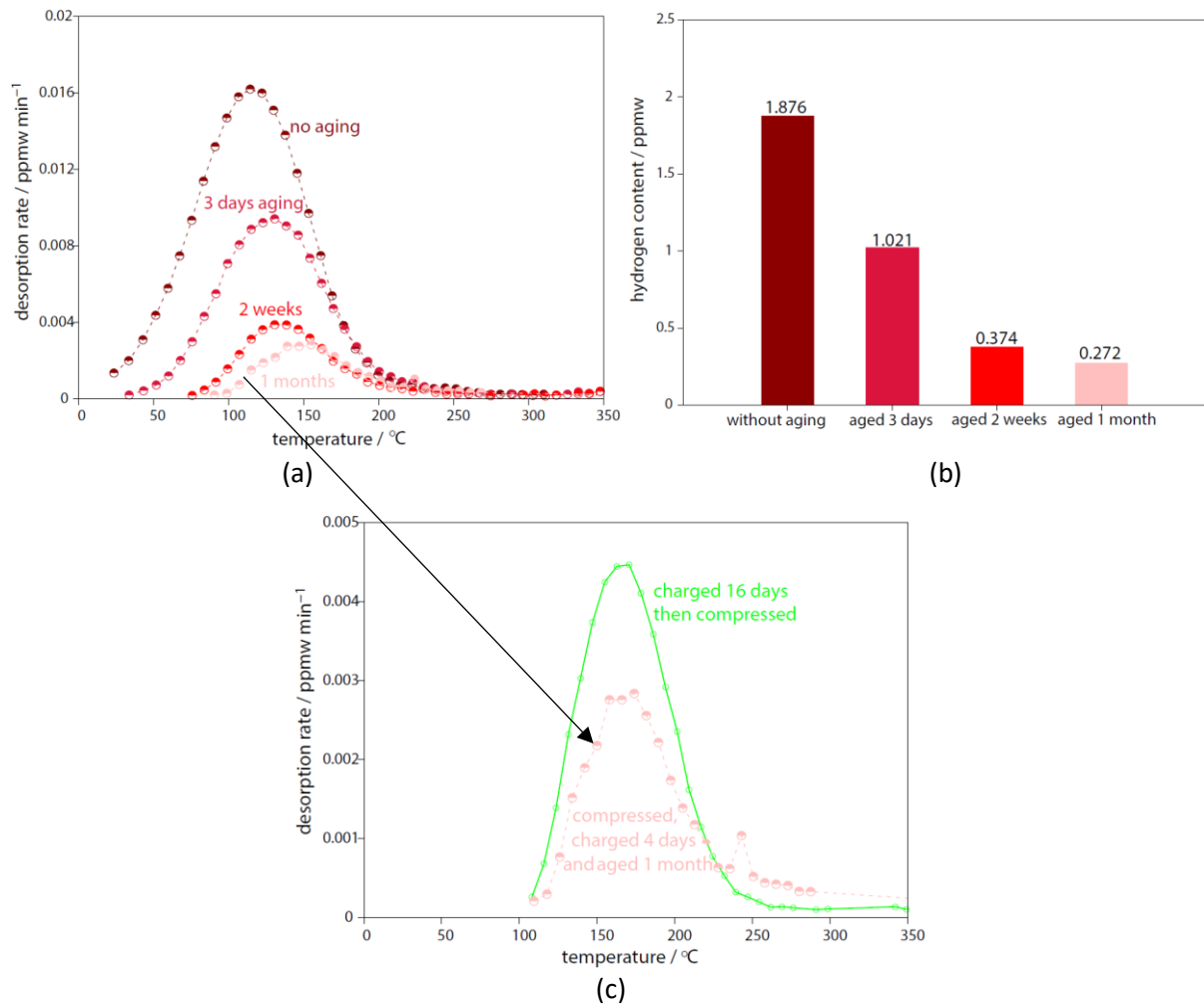


Figure 3.70: (a) & (b) show aging of compressed and charged $\frac{1}{4}$ -sized specimens, (a) constant-heating-rate TDA spectra (b) corresponding hydrogen content (c) compares peak position between a 'compression-before-charging' specimen aged for 1 month and a 'compression-after-charging' specimen without any aging, both specimens are of the same size

3.7.3 Hydrogen-enhanced strain-induced defects in bainite

Figure 3.71 shows that for ‘compression-before-charging’ specimens, there is a quite noticeable increase in hydrogen content if the specimen was pre-charged with hydrogen before compression. This is because the pre-charged hydrogen enhanced the formation of defects during compression, which is consistent with the HESIV in section 1.1. This increase in the number of defects means there are more traps. Therefore, more hydrogen can stay in the compressed specimen with pre-charging.

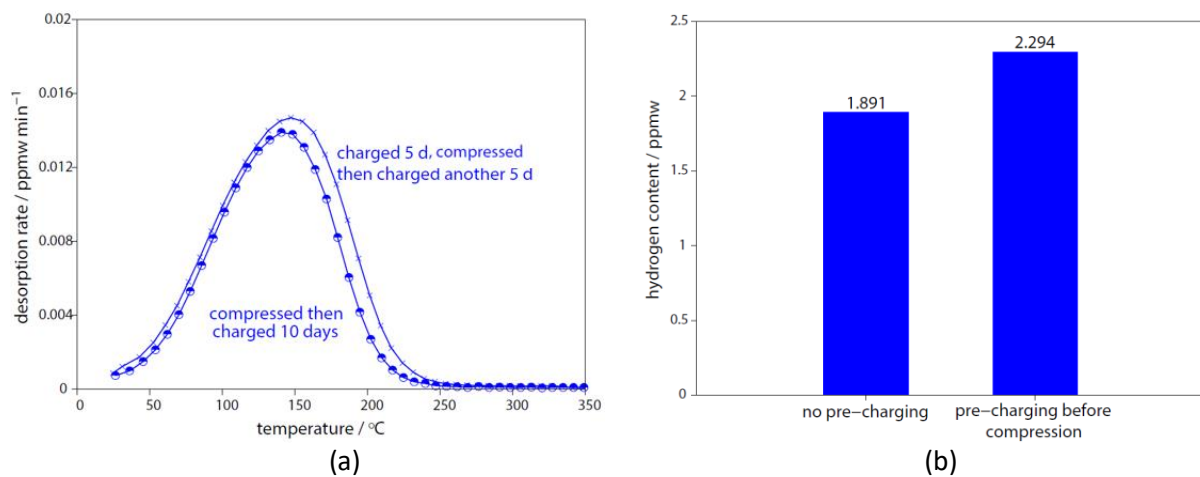


Figure 3.71: Comparison of hydrogen content of bainitic specimens compressed then charged between specimens with and without hydrogen pre-charging before compression

3.8 Visualization of hydrogen

As explained in section 1.5, all microprinting was performed on the hydrogen charged surfaces to identify hydrogen-rich sites unless stated otherwise.

3.8.1 Duplex steel

Figure 3.72 shows that, much of the desorbed hydrogen is from austenite grains. This is because austenite has much higher solubility. Individual silver particles colonizing an austenite grain can be seen in (c).

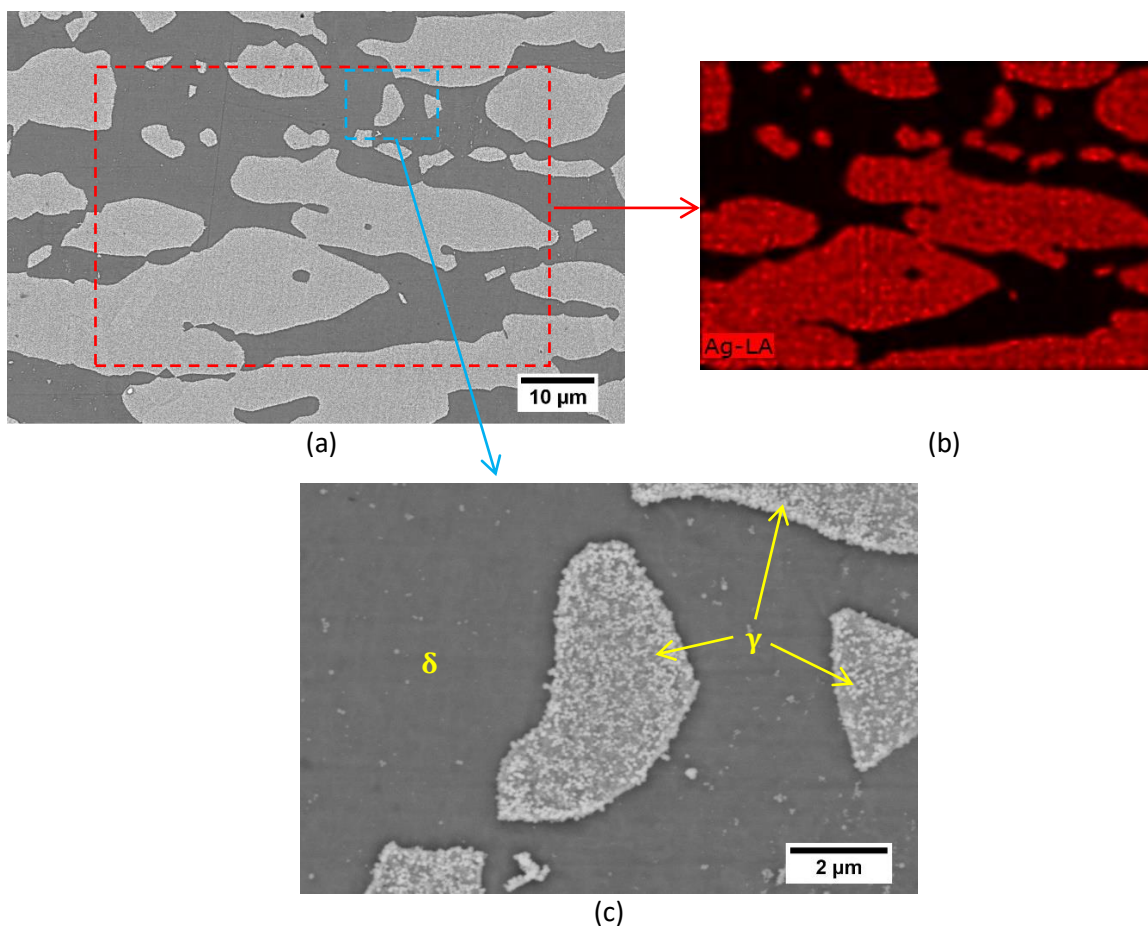


Figure: 3.72: Microprinted image of as-received duplex steel after charging for 2 h, (a): overall view at low magnification; (b): EDS mapping of Ag from the red dotted box in (a), (c): magnified image of an austenite island from (a)

3.8.2 Austenitic steel

Figure 3.73 shows an even distribution of desorbed hydrogen on the microstructure. Neither annealing twin nor grain boundary is a preferential site for hydrogen. This is further confirmed by (b) where the EDS line scan across a grain boundary shows no difference in Ag counts.

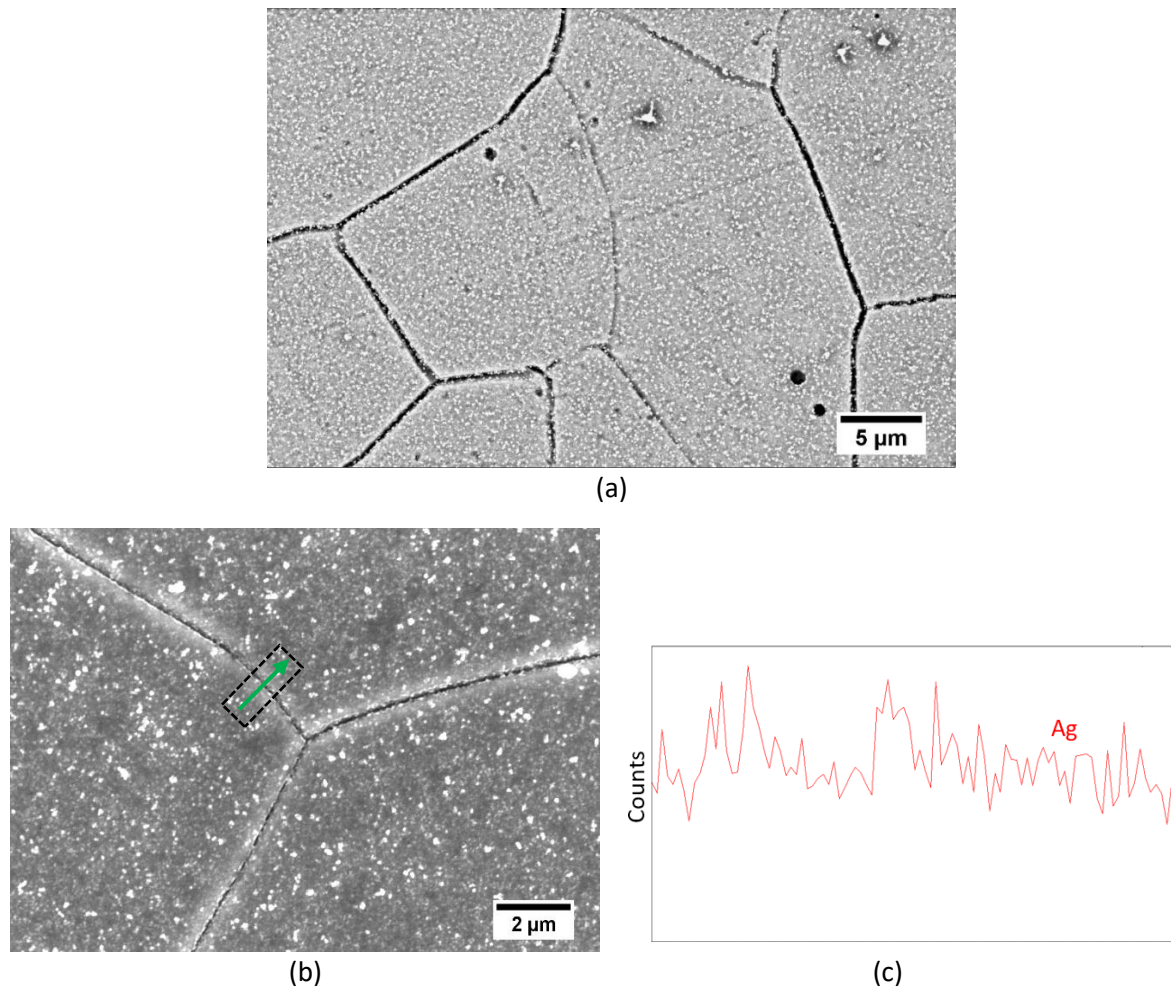
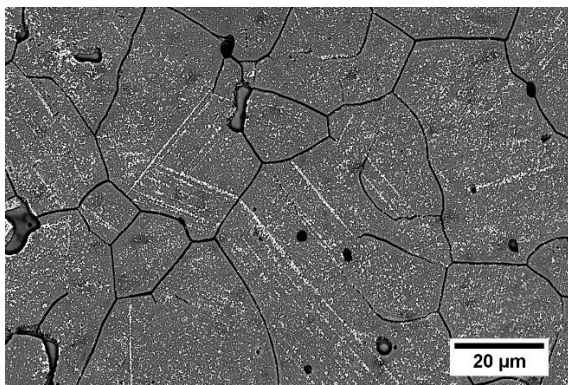
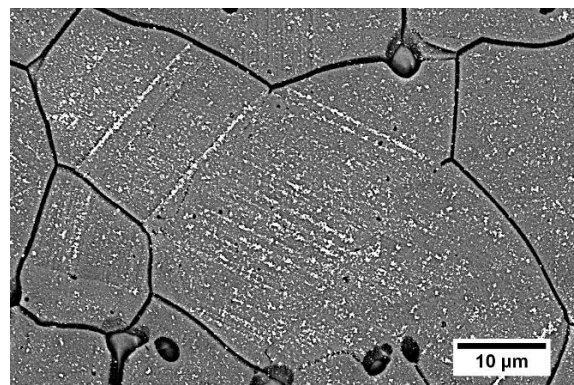


Figure: 3.73: Microprinted image of as-received austenitic steel after charging for 2 h (a) overall view at low magnification; (b)&(c): EDS line scan across a grain boundary

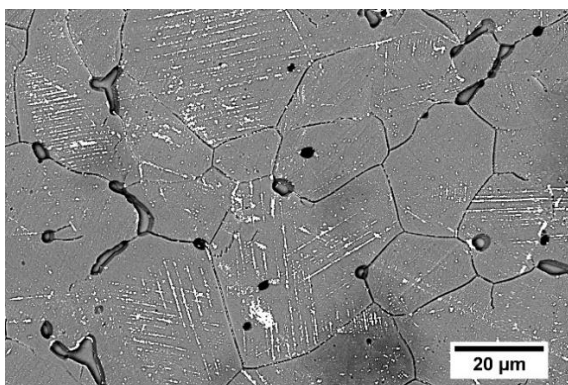
Figure 3.74 is rather exciting, since, by only using microprinting, it directly shows that dislocations can carry hydrogen atoms with them when they move, confirming dislocations' ability to trap hydrogen atoms. After 2 h charging, the specimen was slightly strained by 5% and microprinted. Among the background, preferential deposition of silver particles on slip bands was seen, as shown in figure 3.74 (a) and (b). However, if the specimen was aged for another 2 h after charging but before compression and microprinting. Then, most hydrogen near sample surface would have diffused out. The microprinted surface is now free of background silver atoms but the preferential deposition on slip bands is still there and become more distinct, as in (c) and (d). Figure (e) and (f) confirms there is no preferential deposition of Ag on slip bands if the deformation took place before hydrogen charging.



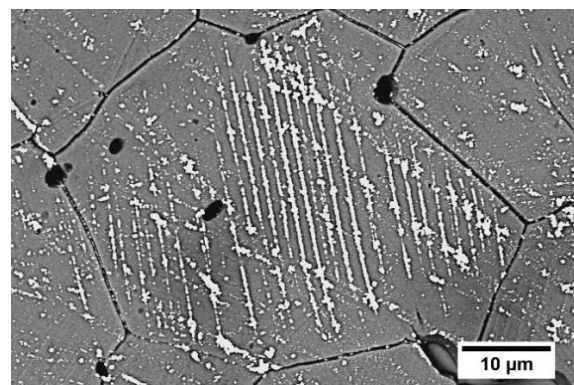
(a)



(b)



(c)



(d)

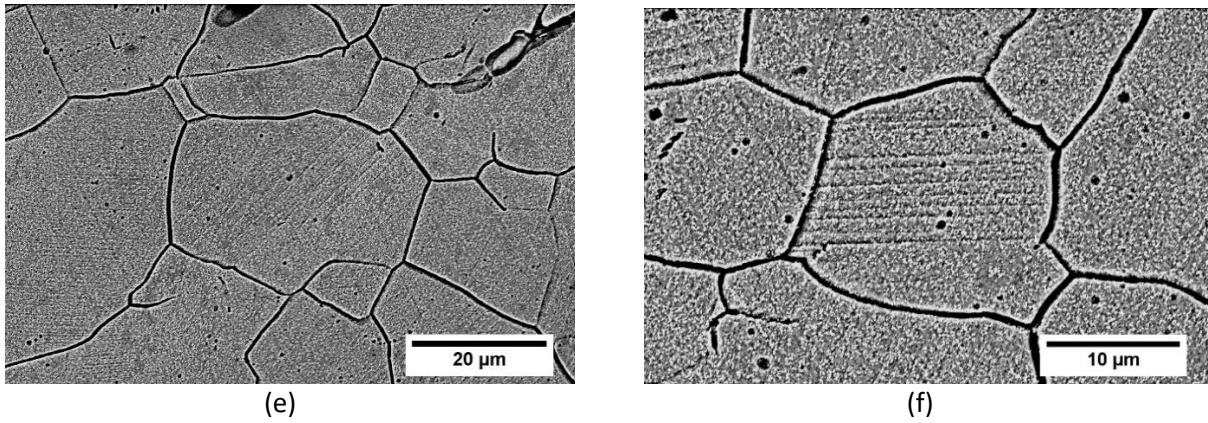


Figure: 3.74: Microprinted image of lightly-strained (5%) austenitic steel charged for 2 h (a)&(b): charged then strained without aging; (c)&(d): charged and aged for 2 h, then strained; (e) & (f): strained before charging

Therefore, the results shown in figure 3.74 (c) and (d) have shown dislocations' ability to drag along hydrogen with them during deformation. This is illustrated in figure 3.75: after aging, little hydrogen was still left near the specimen surface. However, when it is strained, the moving dislocation drags hydrogen with it from the bulk to the specimen surface, where hydrogen reduces the AgBr to Ag atoms, which left the preferential Ag deposition along slip bands as shown in figure 3.74 (c) and (d).

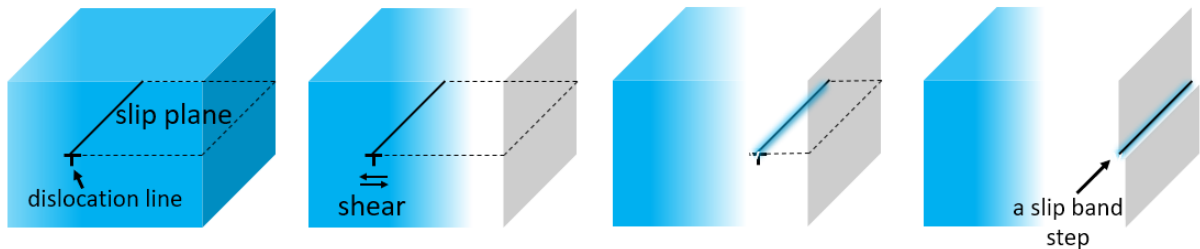


Figure: 3.75: Schematic demonstrating how the results from figure 3.74 (c)&(d) were formed

3.8.3 Bainitic steel

Like duplex steel, most hydrogen desorbs from austenite grain. However, some silver particles also deposited outside the austenite grains. This suggests the ferrite/austenite interface might be another hydrogen-rich region, i.e. possible hydrogen trap.

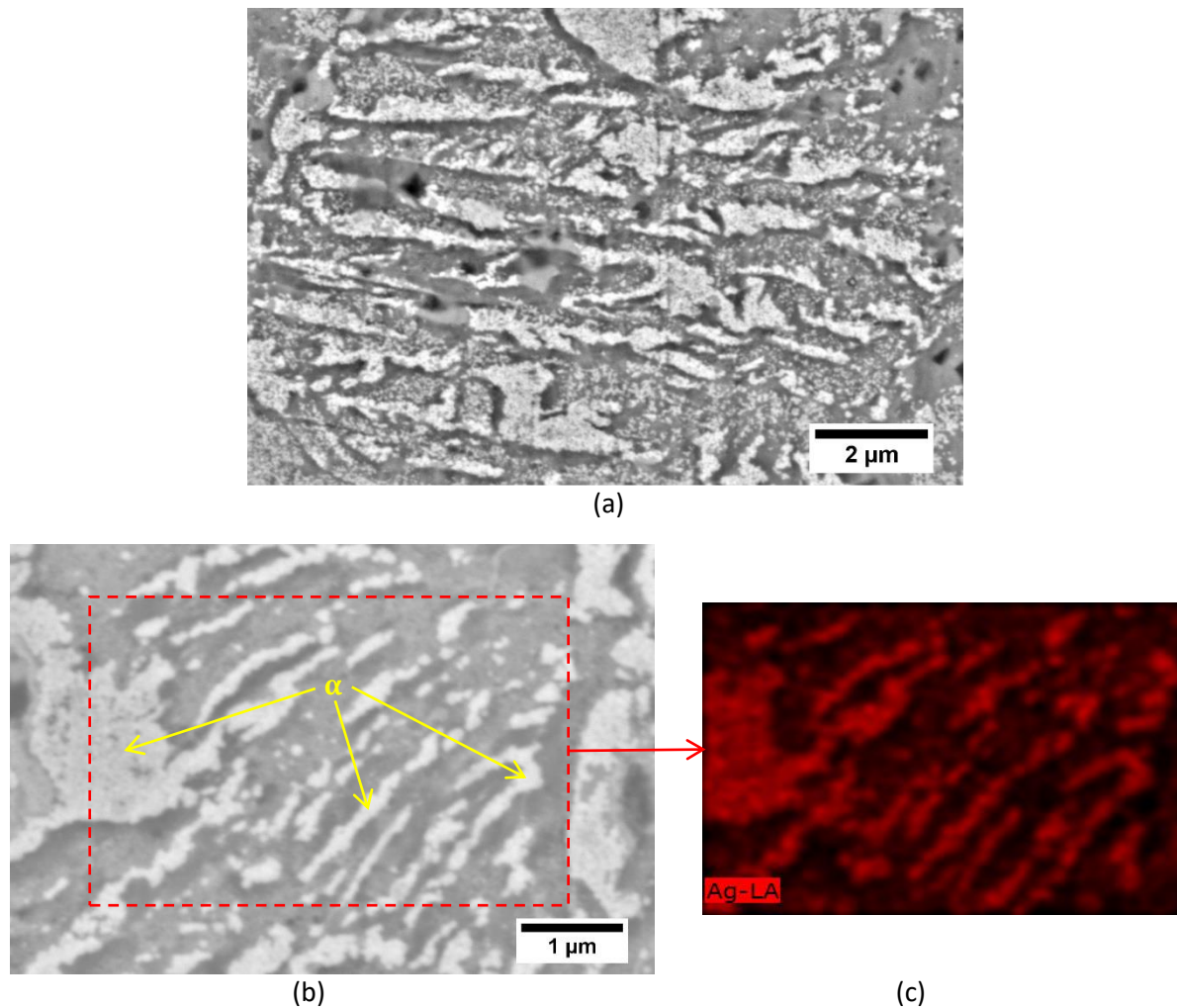


Figure 3.76: Microprinted image of as-received bainitic steel after charging for 2 h, (a): overall view at low magnification, (b): higher magnification image; (c): EDS mapping of Ag from the red dotted box in (b)

Fast-diffusion-path tests, as described in section 1.5, were also performed on the bainitic steel, as shown in figure 3.77. Surprisingly, the result is the same as in figure 3.76, i.e. silver particles preferentially deposit on austenite. This result was also obtained by J. A. Ronevich [68]. This result suggests that hydrogen diffuses fastest in austenite, which cannot be true. The explanation given by Rinevich for such observation was that hydrogen preferentially diffuse via grain boundary. This explanation is not satisfactory since the Ag distribution is uniform on austenite grains rather than segregating towards grain boundaries.

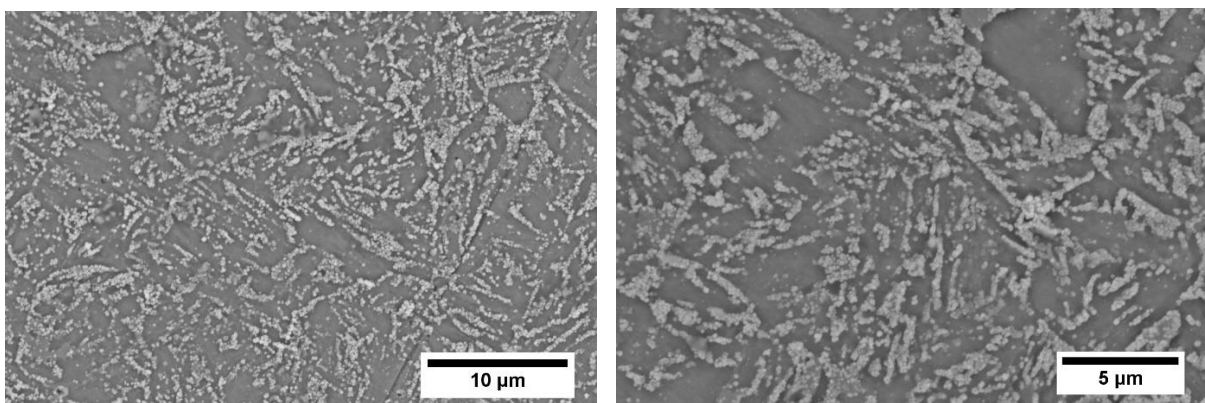


Figure: 3.77: Microprinted image of as-received bainitic steel after charging for 2 h from the opposite surface for fast-diffusion-path tests

After many repeated experiments, it was found that the plastic lacomit protective film, was often lifted up and it formed a balloon by the hydrogen diffused and exited from the microprinted side. This is a locally high hydrogen concentration environment, in which hydrogen back diffused onto the surface austenite on the microprinted side. This is likely to be the actual cause of the counterintuitive results in figure 3.77. To avoid this issue, a better set up used by Ichitani [69] can be employed for more accurate fast-diffusion-path detection, in which hydrogen is being charged through one side while microprinting is being performed simultaneously on the other side. This method avoids the use of protective plastic film.

4. Conclusions

The change in hydrogen desorption behaviour after compression is different for the three different types of steel studied. Such change depends strongly on the dissolved hydrogen concentration and the amount of phase transformation within each type of steel:

1. For the austenitic steel, with high hydrogen concentration (up to around 8 ppmw) and significant phase transformation to martensite (up to 82%) after compression, a significant burst in hydrogen desorption rate was detected. This is because hydrogen has much higher solubility in austenite than in ferrite. After phase transformation, martensite could not dissolve all the hydrogen inherited from the decomposed austenite, leaving most of the hydrogen in a highly mobile state in the martensite lattice, which then desorbed rapidly out of the specimen. (hydrogen is also much more diffusive in martensite than in austenite)

2. For the bainitic steel, with very low hydrogen concentration (up to around 0.5 ppmw) and a little phase transformation to martensite (less than 8%) after compression, a significant reduction in hydrogen desorption was detected. This is due to the formation of newly strain-induced defects which were capable of trapping not only the existing diffusive hydrogen but also any possible additional hydrogen released from the decomposed austenite. These newly formed traps led to an overall reduction in hydrogen diffusivity.

3. For the duplex steel, with no phase transformation, its hydrogen behaviours did not change significantly due to compression. The only difference in this case after compression was the possible deformation-induced traps. However, either these traps were not as effective as in bainitic steels, or their hydrogen trapping capacity was simply too insignificant compared to the total hydrogen charged into the material (up to 40 ppmw)

By comparing the simulation and the experimental results from TDA, it was found that for both the austenitic steel and the duplex steel, the ferrite/austenite interfaces seem very likely to be

playing a very important role during the diffusion process and may act as an accumulation site for hydrogen.

From the microprinting results, it was found that in both the bainitic steel and the duplex steel, austenite grains shows preferential Ag deposition, i.e. hydrogen-rich sites. In the austenitic steel, it has been shown that dislocation can drag hydrogen atoms with it during plastic deformation.

Overall, martensite transformation is something to be avoided in austenite-containing materials used in high-hydrogen-concentration environments. It will generate diffusive hydrogen which will lead to embrittlement and martensite itself is more prone to embrittlement. Strain-induced defects such as dislocations, voids etc. can trap diffusive hydrogen to a certain extent. They are particularly effective when hydrogen concentration is low. However, whether these traps are good for embrittlement improvement is still debatable since it is unknown if these hydrogen atoms can lead to local plasticity thus crack initiation locally at these trap sites.

5. Lessons learnt from failed attempts and future work

1. Ammonia thiocyanate (poison) cannot be used for high temperature electrochemical hydrogen charging. It reacts with steel rapidly at temperatures over 60 °C and forms a black layer which stops further charging.
2. Duplex steel corrodes rapidly during charging at high temperature in saltwater even without using poison.
3. Conventional microprinting should not be applied at elevated temperature. Horikawa [70] has done microprinting up to 260 °C to reveal high energy traps. Many trials have been done to replicate this experiment. But at any temperature above 120 °C, even only for 1 min, the heat itself can lead to large amount of Ag deposition on samples' surface, even for non-charged samples.
4. Data processing and report writing takes long time, should have started earlier

Possible Future work:

This work shows that hydrogen can be released from austenite decomposition into martensite. This hydrogen release can be used to help explain the previously reported hydrogen embrittlement behaviours in austenitic and TRIP steels which has only been ascribed to the change in overall hydrogen diffusivity due to deformation. This allows people to develop a better understanding of the embrittlement behaviours of these steels in order to avoid such problem. This work also shows that deformation-induced defect can greatly traps diffusive hydrogen. In the future, better correlations should be made between these changes in the hydrogen trapping states due to deformation and the mechanical properties of the materials. For example, in-situ desorption/mechanical tests can be performed to correlate hydrogen release rate with the deformation and the phase transformation process. Steels which exhibit hydrogen trap state change due to either phase transformation or trap generation (for example, the austenitic steel or the bainitic steel) should be charged with various amount of hydrogen and then tested mechanically to better quantify the embrittlement effects of phase transformation and its resultant hydrogen state change. This can help us better understand the role of phase transformation in the hydrogen embrittlement process and allow us better to mitigate the hydrogen embrittlement in these materials.

References

- [1] W. H. Johnson, 'On some remarkable changes produced in iron and steel by the action of hydrogen and acids', *Proceedings of the Royal Society of London*, Vol. 23 (1875), pp. 168–179
- [2] H. Benneck, H. Schenck, H. Muller, 'Die Entstehungsursache der Flocken im Stahl', *Stahl Eisen*, Vol. 55 (1935), pp. 321
- [3] D. P. Escobar, C. Miñambres, L. Duprez, K. Verbeken, M. Verhaege, 'Internal and surface damage of multiphase steels and pure iron after electrochemical hydrogen charging', *Corrosion Science*, Vol. 53 (2011), pp. 3166–3176
- [4] N. J. Petch, P. Stables, 'Delayed Fracture of Metals under Static Load', *Nature* Vol. 169 (1952), pp. 842
- [5] N. J. Petch, 'The lowering of fracture-stress due to surface adsorption', *The Philosophical Magazine: A Journal of Theoretical Experimental and Applied Physics*, Vol. 3 (1958), issue 34, pp. 331-337
- [6] T. Tabata, H. K. Birnbaum, 'Direct observations of the effect of hydrogen on the behavior of dislocations in iron', *Scripta Metallurgica*, Vol. 17 (1983), issue 7, pp. 947-950
- [7] H. K. Birnbaum, P. Sofronis, 'Hydrogen-enhanced localized plasticity-a mechanism for hydrogen-related fracture', *Materials Science and Engineering: A*, Vol. 176 (1994), pp. 191-202
- [8] M. Nagumo, 'Hydrogen related failure of steels – a new aspect', *Materials Science and Technology*, Vol. 20 (2004), pp. 940-950
- [9] M. Nagumo, M. Nakamura, K. Takai, 'Hydrogen thermal desorption relevant to delayed-fracture susceptibility of high-strength steels', *Metallurgical and Materials Transactions A*, Vol. 32 (2001), issue 2, pp. 339–347
- [10] K. Takai, H. Shoda, H. Suzuki, M. Nagumo, 'Lattice defects dominating Hydrogen-related failure of metals', *Acta Materialia*, Vol. 56 (2008), issue 18, pp. 5158-5167
- [11] A. R. Troiano, 'The Role of Hydrogen and Other Interstitials in the Mechanical Behavior of Metals', *Transactions of American Society for Metals*, Vol. 52 (1960), pp. 54–80
- [12] D.G. Westlake, 'Generalized model for hydrogen embrittlement', *Transactions American Society for Metals*, Vol. 62 (1969), pp. 1000–1006
- [13] K. Takai, R. Watanuki, 'Hydrogen in Trapping States Innocuous to Environmental Degradation of High-strength Steels', *ISIJ international*, Vol. 43 (2003), issue 4, pp. 520-526
- [14] H. Hagi, 'Diffusion Coefficient of Hydrogen in Iron without Trapping by Dislocations and Impurities', *Materials Transactions, JIM*, Vol. 35 (1994), issue 2, pp. 112-117
- [15] H. Katsuta, K. Furukawa, 'Hydrogen and Deuterium Transport through Type 304 Stainless Steel at Elevated Temperatures', *Journal of Nuclear Science and Technology*, Vol.18 (1981), issue 2, pp. 143-151
- [16] J. Crank 'The mathematics of Diffusion', *Oxford University Press*, second edition (1975), pp. 14
- [17] G. R. Caskey Jr., 'Hydrogen Degradation of Ferrous Alloys', *Noyes Publications*, Park Ridge, (1985)
- [18] H.K.D.H. Bhadeshia, 'Prevention of Hydrogen Embrittlement in Steels', *ISIJ International*, Vol. 56 (2016), no. 1, pp. 24-36
- [19] K. Yamakawa, T. Tsuruta, S. Yoshizawa, 'Interaction between Dislocation and Hydrogen Occluded in Single Crystal of Iron', *Corrosion Engineering*, Vol. 30 (1981), issue 8, pp. 443-449
- [20] R. A. Oriani, 'The diffusion and trapping of hydrogen in steel', *Acta Metallurgica*, Vol.18 (1970), issue 1, pp. 147-157
- [21] J. P. Hirth, 'Effects of hydrogen on the properties of iron and steel', *Metallurgical Transactions A*, Vol. 11 (1980), issue 6, pp. 861-890

-
- [22] Y. Mine, Z. Horita, Y. Murakami, 'Effect of high-pressure torsion on hydrogen trapping in Fe-0.01 mass% C and type 310S austenitic stainless steel', *Acta Materialia*, Vol. 58 (2010), pp. 649–657
- [23] L. S. Darken, R. P. Smith, 'Behavior of Hydrogen in Steel During and After Immersion in Acid', *Corrosion*, Vol.5 (1949), pp. 1-16
- [24] M. L. Hill, E. W. Johnson 'Hydrogen in cold worked Iron-Carbon alloys and the mechanism of hydrogen embrittlement', *Transactions of the metallurgical society of AIME*, Vol. 215 (1959), pp. 717
- [25] A. McNabb, P. K. Foster, 'A new analysis of the diffusion of hydrogen in iron and ferritic steels', *Transactions of Metallurgical Society of AIME*, Vol. 227 (1963), pp. 618
- [26] H. Shoda, H. Suzuki, K. Takai, Y. Hagiwara, 'Hydrogen Desorption Behavior of Pure Iron and Inconel 625 during Elastic and Plastic Deformation', *ISIJ International*, Vol.50 (2010), pp. 115– 123
- [27] C. M. Sturges, A. P. Miodownik, 'The interaction of hydrogen and dislocations in iron', *Acta Metallurgica*, Vol. 17 (1969), issue 9, pp. 1197-1207
- [28] M. Nagumo, 'Fundamentals of hydrogen embrittlement', *Springer* (2016)
- [29] T. Tabata, H. K. Birnbaum, 'Direct observations of hydrogen enhanced crack propagation in iron', *Scripta Metallurgica*, Vol. 18 (1984), issue 3, pp. 231-236
- [30] G. K. Williamson, W. H. Hall, 'X-ray line broadening from filed aluminium and wolfram', *Acta Metallurgica*, Vol. 1 (1953), issue 1, pp 22-31
- [31] M. Nagumo, K. Ohta, H. Saitoh, 'Deformation induced defects in iron revealed by thermal desorption spectroscopy of Tritium', *Scripta Materialia*, Vol. 40 (1999), no. 3, pp. 313–319
- [32] M. Aoki, H. Saito, M. Mori, Y. Ishida, M. Nagumo, 'Deformation microstructures of a low carbon steel characterized by tritium autoradiography and thermal desorption spectroscopy', *Journal of the Japan Institute of Metals-Nihon Kinzoku Gakkaishi*, Vol. 58 (1994), pp. 1141-1148
- [33] H. G. Lee, J. Y. Lee, 'Hydrogen trapping by TiC particles in iron', *Acta Metallurgica*, Vol. 32 (1984), issue 1, pp. 131-136
- [34] S. M. Lee, J. Y. Lee, 'The effect of the interface character of TiC particles on hydrogen trapping in steel', *Acta Metallurgica*. Vol. 35 (1987) pp.2695-2700
- [35] Z. Zhang, K.L. Moore, G. McMahon, R. Morana, M. Preuss, 'On the role of precipitates in hydrogen trapping and hydrogen embrittlement of a nickel-based superalloy', *Corrosion Science*, Vol. 146 (2019), pp. 58-69
- [36] J. Ovejero-García 'Hydrogen microprint technique in the study of hydrogen in steels' *Journal of Materials Science*, Vol. 20 (1985), issue 7, pp. 2623–2629
- [37] M. A. Mohtadi-Bonab, J. A. Szpunar, S. S. Razavi-Tousi 'A comparative study of hydrogen induced cracking behavior in API 5L X60 and X70 pipeline steels', *Engineering Failure Analysis*, Vol. 33 (2013), pp. 163-175
- [38] S. Wang, M. L. Martin, P. Sofronis, S. Ohnuki, N. Hashimoto, I. M. Robertson 'Hydrogen-induced intergranular failure of iron', *Acta Materialia*, Vol. 69 (2014), pp. 275-282
- [39] X. Y. Liu, J. Kameda, J. W. Anderegg, S. Takaki, K. Abiko, C. J. McMahon 'Hydrogen-induced cracking in a very-high-purity high-strength steel', *Materials Science and Engineering: A*, Vol. 492 (2008), pp. 218-220
- [40] Y. Bai, Y. Momotani, M. C. Chen, A. Shibata, N. Tsuji, 'Effect of grain refinement on hydrogen embrittlement behaviors of high-Mn TWIP steel', *Materials Science and Engineering: A*, Vol. 651 (2016), pp. 935-944
- [41] K. Takasawa, R. Ikeda, N. Ishikawa, R. Ishigaki, 'Effects of grain size and dislocation density on the susceptibility to high-pressure hydrogen environment embrittlement of high-strength low-alloy steels', *International Journal of Hydrogen Energy*, Vol. 37 (2012), pp. 2669-2675
- [42] 'Standard Test Methods for Determining Average Grain Size', ASTM E112 – 12
- [43] L. C. Chang, H. K. D. H. Bhadeshia, 'Austenite films in bainitic microstructures', *Metal Science Journal*, Vol. 11 (1995), issue 9, pp. 874-882

-
- [44] C. Garcia-Mateo, F. G. Caballero, H. K. D. H. Bhadeshia, 'Acceleration of Low-temperature Bainite', *ISIJ International*, Vol. 43 (2003), no. 11, pp. 1821–1825
- [45] C. Andreone, A. Murut, 'Influence of the austenite retained in the hydrogen embrittlement in AISI 4340', *Scripta Metallurgica et Materialia*, Vol. 24 (1990), issue 8, pp. 1453-1458
- [46] S. L. I. Chan, H. L. Lee, J. R. Yang, 'Effect of retained austenite on the hydrogen content and effective diffusivity of martensitic structure', *Metallurgical Transactions A*, Vol. 22 (1991), issue 11, pp. 2579–2586
- [47] L. Fielding, E. J. Song, D. Han, H. K. D. H. Bhadeshia, D. Suh, 'Hydrogen diffusion and the percolation of austenite in nanostructured bainitic steel', *Proceedings of The Royal Society A Mathematical Physical and Engineering Sciences*, Vol. 470 (2014), pp. 2168
- [48] M. L. Holzworth, 'Hydrogen Embrittlement of Type 304L Stainless Steel', *CORROSION*, Vol. 25 (1969), pp.107-115
- [49] M. Hatano, M. Fujinami, K. Arai, H. Fujii, M. Nagumo, 'Hydrogen embrittlement of austenitic stainless steels revealed by deformation microstructures and strain-induced creation of vacancies', *Acta Materialia*, Vol. 67 (2014), pp. 342–353
- [50] G. B. Olson, M. Cohen, 'A general mechanism of martensitic nucleation: Part III. Kinetics of martensitic nucleation' *Metallurgical Transactions A*, Vol.7 (1976), issue 12, pp 1915–1923
- [51] J. H. Ryu, D.I. Kim, H.S. Kim, H.K.D.H. Bhadeshia, D.W. Suh, 'Strain partitioning and mechanical stability of retained austenite', *Scripta Materialia*, Vol.63 (2010) pp. 297–299
- [52] J. H. Ryu, Y. S. Chun, C. S. Lee, H. K. D. H. Bhadeshia, D.W. Suh, 'Effect of Deformation on Hydrogen Trapping and Effusion in TRIP-Assisted Steel', *Acta Materialia*, Vol. 60 (2012), issue 10, pp. 4085-4092
- [53] H.K.D.H. Bhadeshia, R. Honeycombe, 'Steels: Microstructure and Properties', fourth edition, Elsevier Ltd (2017), pp. 160
- [54] J. M. Rigsbee, 'TEM observations on hydrogen-induced ϵ -HCP martensite', *Metallography*, Vol. 11 (1978), issue 4, pp 493-498
- [55] Y. Katz, H. Mathias, S. Nadiv, 'The mechanical stability of Austenite in maraging steels', *Metallurgical Transactions A*, Vol. 14 (1983), issue 4, pp. 801–808
- [56] P. Rozenak, R. Bergman, 'X-ray phase analysis of martensitic transformations in austenitic stainless steels electrochemically charged with hydrogen', *Materials Science and Engineering A*, Vol. 437 (2006), pp. 366–378
- [57] A. Szummer, A. Janko, 'Hydride Phases in Austenitic Stainless Steels', *CORROSION*, Vol. 35 (1979), pp. 461-464
- [58] K. Kamachi, M. Toge, T. Nakanori, 'X-Ray Study of Hydrides in Austenitic Stainless Steels', *Journal of the Society of Materials Science Japan*, Vol.26 (1977) issue 283 pp. 322-328
- [59] N. Narita, C. J. Altstetter, H. K. Birnbaum, 'Hydrogen-related phase transformations in austenitic stainless steels', *Metallurgical Transactions*, Vol. 13 (1982), issue 8, pp. 1355–1365
- [60] M. B. Whiteman, A. R. Troiano, 'The Influence of Hydrogen on the Stacking Fault Energy of an Austenitic Stainless Steel', *Physica Status Solidi (b)*, Vol. 7 (1964), issue2 , pp. K109-K110
- [61] P. A. Redhead, 'Thermal desorption of gases', *Vacuum*, Vol. 12 (1962), no. 4, pp. 203–211
- [62] H. E. Kissinger, 'Reaction Kinetics in Differential Thermal Analysis' *Analytical Chemistry*, Vol. 29 (1957), no.11, pp. 1702–1706
- [63] W. Y. Choo, J. Y. Lee, 'Thermal analysis of trapped hydrogen in pure iron' *Metallurgical Transactions A*, Vol. 13 (1982), issue 1, pp. 135–140
- [64] T. Tanaka, K. Kawakami, S. Hayashi, 'Visualization of deuterium flux and grain boundary diffusion in duplex stainless steel and Fe–30 % Ni alloy, using secondary ion mass spectrometry equipped with a Ga focused ion beam', *Journal of Materials Science*, Vol. 49 (2014), pp. 3928-3935
- [65] E. Zolotoyabko, 'Determination of the degree of preferred orientation within the March-Dollase approach', *Journal of Applied Crystallography*, Vol. 42 (2009), pp. 513-518

[66] A. F. Padilha, C. F. Tavares; M. A. Martorano, 'Delta Ferrite Formation in Austenitic Stainless Steel Castings' *Materials Science Forum*, Vol. 730-732 (2013), pp. 733-738

[67] <https://www.mathworks.com/matlabcentral/fileexchange/38088-diffusion-in-1d-and-2d> 2/24/2019

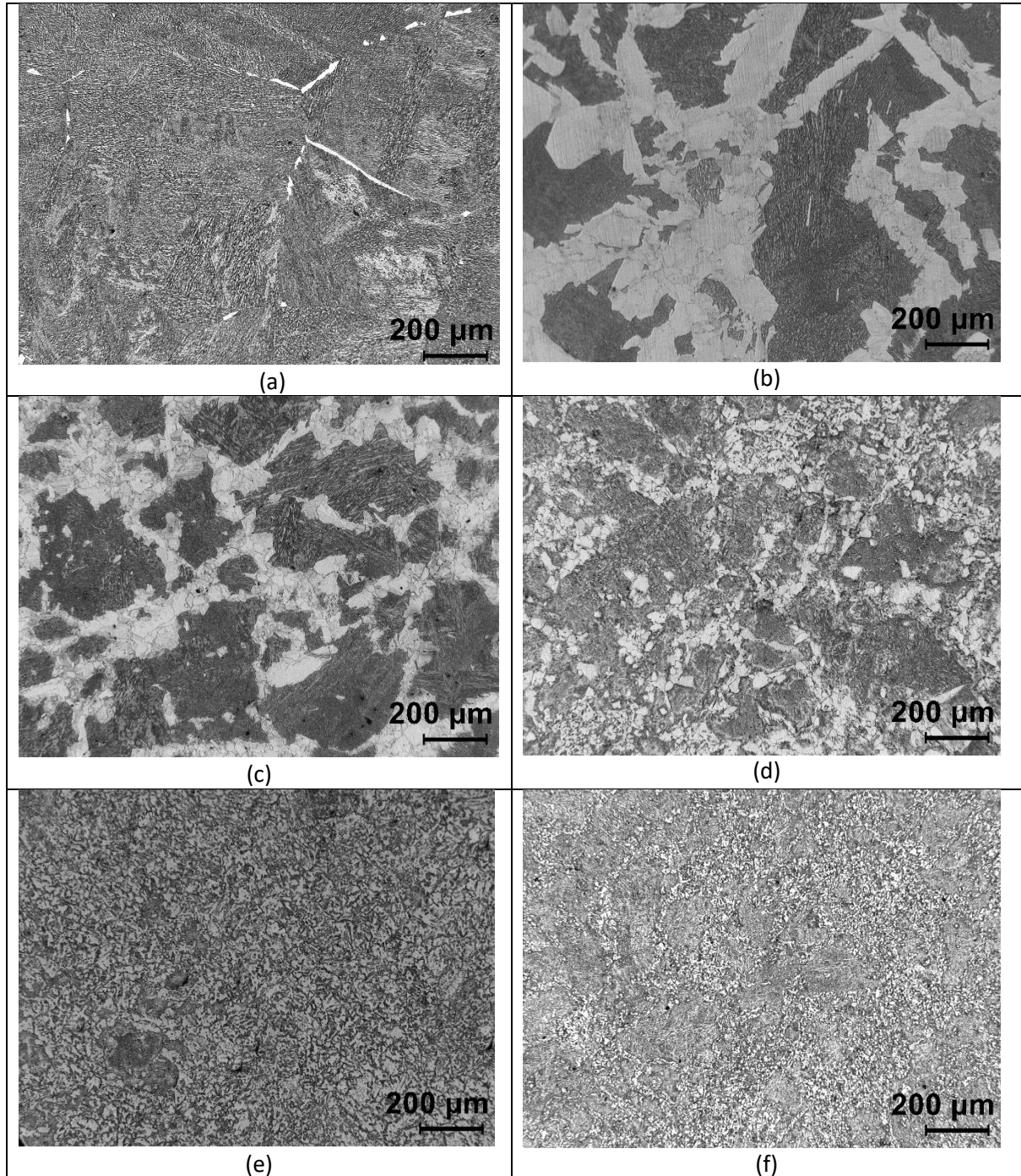
[68] J. A. Ronevich, J. G. Speer, G. Krauss, D. K. Matlock 'Improvement of the Hydrogen Microprint Technique on AHSS Steels' *Metallography, Microstructure, and Analysis*, Vol. 1 (2012) , issue 2, pp. 79–84

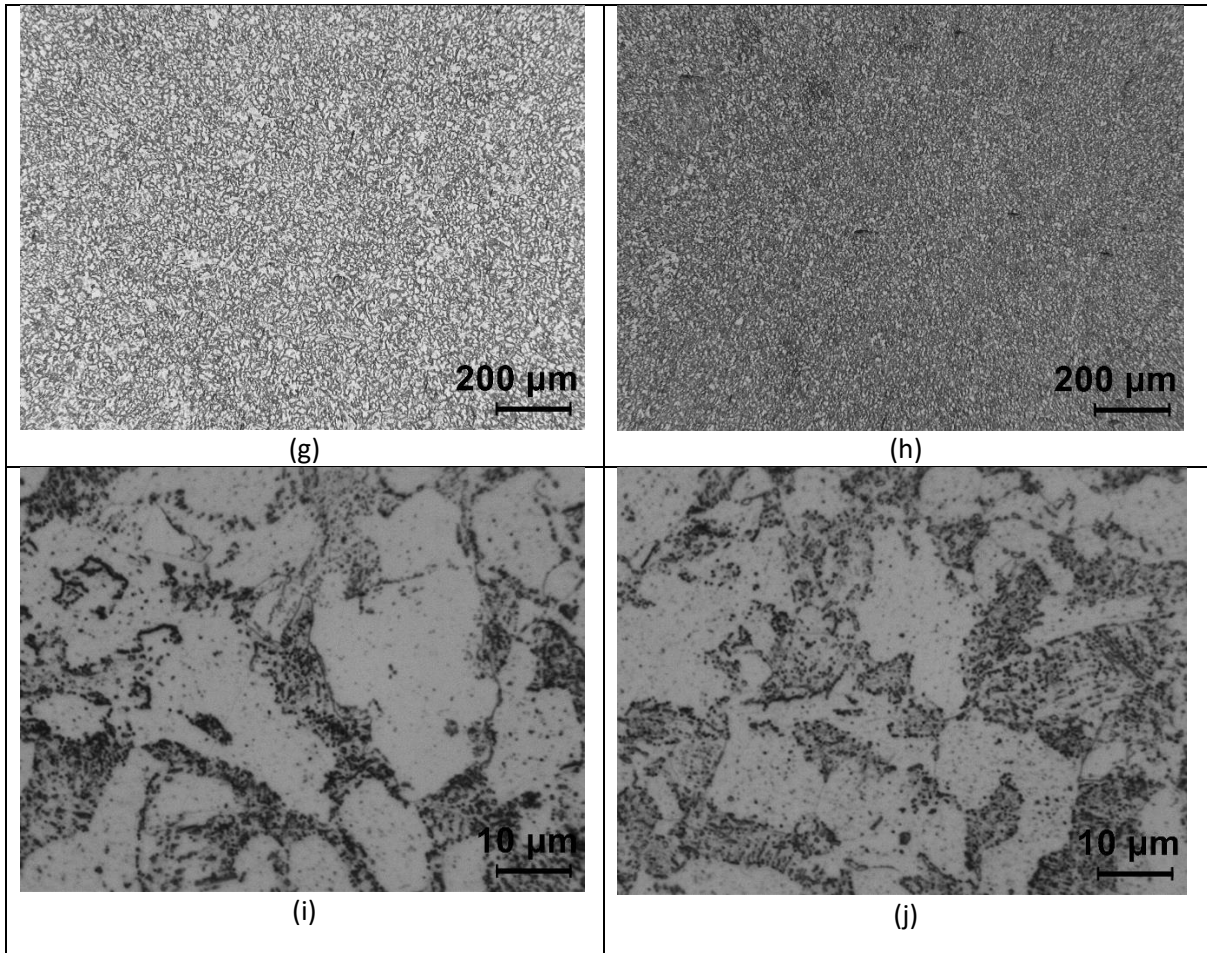
[69] K. Ichitani, M. Kanno, 'Visualization of hydrogen diffusion in steels by high sensitivity hydrogen microprint technique' *Science and Technology of Advanced Materials*, Vol. 4 (2003), pp. 545–551

[70] K. Horikawa, H. Okada, H. Kobayashi¹ and W. Urushihara, 'Visualization of Diffusive Hydrogen in Low Alloy Steel by means of Hydrogen Microprint Technique at Elevated Temperatures' *Materials Transactions*, Vol. 50 (2009), no. 4, pp. 759-764

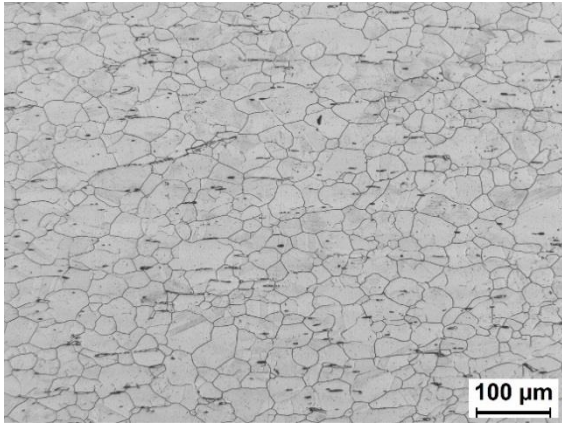
6. Appendix

6.1 Optical Images

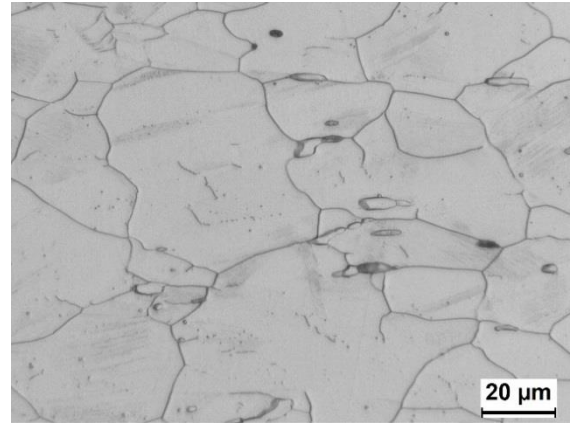




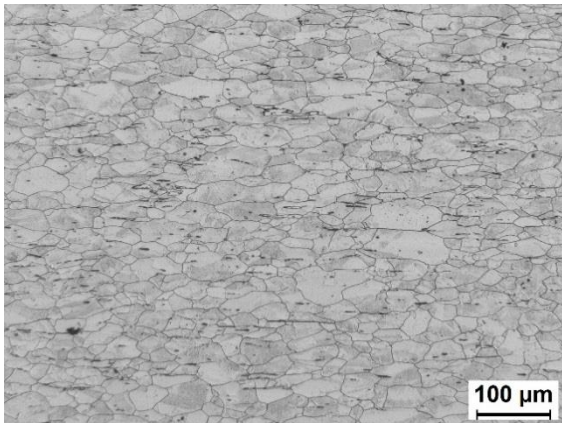
Appendix 6.1: Optical microscopic images showing the grain refinement progress. (a) air cooled from homogenization, (b)-(h): microstructure after 1st to 7th heat treatment cycle. Bainite can still be observed up till 5th cycles. After that, only ferrite/pearlite structure is left. ferrite grain size gradually reduced to 15-30 μm. (i) & (j): microstructures after 7th heat treatment cycle at higher magnification.



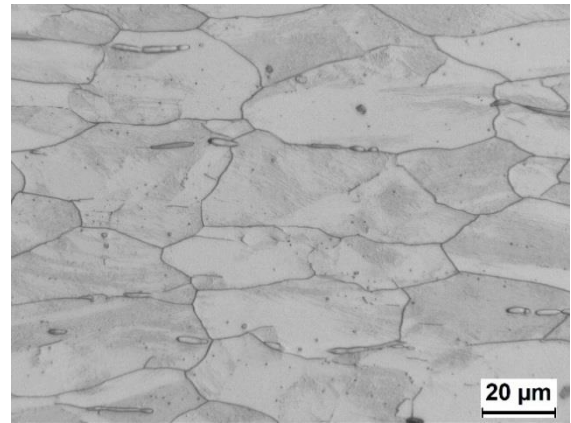
(a)



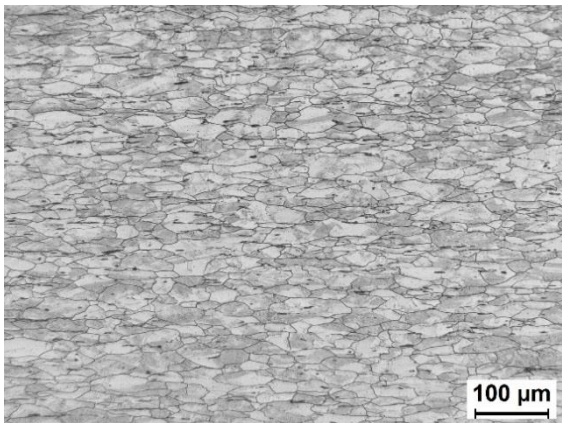
(b)



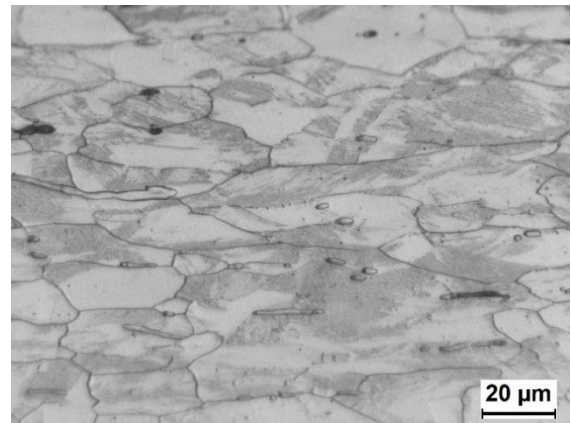
(c)



(d)

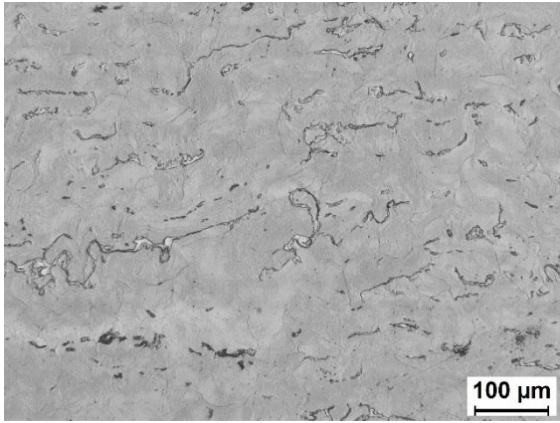


(e)

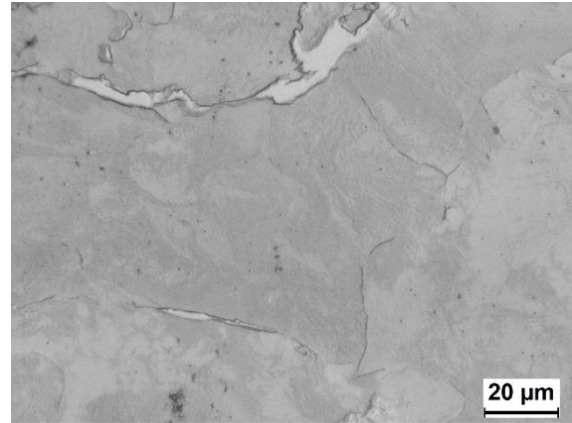


(f)

Appendix 6.2: The optical microstructure images of a compressed 8-mm-diameter austenitic steel specimen. (a) & (b): centre of the compressed specimen; (c) & (d): mid-way between bottom and centre of the compressed specimen; (e) & (f): bottom of the compressed specimen



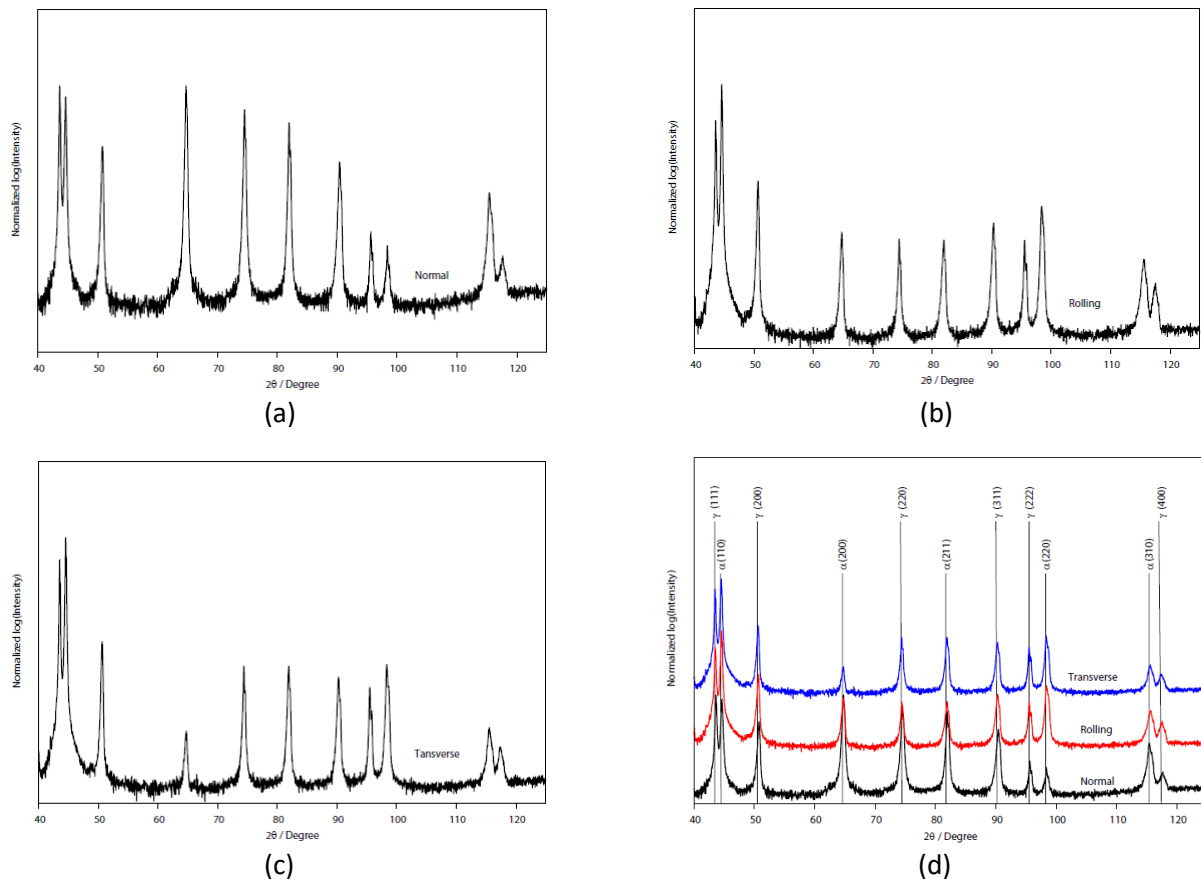
(a)



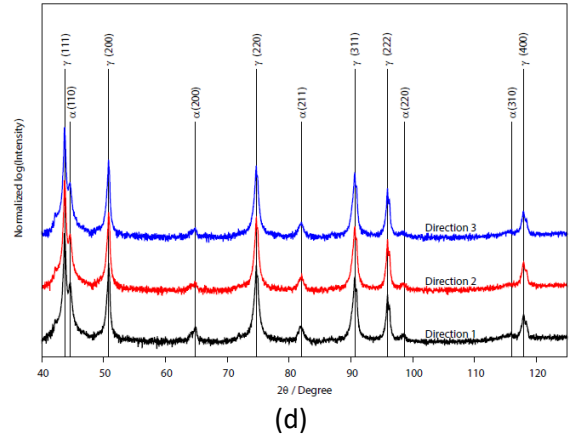
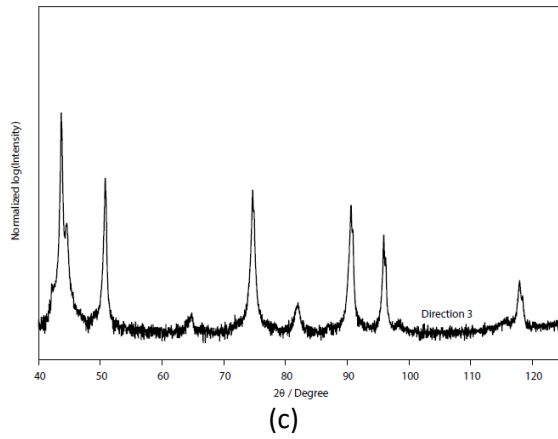
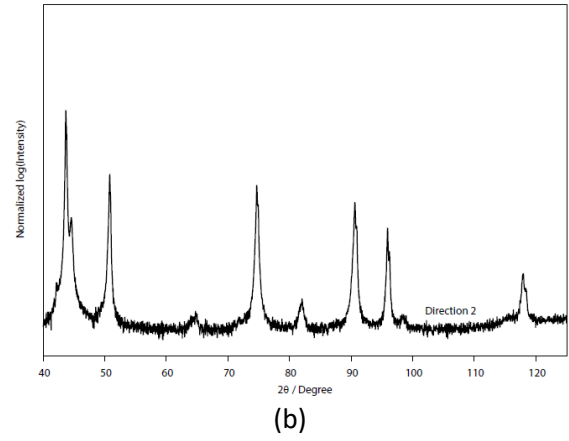
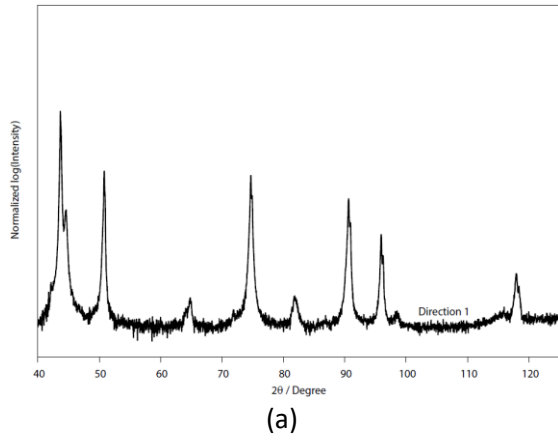
(b)

Appendix 6.3: *The optical microstructure images of a compressed 4-mm-diameter austenitic steel specimen at different magnifications, correspond to SEM images in figure 3.16*

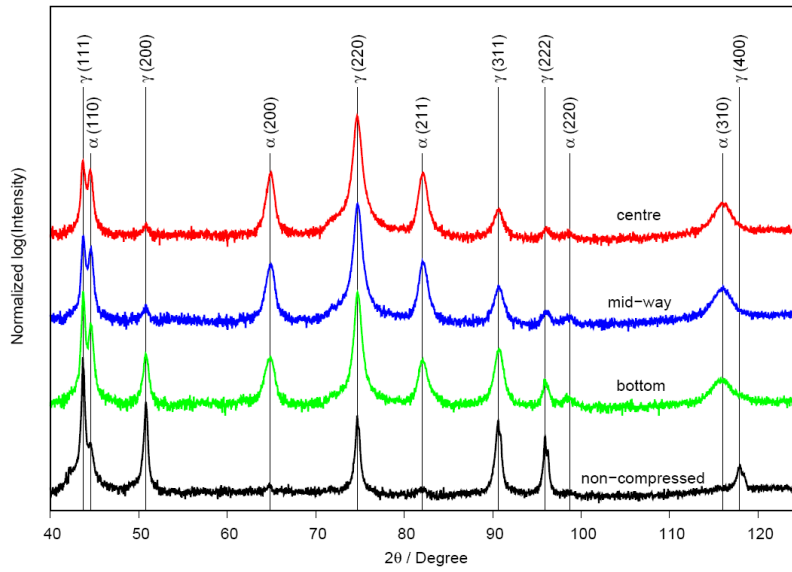
6.2 XRD plots



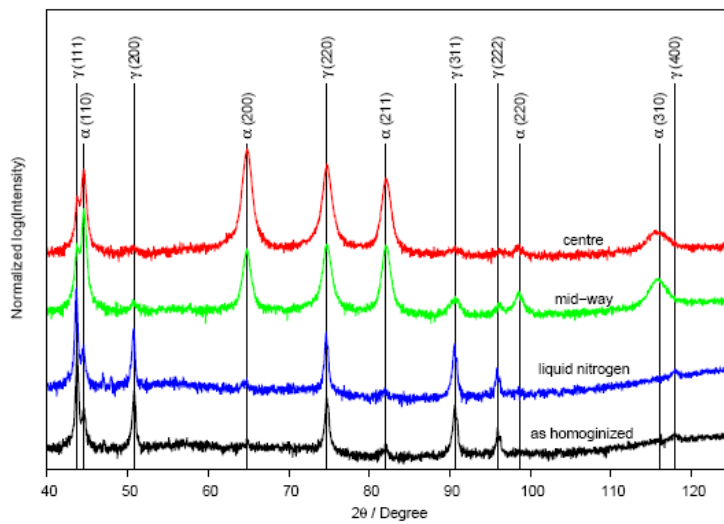
Appendix 6.4: Normalized logarithm plots of as-received duplex stainless steel from different directions: (a) normal direction; (b) rolling direction; (c) transverse direction, corresponding to figure 3.1 (a), (b), (c). (d): compiled plot of (a), (b) and (c)



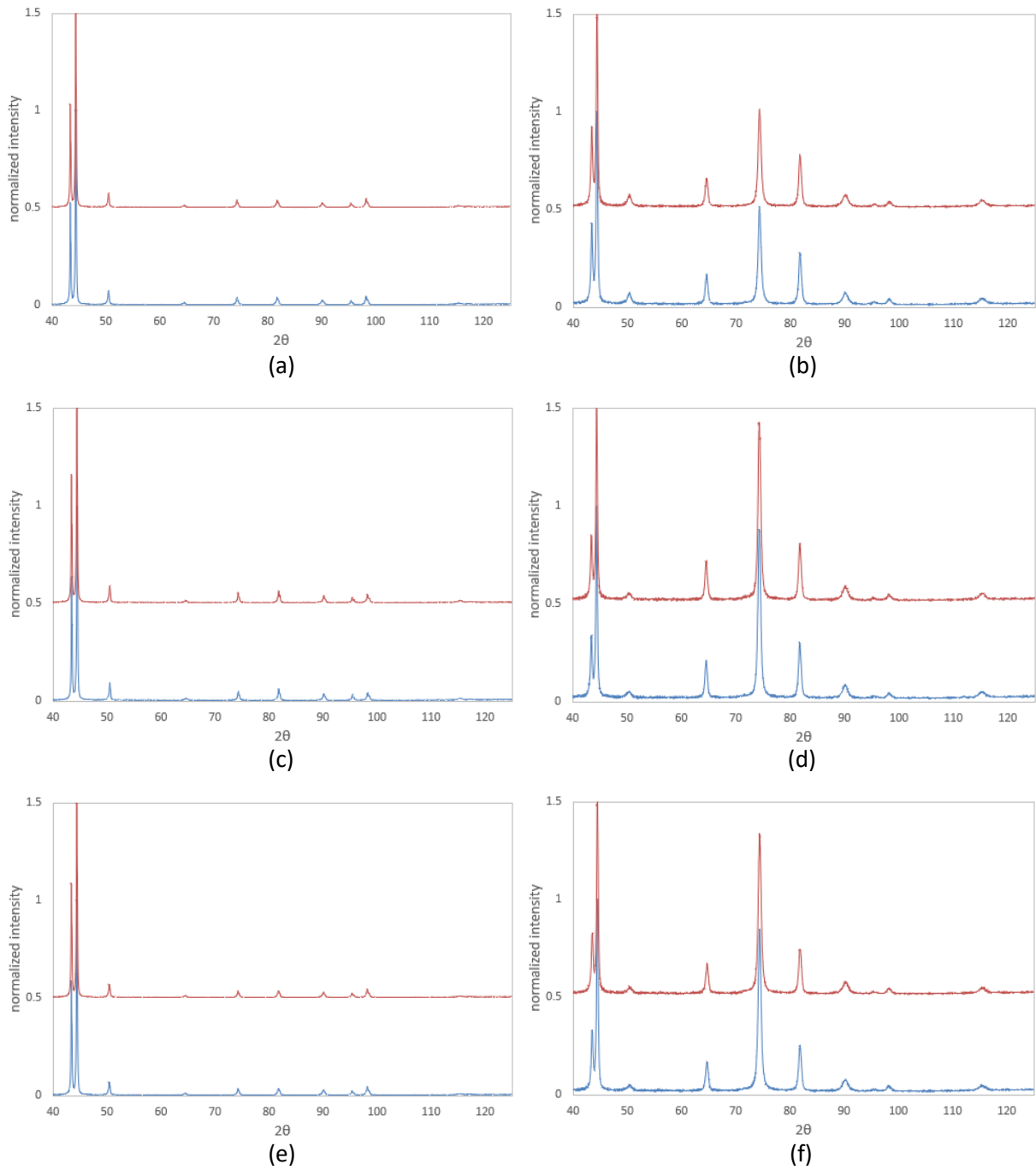
Appendix 6.5: Normalized logarithm plots of as-homogenized austenitic steel from different directions, (a) direction 1; (b) direction 2; (c) direction 3, corresponding to figure 3.4 (a), (b), (c). (d): compiled plot of (a), (b) and (c)



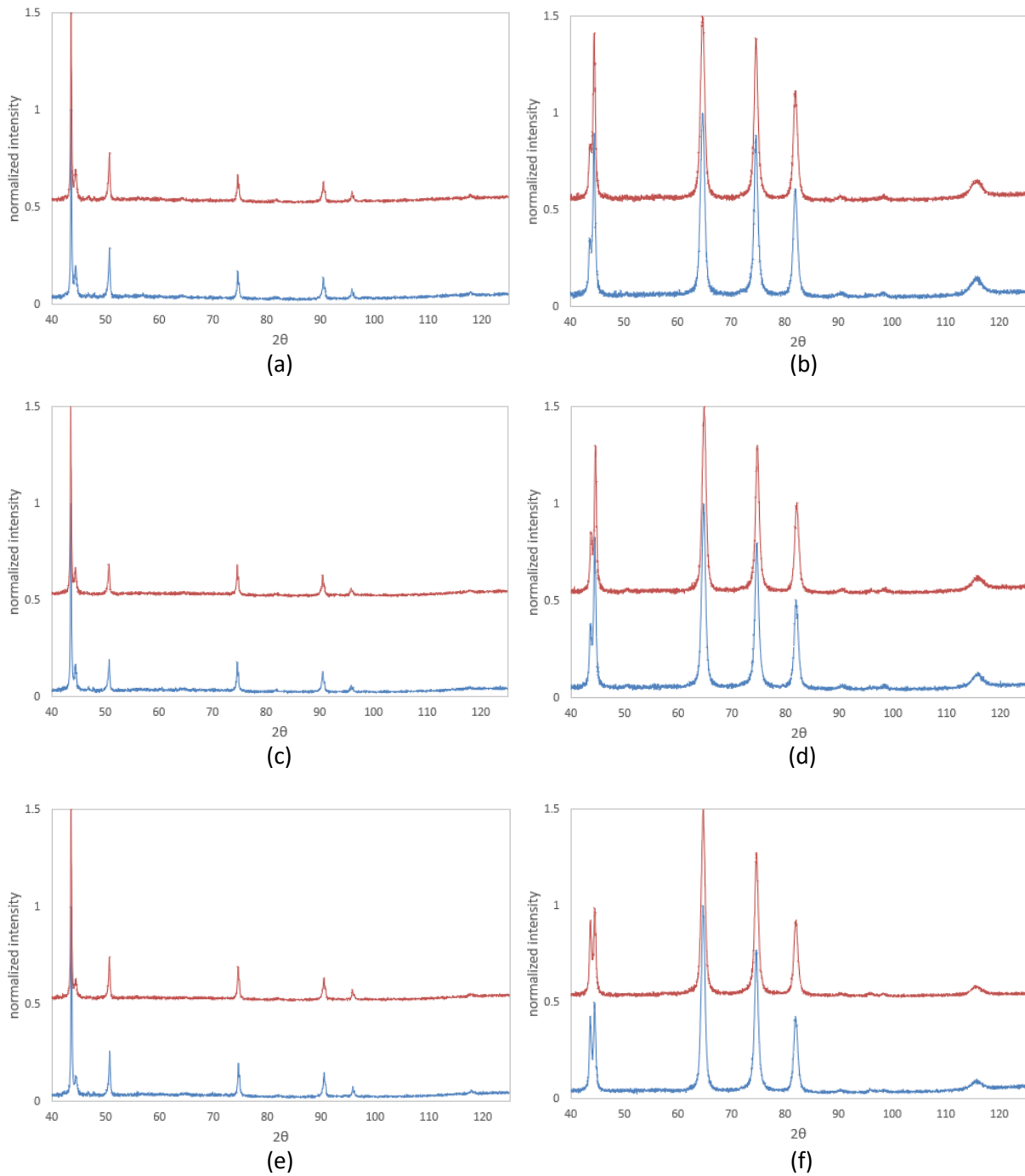
Appendix 6.6: Normalized logarithm plots of different sections of a compressed 8-mm-diameter austenitic steel specimen, corresponding to figure 3.17



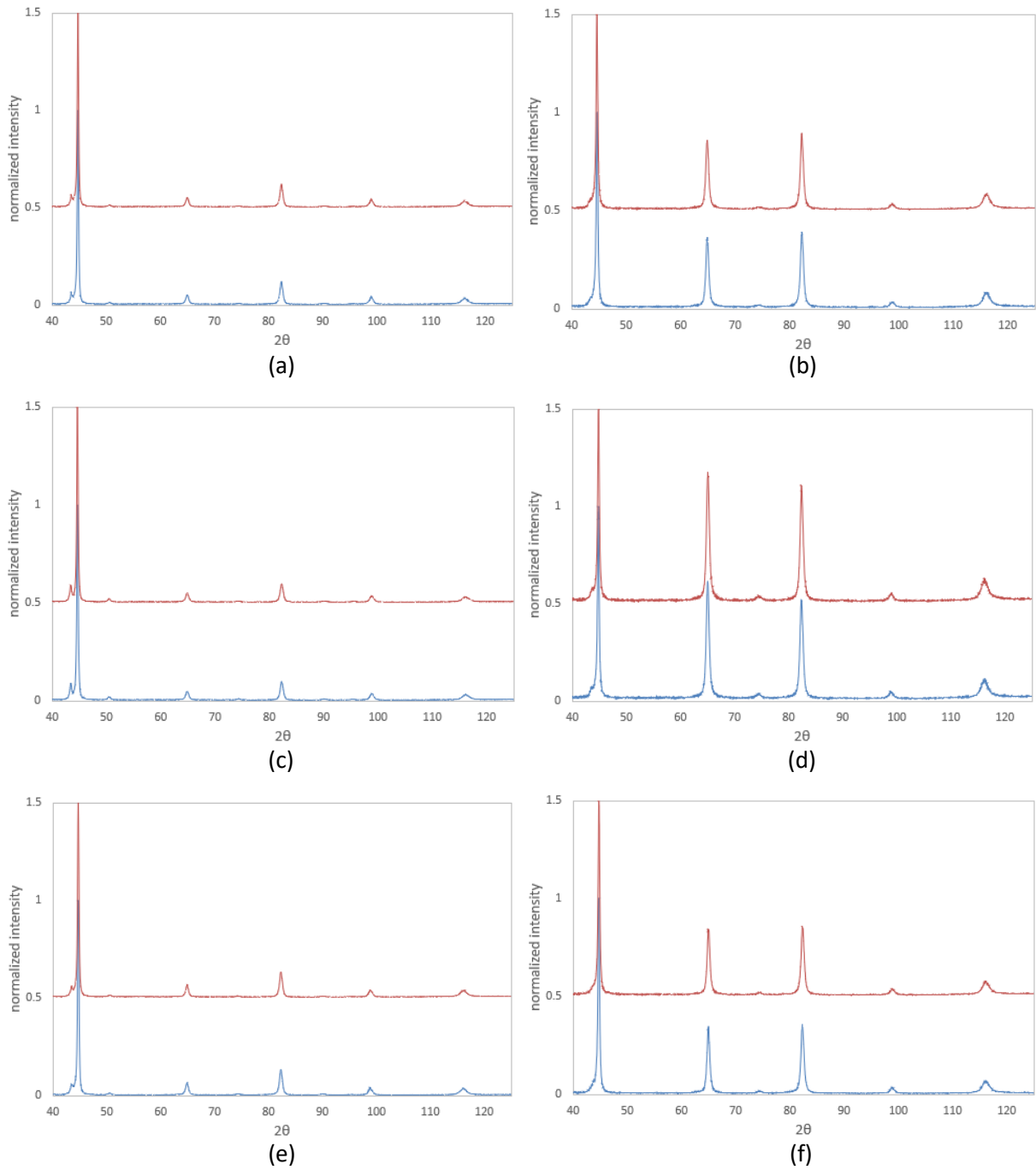
Appendix 6.7: Normalized logarithm plots of different sections of 4-mm-diameter austenitic specimens after compression or after quenching in liquid nitrogen, corresponding to figure 3.19



Appendix 6.8: Comparison of normalized XRD plots between aged (red) and non-aged (blue) duplex steel specimens charged for different amount of time (a)&(b): 4 days, (c)&(d): 10 days, (e)&(f): 16 days. (a),(c),(e) are non-compressed specimens, (b),(d),(f) are compressed specimens

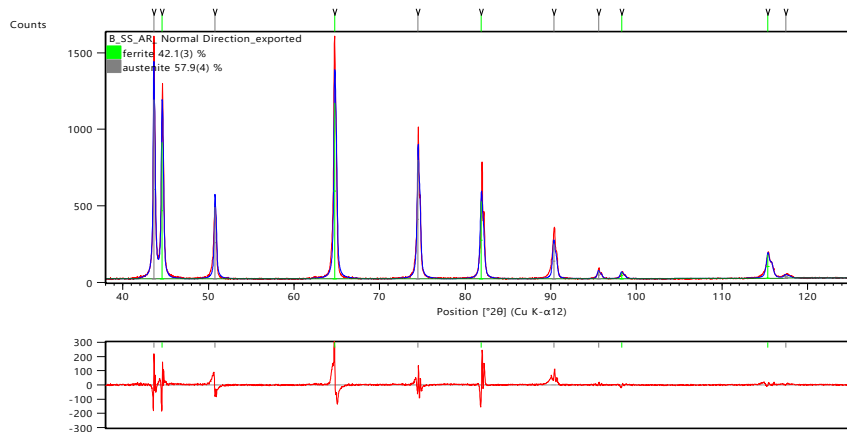


Appendix 6.9: Comparison of normalized XRD plots between aged (red) and non-aged (blue) austenitic steel specimens charged for different amount of time (a)&(b): 4 days, (c)&(d): 10 days, (e)&(f): 16 days. (a),(c),(e) are non-compressed specimens, (b),(d),(f) are compressed specimens



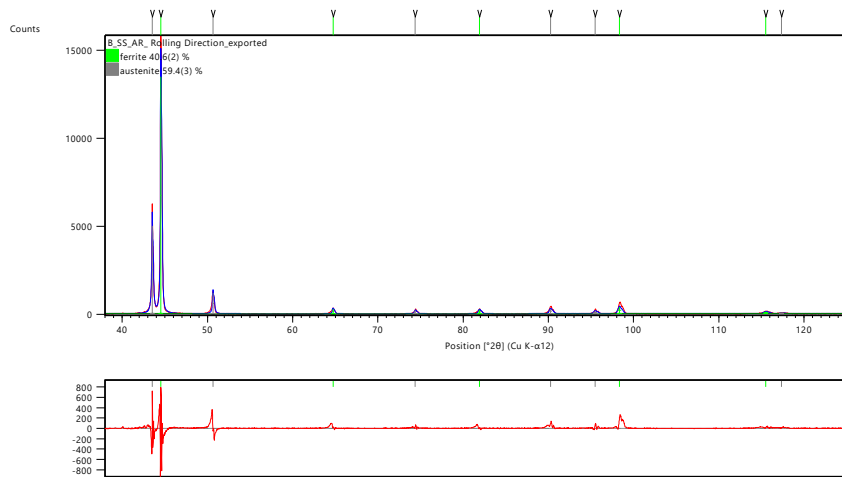
Appendix 6.10: Comparison of normalized XRD plots between aged (red) and non-aged (blue) bainitic steel specimens charged for different amount of time (a)&(b): 4 days, (c)&(d): 10 days, (e)&(f): 16 days. (a),(c),(e) are non-compressed specimens, (b),(d),(f) are compressed specimens

6.3 XRD fitting



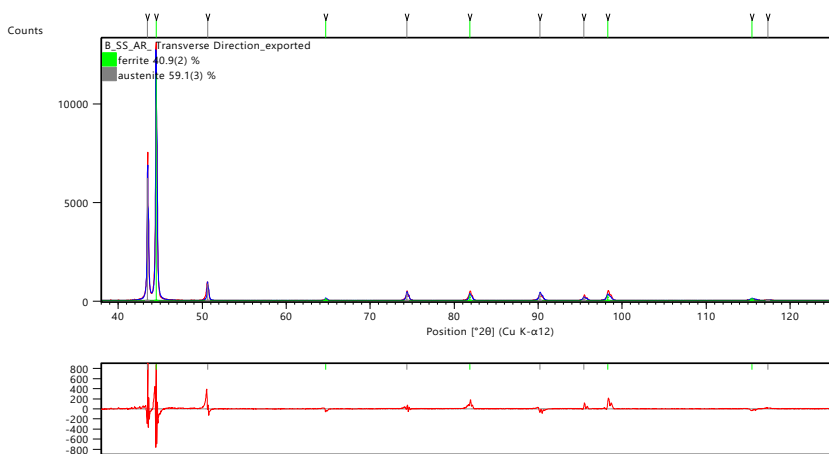
Agreement Indices	
R expected	12.79427
R profile	12.61924
Weighted R profile	16.52778
D-statistics	0.19821
Weighted D-statistics	0.2465
Goodness of Fit	1.29181
Mixture MAC [cm ² /g]	310.94
Custom Mixture MAC [cm ² /g]	-1

(a)



Agreement Indices	
R expected	9.38328
R profile	11.57434
Weighted R profile	16.29086
D-statistics	0.5803
Weighted D-statistics	0.18875
Goodness of Fit	1.73616
Mixture MAC [cm ² /g]	310.94
Custom Mixture M...	-1

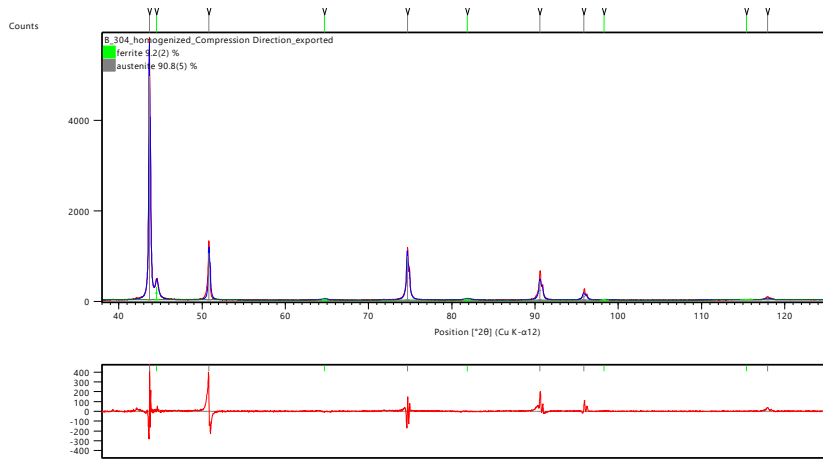
(b)



Agreement Indices	
R expected	9.66721
R profile	11.03691
Weighted R profile	15.40558
D-statistics	0.68858
Weighted D-statistics	0.22609
Goodness of Fit	1.59359
Mixture MAC [cm ² /g]	310.94
Custom Mixture MAC [cm ² /g]	-1

(c)

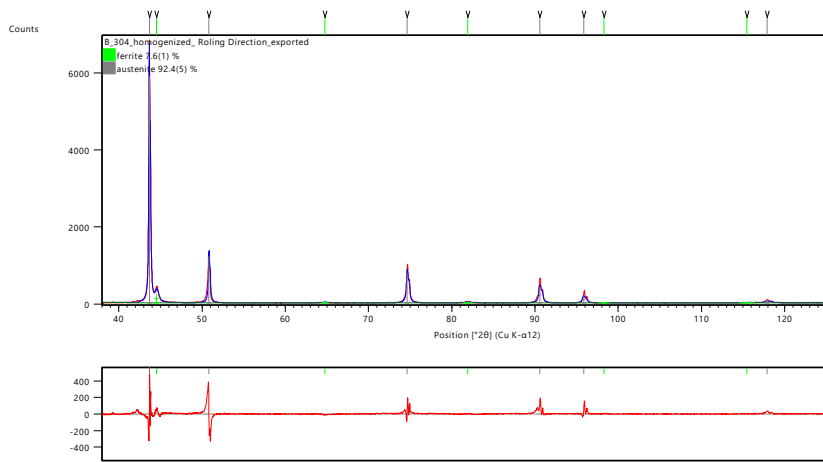
Appendix 6.11: XRD fitting using high-score Plus for Phase fraction analysis for different directions of the duplex steel (a) normal direction; (b) rolling direction; (c) transverse direction



Agreement Indices

R expected	11.71247
R profile	10.01942
Weighted R profile	14.87455
D-statistics	0.3321
Weighted D-statistics	0.26058
Goodness of Fit	1.26998
Mixture MAC [cm ² /g]	310.94
Custom Mixture MAC [cm ² /g]	-1

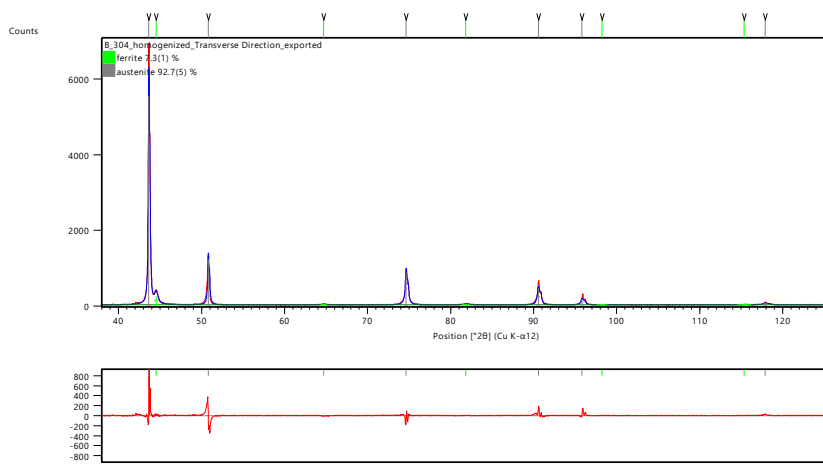
(a)



Agreement Indices

R expected	11.58646
R profile	11.74258
Weighted R profile	16.82335
D-statistics	0.32243
Weighted D-statistics	0.20369
Goodness of Fit	1.45198
Mixture MAC [cm ² /g]	310.94
Custom Mixture MAC [cm ² /g]	-1

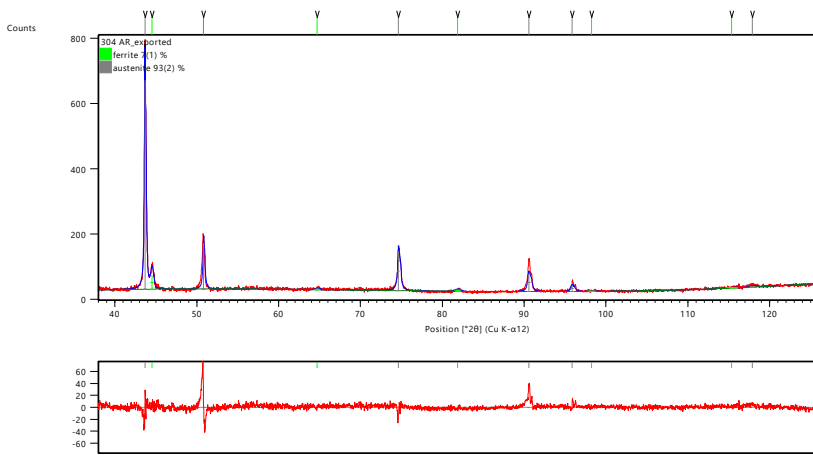
(b)



Agreement Indices

R expected	11.61552
R profile	10.76369
Weighted R profile	15.92682
D-statistics	0.3386
Weighted D-statistics	0.22797
Goodness of Fit	1.37117
Mixture MAC [cm ² /g]	310.94
Custom Mixture MAC [cm ² /g]	-1

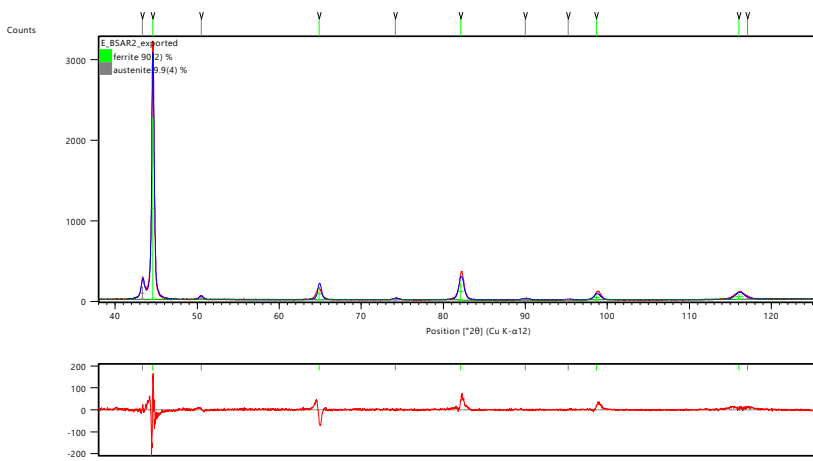
(c)



Agreement Indices	
R expected	16.72076
R profile	8.32588
Weighted R profile	11.23786
D-statistics	0.39786
Weighted D-statistics	0.65548
Goodness of Fit	0.67209
Mixture MAC [cm ² /g]	310.94
Custom Mixture MAC [cm ² /g]	-1

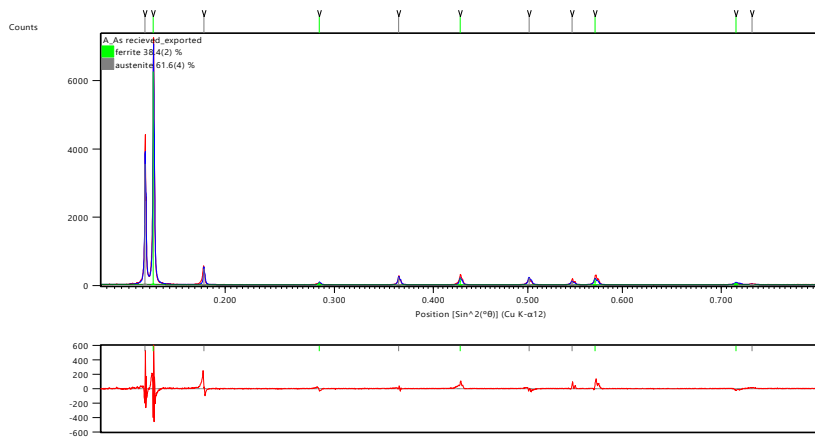
(d)

Appendix 6.12: XRD fitting using high-score Plus for Phase fraction analysis for different directions of the austenitic steel (a) direction 1; (b) direction 2; (c) direction 3; (c) direction 3 (smaller specimen)



Agreement Indices	
R expected	14.41843
R profile	9.53503
Weighted R profile	12.65194
D-statistics	0.22225
Weighted D-statistics	0.40414
Goodness of Fit	0.87748
Mixture MAC [cm ² /g]	310.94
Custom Mixture MAC [cm ² /g]	-1

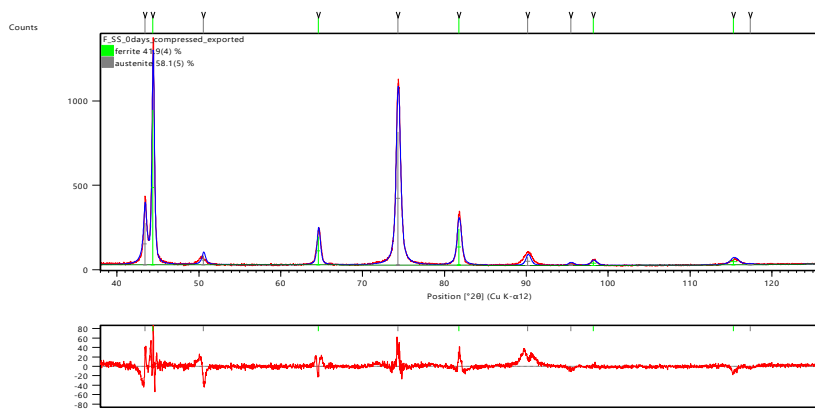
Appendix 6.13: XRD fitting using high-score Plus for Phase fraction analysis for the as-prepared bainitic steel



Agreement Indices

R expected	12.16503
R profile	11.63907
Weighted R profile	16.13911
D-statistics	0.72663
Weighted D-statistics	0.29509
Goodness of Fit	1.32668
Mixture MAC [cm ² /g]	310.94
Custom Mixture MAC [cm ² /g]	-1

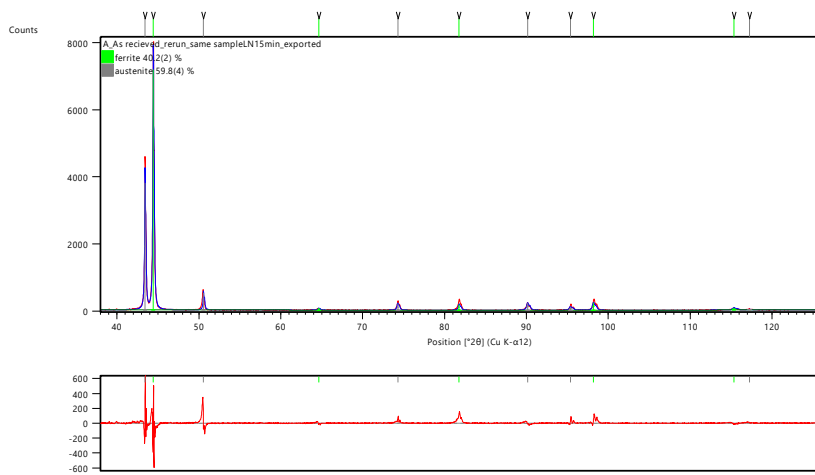
(a)



Agreement Indices

R expected	13.21413
R profile	7.61789
Weighted R profile	11.19608
D-statistics	0.3281
Weighted D-statistics	0.43181
Goodness of Fit	0.84728
Mixture MAC [cm ² /g]	310.94
Custom Mixture MAC [cm ² /g]	-1

(b)

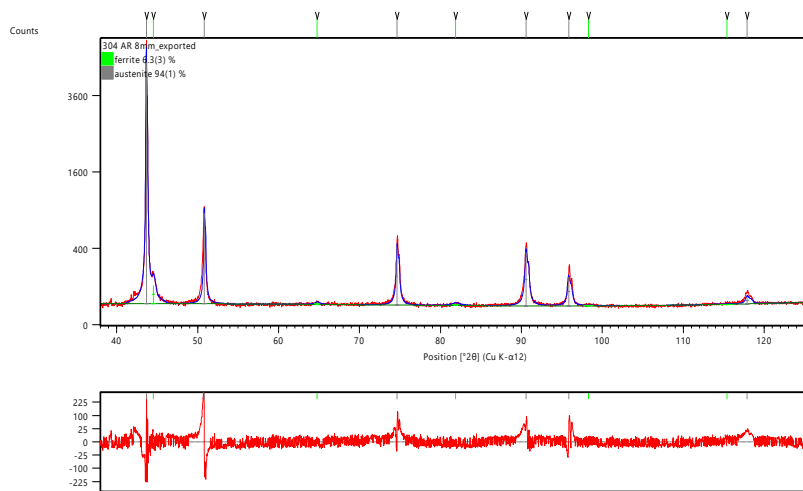


Agreement Indices

R expected	11.53846
R profile	10.6939
Weighted R profile	15.38999
D-statistics	0.66031
Weighted D-statistics	0.2766
Goodness of Fit	1.3338
Mixture MAC [cm ² /g]	310.94
Custom Mixture MAC [cm ² /g]	-1

(c)

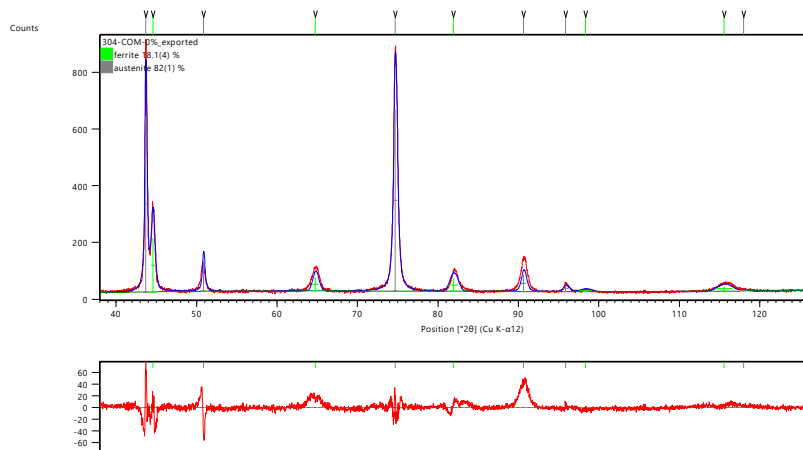
Appendix 6.14: XRD fitting using high-score Plus for Phase fraction analysis for the duplex steel (a) as-received; (b) after compression; (c) after dipping in liquid nitrogen



(a)

Agreement Indices

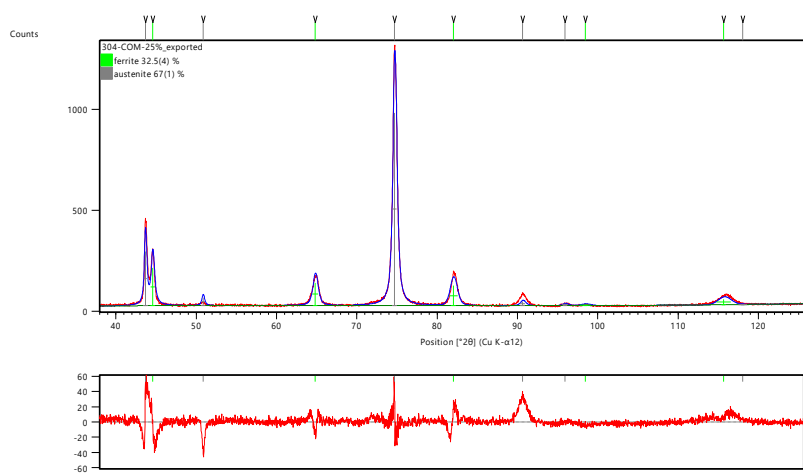
R expected	13.35127
R profile	10.41368
Weighted R profile	15.26729
D-statistics	0.33791
Weighted D-statistics	0.29287
Goodness of Fit	1.14351
Mixture MAC [cm ² /g]	310.94
Custom Mixture MAC [cm ² /g]	-1



(b)

Agreement Indices

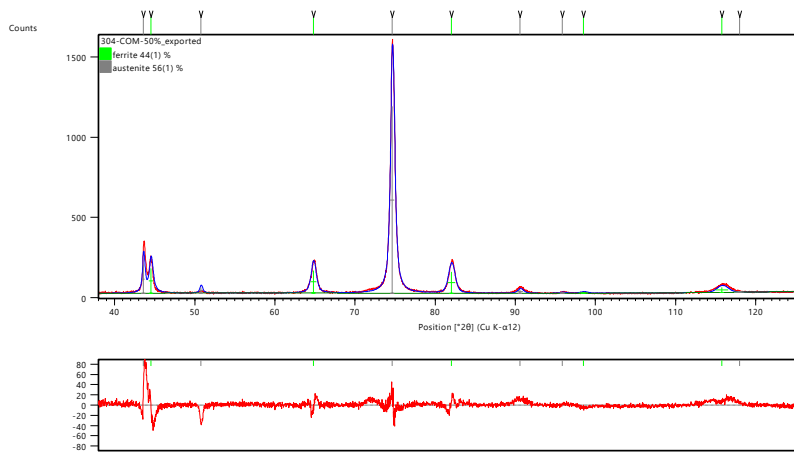
R expected	14.32361
R profile	9.46953
Weighted R profile	13.05155
D-statistics	0.21221
Weighted D-statistics	0.36045
Goodness of Fit	0.91119
Mixture MAC [cm ² /g]	310.94
Custom Mixture MAC [cm ² /g]	-1



(c)

Agreement Indices

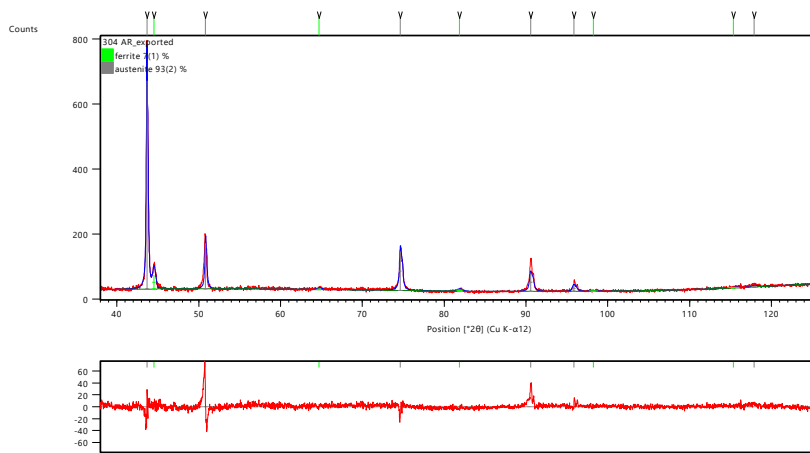
R expected	13.72683
R profile	8.40982
Weighted R profile	12.25483
D-statistics	0.25237
Weighted D-statistics	0.37793
Goodness of Fit	0.89276
Mixture MAC [cm ² /g]	310.94
Custom Mixture MAC [cm ² /g]	-1



(d)

Agreement Indices

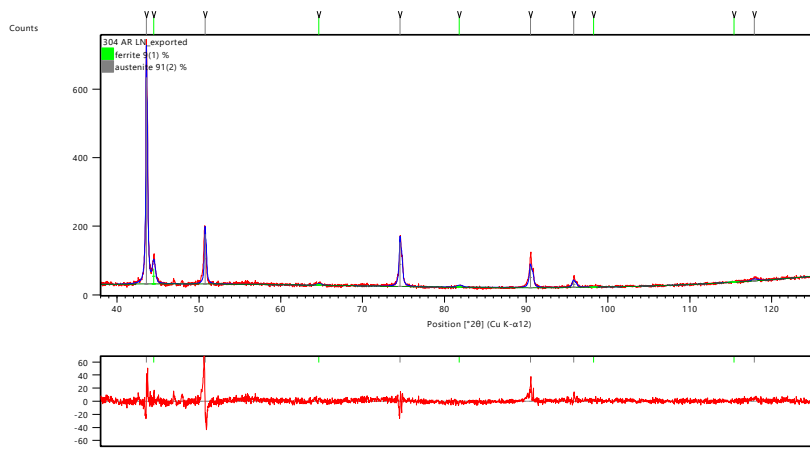
R expected	13.27328
R profile	7.7278
Weighted R profile	11.54167
D-statistics	0.24988
Weighted D-statistics	0.41588
Goodness of Fit	0.86954
Mixture MAC [cm ² /g]	310.94
Custom Mixture MAC [cm ² /g]	-1



(e)

Agreement Indices

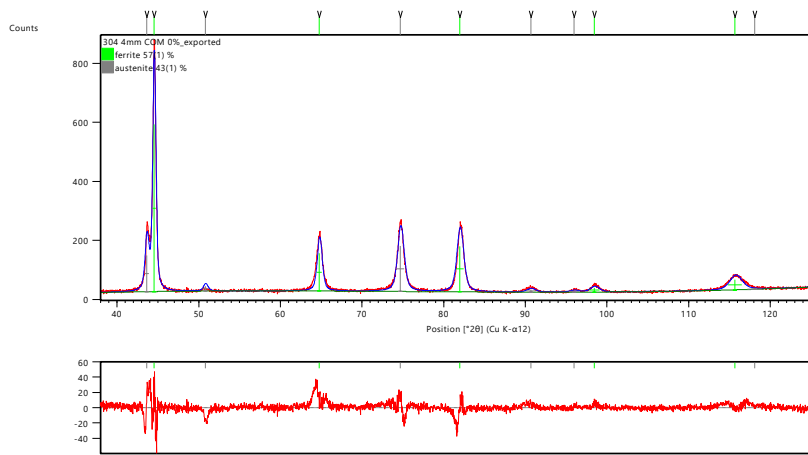
R expected	16.72076
R profile	8.32588
Weighted R profile	11.23786
D-statistics	0.39786
Weighted D-statistics	0.65548
Goodness of Fit	0.67209
Mixture MAC [cm ² /g]	310.94
Custom Mixture MAC [cm ² /g]	-1



(f)

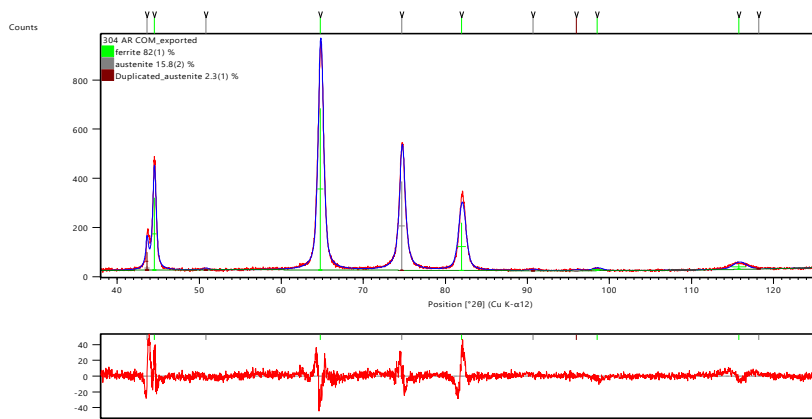
Agreement Indices

R expected	16.72883
R profile	7.77192
Weighted R profile	10.49756
D-statistics	0.45795
Weighted D-statistics	0.75348
Goodness of Fit	0.62751
Mixture MAC [cm ² /g]	310.94
Custom Mixture MAC [cm ² /g]	-1



Agreement Indices	
R expected	14.55601
R profile	7.51187
Weighted R profile	10.02351
D-statistics	0.41911
Weighted D-statistics	0.60957
Goodness of Fit	0.68862
Mixture MAC [cm ² /g]	310.94
Custom Mixture MAC [cm ² /g]	-1

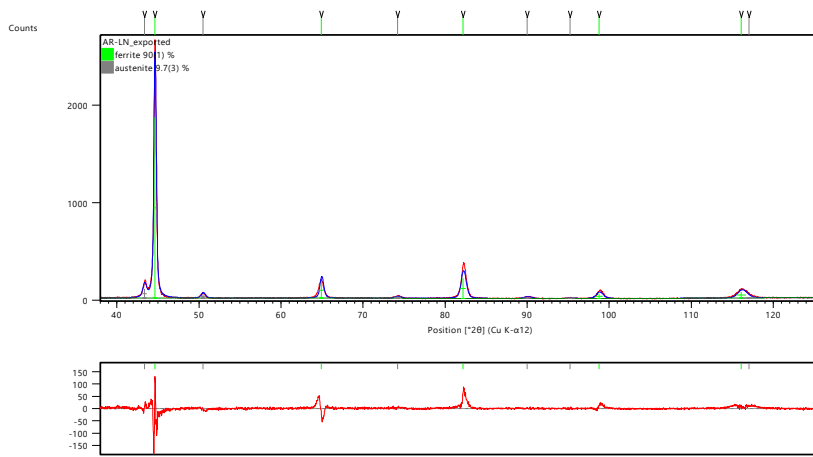
(g)



Agreement Indices	
R expected	13.27645
R profile	6.25684
Weighted R profile	8.39165
D-statistics	0.42774
Weighted D-statistics	0.77769
Goodness of Fit	0.63207
Mixture MAC [cm ² /g]	310.94
Custom Mixture MAC [cm ² /g]	-1

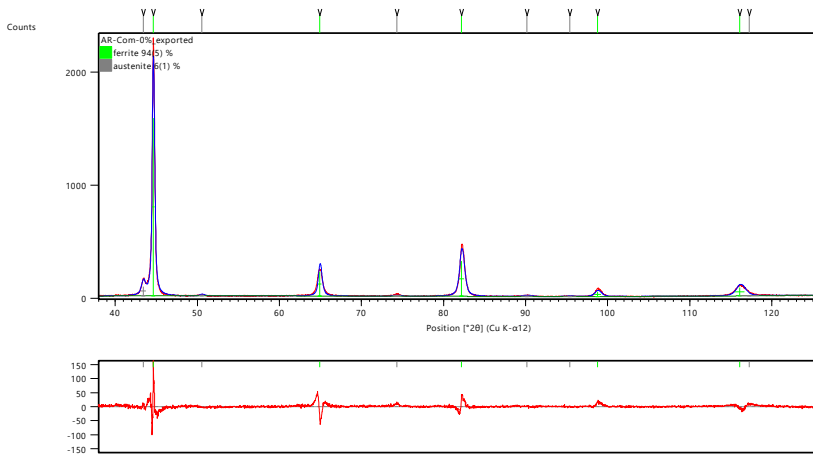
(h)

Appendix 6.15: XRD fitting using high-score Plus for Phase fraction analysis for 4-mm-diameter and 8-mm-diameter austenitic steel specimens after compression or after liquid nitrogen quenching, corresponding to table 3.2.2.1, (a) - (d) are for 8-mm-diameter specimens, (e) - (h) are for 4-mm-diameter specimens. (a) & (e): as homogenized; (b) & (g): bottom cross section after compression; (c): mid-way cross section after compression; (d) & (h): centre cross section after compression; (f): after 15-minute quenching in liquid nitrogen



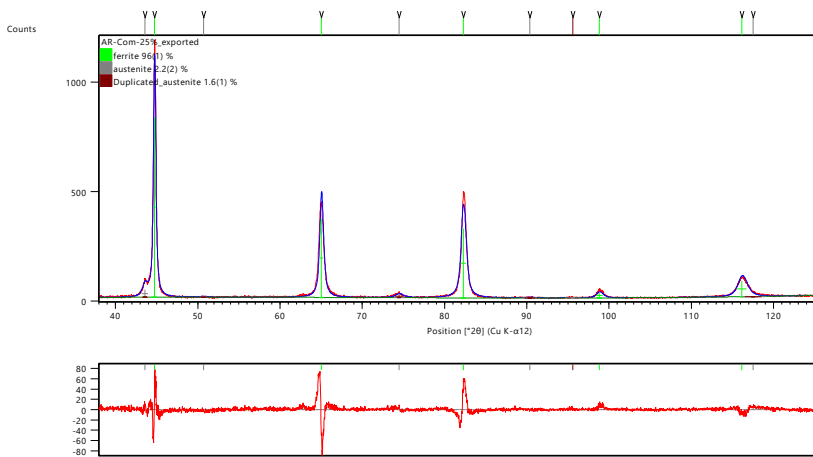
(a)

Agreement Indices	
R expected	15.1759
R profile	9.95319
Weighted R profile	12.81529
D-statistics	0.19666
Weighted D-statistics	0.44859
Goodness of Fit	0.84445
Mixture MAC [cm ² /g]	310.94
Custom Mixture MAC [cm ² /g]	-1



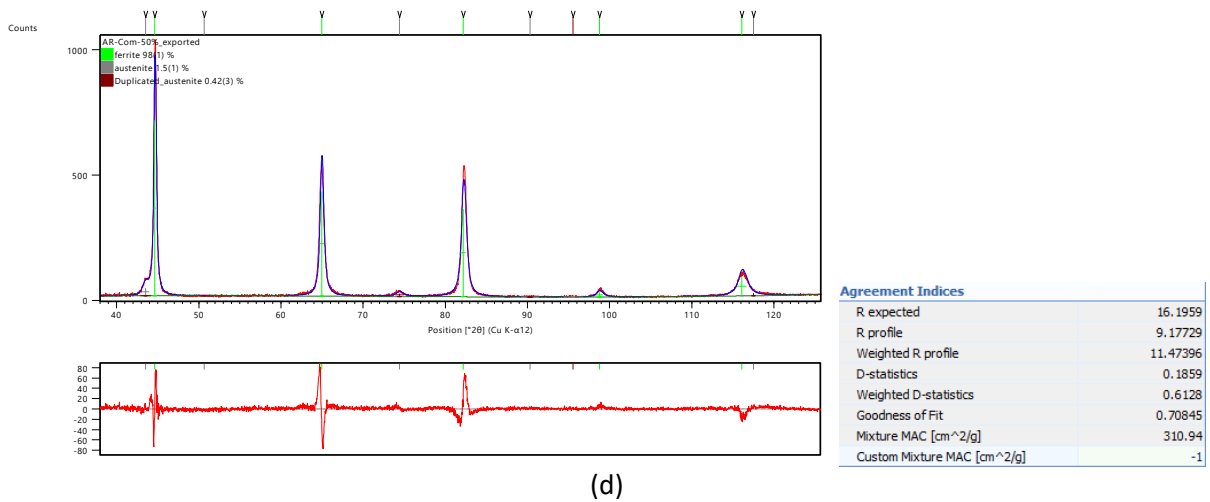
(b)

Agreement Indices	
R expected	15.25503
R profile	8.42818
Weighted R profile	11.09228
D-statistics	0.31193
Weighted D-statistics	0.56927
Goodness of Fit	0.72712
Mixture MAC [cm ² /g]	310.94
Custom Mixture MAC [cm ² /g]	-1

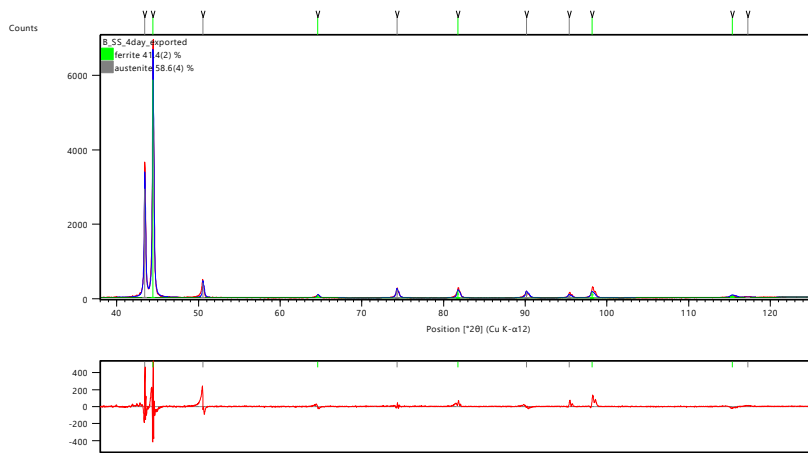


(c)

Agreement Indices	
R expected	16.44325
R profile	9.23367
Weighted R profile	11.54071
D-statistics	0.19762
Weighted D-statistics	0.61541
Goodness of Fit	0.70185
Mixture MAC [cm ² /g]	310.94
Custom Mixture MAC [cm ² /g]	-1

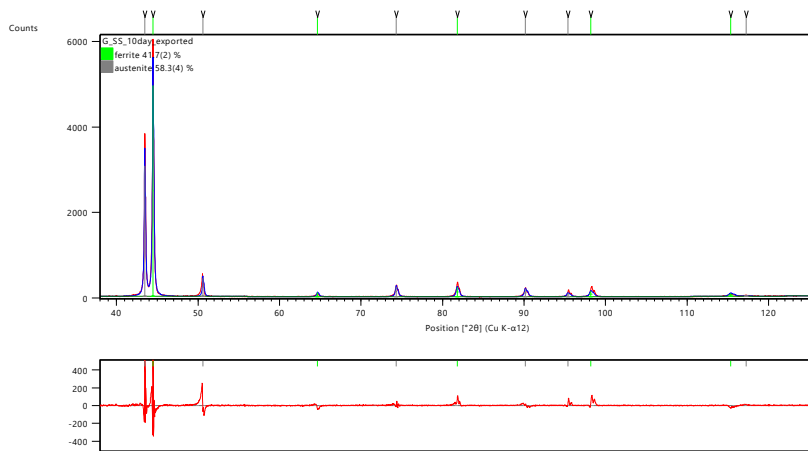


Appendix 6.16: XRD fitting using high-score Plus for Phase fraction analysis for the bainitic steel (a) after 15-minute quenching in liquid nitrogen; (b) bottom cross section after compression, (c) mid-way cross section after compression, (d) centre cross section after compression



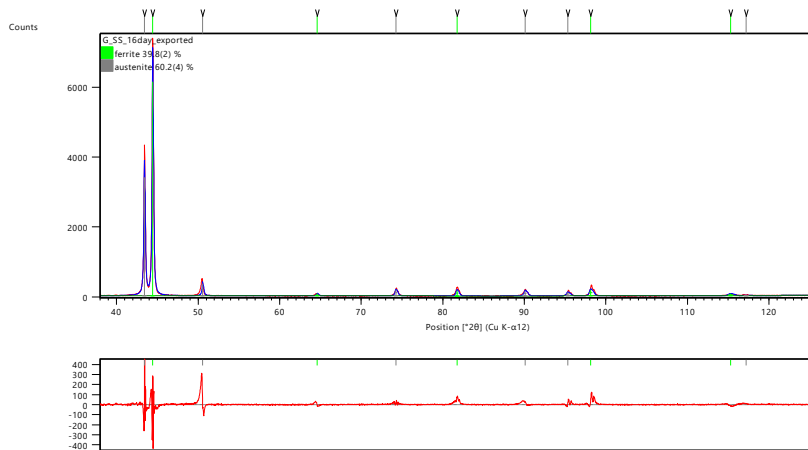
(a)

Agreement Indices	
R expected	11.78432
R profile	10.09777
Weighted R profile	14.47508
D-statistics	0.6464
Weighted D-statistics	0.28952
Goodness of Fit	1.22833
Mixture MAC [cm ² /g]	310.94
Custom Mixture MAC [cm ² /g]	-1



(b)

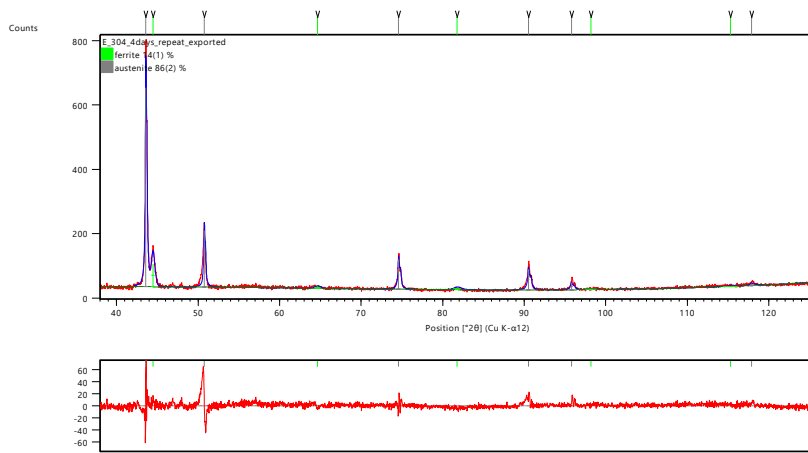
Agreement Indices	
R expected	11.72727
R profile	10.00703
Weighted R profile	14.42003
D-statistics	0.69294
Weighted D-statistics	0.29917
Goodness of Fit	1.22961
Mixture MAC [cm ² /g]	310.94
Custom Mixture MAC [cm ² /g]	-1



(c)

Agreement Indices	
R expected	11.21457
R profile	9.44956
Weighted R profile	14.36096
D-statistics	0.56674
Weighted D-statistics	0.25665
Goodness of Fit	1.28056
Mixture MAC [cm ² /g]	310.94
Custom Mixture MAC [cm ² /g]	-1

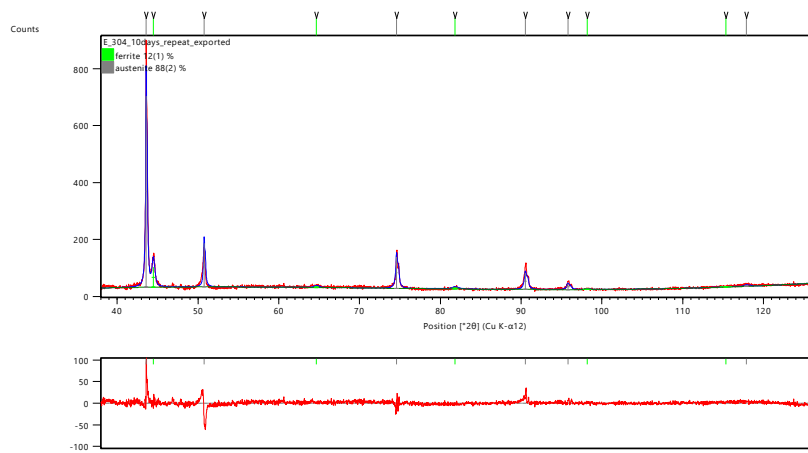
Appendix 6.17: XRD fitting using high-score Plus for Phase fraction analysis for duplex steel specimens charged for different amount of time (a) 4 days; (b) 10 days; (c) 16 days



Agreement Indices

R expected	16.18767
R profile	8.25304
Weighted R profile	11.04316
D-statistics	0.48873
Weighted D-statistics	0.67208
Goodness of Fit	0.6822
Mixture MAC [cm ² /g]	310.94
Custom Mixture MAC [cm ² /g]	-1

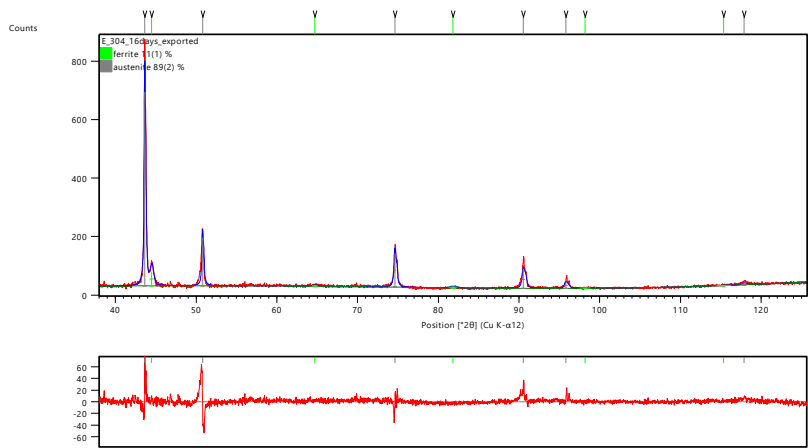
(a)



Agreement Indices

R expected	16.36288
R profile	8.55599
Weighted R profile	11.44777
D-statistics	0.40765
Weighted D-statistics	0.64738
Goodness of Fit	0.69962
Mixture MAC [cm ² /g]	310.94
Custom Mixture MAC [cm ² /g]	-1

(b)

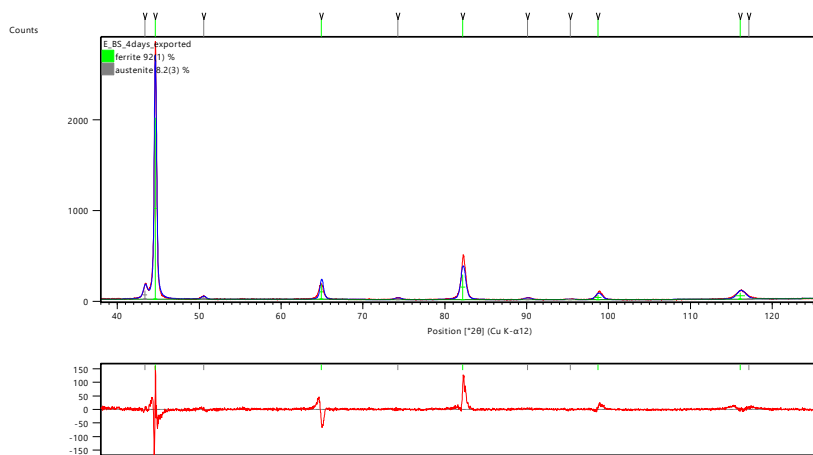


Agreement Indices

R expected	16.59368
R profile	8.67568
Weighted R profile	11.73073
D-statistics	0.3883
Weighted D-statistics	0.60669
Goodness of Fit	0.70694
Mixture MAC [cm ² /g]	310.94
Custom Mixture MAC [cm ² /g]	-1

(c)

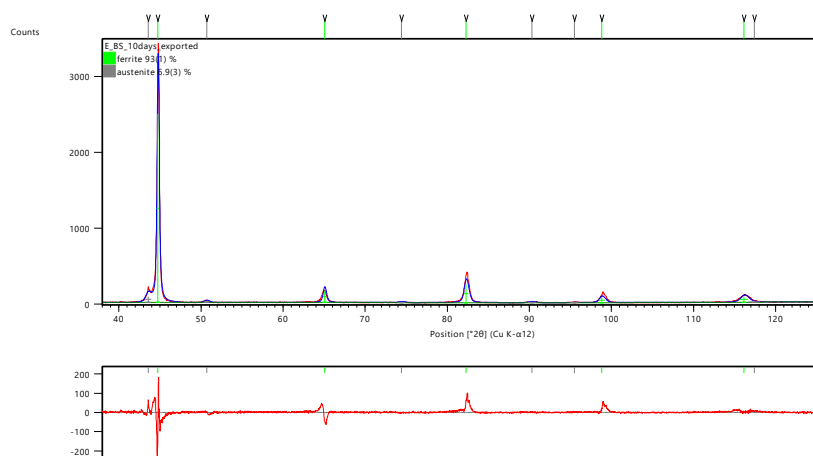
Appendix 6.18: XRD fitting using high-score Plus for Phase fraction analysis for austenitic steel specimens charged for different amount of time (a) 4 days; (b) 10 days; (c) 16 days



(a)

Agreement Indices

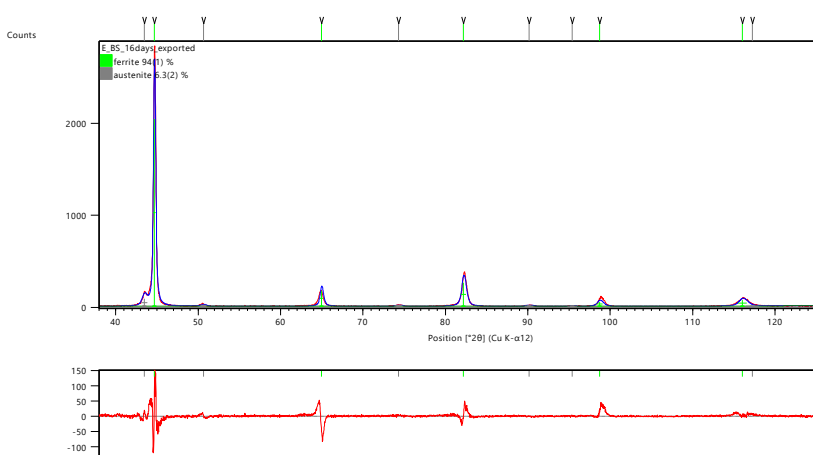
R expected	14.78822
R profile	9.28698
Weighted R profile	12.49199
D-statistics	0.17621
Weighted D-statistics	0.41076
Goodness of Fit	0.84473
Mixture MAC [cm ² /g]	310.94
Custom Mixture MAC [cm ² /g]	-1



(b)

Agreement Indices

R expected	14.67063
R profile	10.37119
Weighted R profile	13.85658
D-statistics	0.18556
Weighted D-statistics	0.35839
Goodness of Fit	0.94451
Mixture MAC [cm ² /g]	310.94
Custom Mixture MAC [cm ² /g]	-1

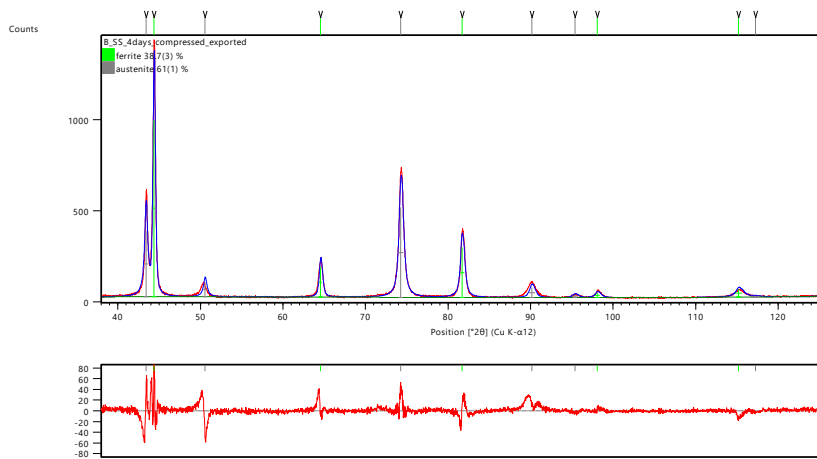


(c)

Agreement Indices

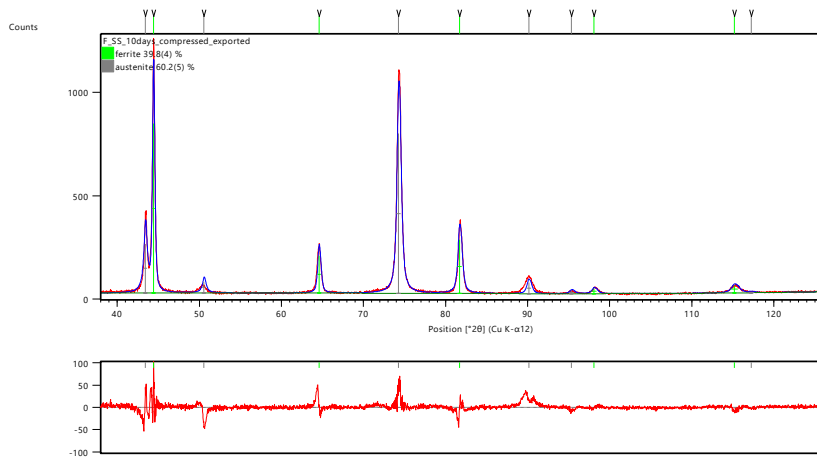
R expected	16.56088
R profile	10.62826
Weighted R profile	14.74254
D-statistics	0.19408
Weighted D-statistics	0.40094
Goodness of Fit	0.8902
Mixture MAC [cm ² /g]	310.94
Custom Mixture MAC [cm ² /g]	-1

Appendix 6.19: XRD fitting using high-score Plus for Phase fraction analysis for bainitic steel specimens charged for different amount of time (a) 4 days; (b) 10 days; (c) 16 days



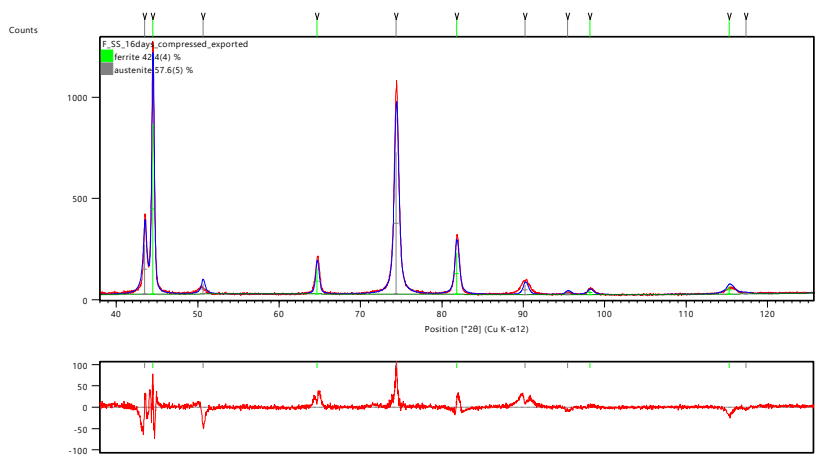
Agreement Indices	
R expected	13.64555
R profile	8.18123
Weighted R profile	11.75941
D-statistics	0.23681
Weighted D-statistics	0.39501
Goodness of Fit	0.86178
Mixture MAC [cm ² /g]	310.94
Custom Mixture MAC [cm ² /g]	-1

(a)



Agreement Indices	
R expected	13.34633
R profile	7.83292
Weighted R profile	11.4596
D-statistics	0.30045
Weighted D-statistics	0.41141
Goodness of Fit	0.85863
Mixture MAC [cm ² /g]	310.94
Custom Mixture MAC [cm ² /g]	-1

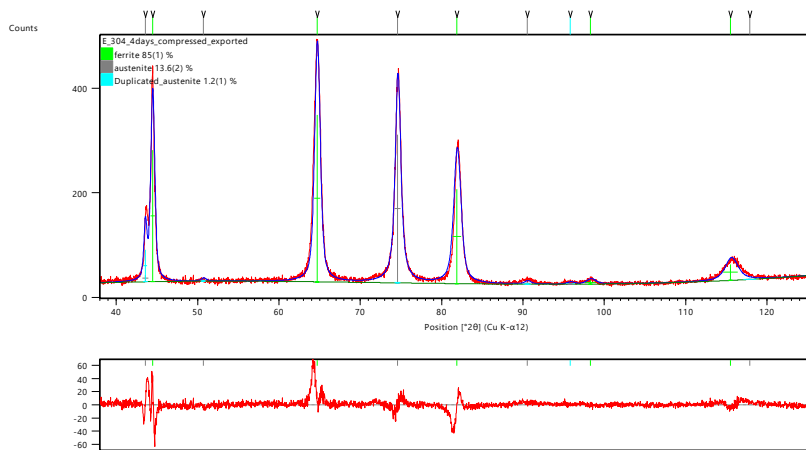
(b)



Agreement Indices	
R expected	13.40347
R profile	9.09308
Weighted R profile	12.81721
D-statistics	0.18765
Weighted D-statistics	0.31124
Goodness of Fit	0.95626
Mixture MAC [cm ² /g]	310.94
Custom Mixture MAC [cm ² /g]	-1

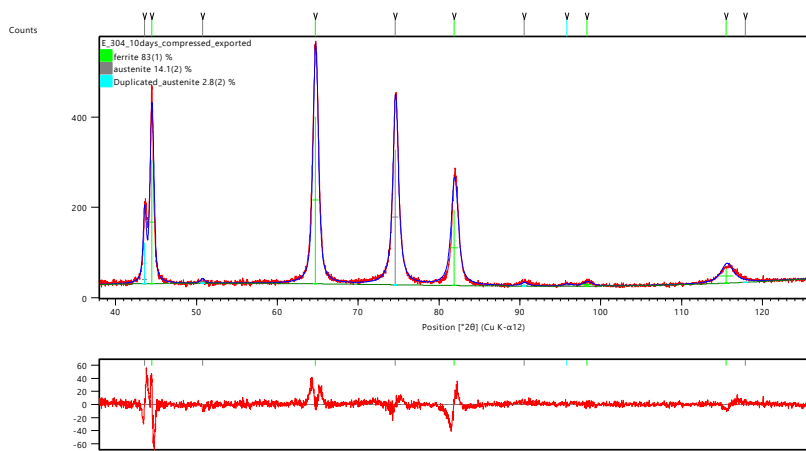
(c)

Appendix 6.20: XRD fitting using high-score Plus for Phase fraction analysis for duplex steel specimens charged for different amount of time then compressed (a) 4 days; (b) 10 days; (c) 16 days



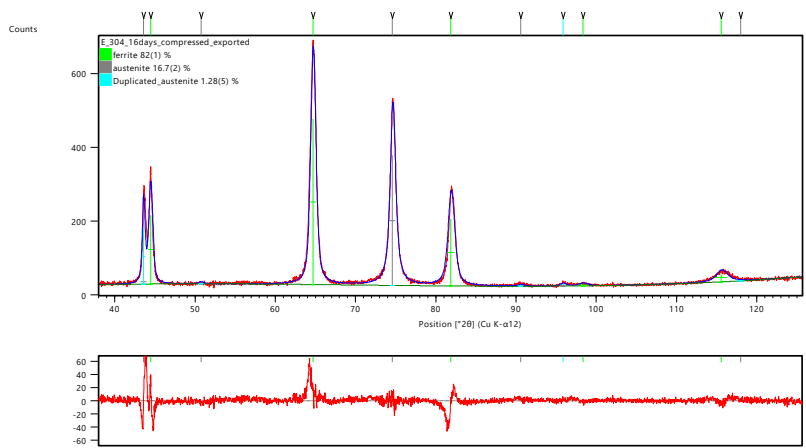
Agreement Indices	
R expected	13.86055
R profile	7.66358
Weighted R profile	10.3286
D-statistics	0.25429
Weighted D-statistics	0.54038
Goodness of Fit	0.74518
Mixture MAC [cm ² /g]	310.94
Custom Mixture MAC [cm ² /g]	-1

(a)



Agreement Indices	
R expected	13.6283
R profile	7.08055
Weighted R profile	9.57326
D-statistics	0.31074
Weighted D-statistics	0.60615
Goodness of Fit	0.70245
Mixture MAC [cm ² /g]	310.94
Custom Mixture MAC [cm ² /g]	-1

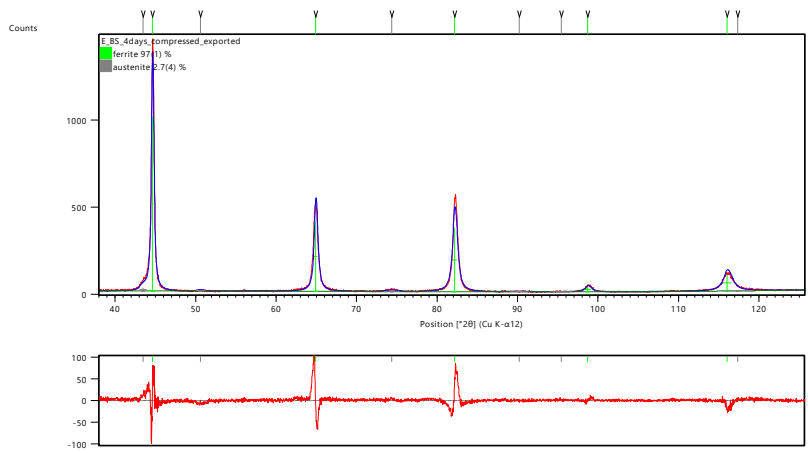
(b)



Agreement Indices	
R expected	13.6397
R profile	6.9196
Weighted R profile	9.6347
D-statistics	0.26476
Weighted D-statistics	0.59025
Goodness of Fit	0.70637
Mixture MAC [cm ² /g]	310.94
Custom Mixture MAC [cm ² /g]	-1

(c)

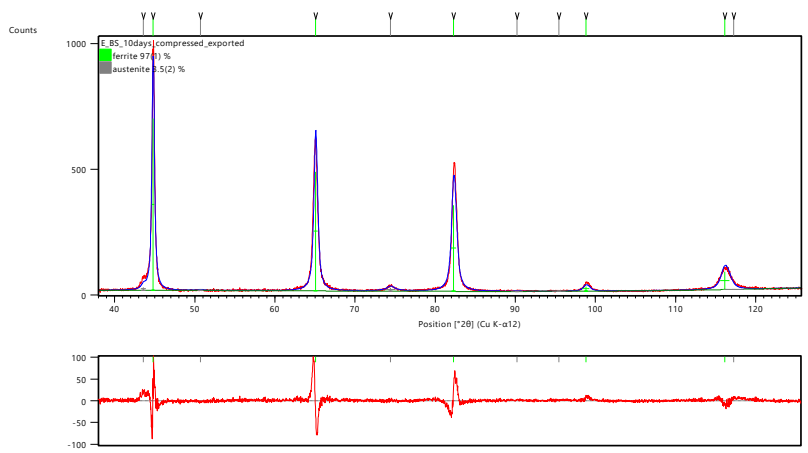
Appendix 6.21: XRD fitting using high-score Plus for Phase fraction analysis for austenitic steel specimens charged for different amount of time then compressed (a) 4 days; (b) 10 days; (c) 16 days



(a)

Agreement Indices

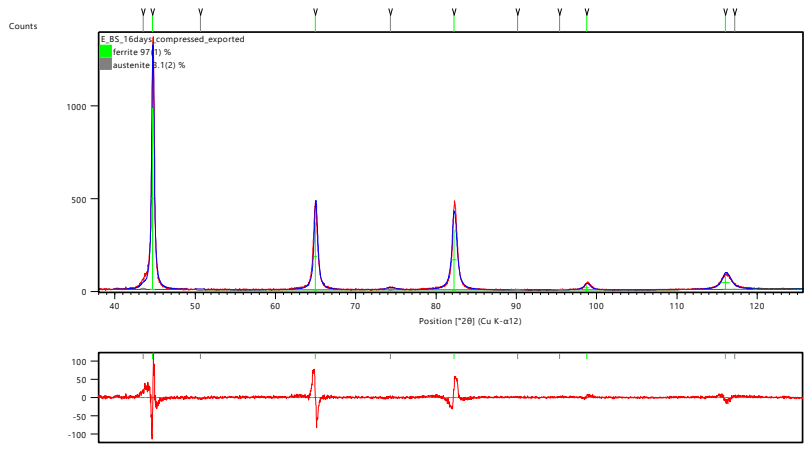
R expected	15.64244
R profile	9.74248
Weighted R profile	12.31942
D-statistics	0.18059
Weighted D-statistics	0.50976
Goodness of Fit	0.78756
Mixture MAC [cm ² /g]	310.94
Custom Mixture MAC [cm ² /g]	-1



(b)

Agreement Indices

R expected	16.08456
R profile	9.91481
Weighted R profile	12.16441
D-statistics	0.19573
Weighted D-statistics	0.55486
Goodness of Fit	0.75628
Mixture MAC [cm ² /g]	310.94
Custom Mixture MAC [cm ² /g]	-1



(c)

Agreement Indices

R expected	17.97168
R profile	11.34761
Weighted R profile	14.16465
D-statistics	0.14886
Weighted D-statistics	0.49077
Goodness of Fit	0.78817
Mixture MAC [cm ² /g]	310.94
Custom Mixture MAC [cm ² /g]	-1

Appendix 6.22: XRD fitting using high-score Plus for Phase fraction analysis for bainitic steel specimens charged for different amount of time then compressed (a) 4 days; (b) 10 days; (c) 16 days

6.4 Microstructure related calculations

Pic name	direction	n	Length	l	n	Length	l	n	Length	l	\bar{l}
x10_0004	rolling	6	767.5	75.6	8	767.5	56.7	7	765.5	64.6	65.6
	normal	35	576.0	9.7	44	574.5	7.7	46	575	7.4	8.3
x10_0005	rolling	7	757.9	64.0	9	759.4	49.9	6	759.9	74.9	62.9
	normal	48	572.6	7.1	44	572.7	7.7	50	572.7	6.8	7.2
x10_0006	rolling	9	767.5	50.4	7	767.5	64.8	9	765.5	50.3	55.2
	normal	46	574.6	7.4	36	573.5	9.4	42	574.5	8.1	8.3

(a)

Pic name	direction	n	Length	l	n	Length	l	n	Length	l	\bar{l}
x10_0002	transverse	13	760.0	34.7	14	758.9	32.2	11	760.0	41.0	36.0
	normal	37	570.3	9.1	42	569.3	8.1	39	570.3	8.7	8.6
x10_0003	transverse	13	762.7	34.8	11	763.7	41.2	13	763.7	34.9	37.0
	normal	42	572.6	8.1	38	572.1	8.9	40	572.2	8.5	8.5
x10_0004	transverse	15	758.5	30.0	13	757.9	34.6	15	758.5	30.0	31.6
	normal	41	569.3	8.2	35	570.3	9.7	42	569.9	8.1	8.7

(b)

Pic name	direction	n	Length	l	n	Length	l	n	Length	l	\bar{l}
x10_0006	rolling	5	757.5	87.7	6	758.0	73.1	6	757.6	73.1	78.0
	transverse	16	570.3	20.6	13	569.3	25.4	14	569.8	23.6	23.2
x10_0007	rolling	8	756.5	54.8	6	759.9	73.3	10	758.5	43.9	57.3
	transverse	13	569.3	25.4	9	569.8	36.7	9	568.3	36.6	32.9
x10_0008	rolling	8	761.7	55.1	6	761.8	73.5	9	763.2	49.1	59.2
	transverse	16	573.2	20.7	17	571.7	19.5	12	571.6	27.6	22.6

(c)

Appendix 6.23: Austenite grain size measurement along different directions for the duplex steel, (a) using images from transverse direction, (b) using images from rolling direction, (c) using images from normal direction images

Pic name	n	Length	l	n	Length	l	n	Length	l	\bar{l}
x5_0022	23	573.1	24.9	27	762.7	28.3	39	945.7	24.3	27.2±2
x5_0023	19	572.6	30.1	27	763.8	28.3	36	949.5	26.4	
x5_0024	22	569.8	25.9	27	759.5	28.1	33	947.8	28.7	

(a)

Pic name	n	Length	l	n	Length	l	n	Length	l	\bar{l}
x10_0005	24	572.6	23.9	25	763.2	30.5	30	953.4	31.8	27.2±3
x10_0006	22	572.1	26.0	25	764.2	30.6	38	953.7	25.1	
x10_0007	22	570.3	25.9	29	759.9	26.2	38	948.0	24.9	

(b)

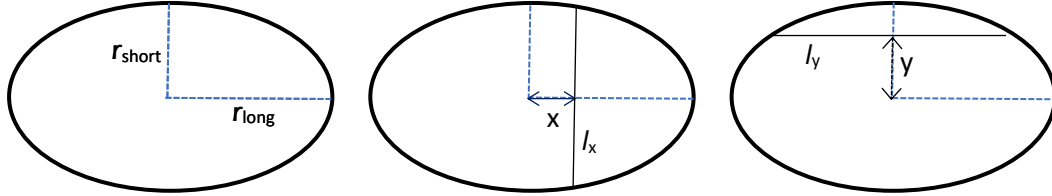
Pic name	n	Length	l	n	Length	l	n	Length	l	\bar{l}
x5_0035	18	573.1	31.8	29	763.1	26.3	36	951.4	26.4	26.3±2
x5_0036	23	573.2	24.9	28	764.2	27.3	35	951.7	27.2	
x5_0037	23	570.3	24.8	31	760.4	24.5	40	948.1	23.7	

(c)

Appendix 6.24: Austenite grain size measurement along different directions for the austenitic steel, (a) using images from direction 3; (b) using images from direction 2; (c) using images from direction 1

Pic name	n	Length	l	n	Length	l	n	Length	l	\bar{l}
X10000_005	16	8.14	0.509	25	11.70	0.468	22	11.83	11.83	0.50±0.04
X10000_008	11	5.46	0.496	13	5.79	0.445	12	5.35	5.35	
X10000_009	18	10.69	0.594	17	8.40	0.494	12	6.28	6.28	

Appendix 6.25: Bainitic steel plate thickness measurement



l_x and l_y are the possible interception lines during linear intercept measurements, given that all interceptions are made at each x, y value with same probability, then the average l_x and l_y values will be the measured mean line interception values, i.e. $\bar{l}_y \approx \bar{l}_{\text{Transverse}}$ and $\bar{l}_x \approx \bar{l}_{\text{Rolling}}$

In this case, $r_{\text{short}} = \bar{l}_{\text{Transverse,actual}} \approx 40 \mu\text{m}$ and $r_{\text{long}} = \bar{l}_{\text{Rolling,actual}} \approx 80 \mu\text{m}$

Using the ellipse equation, $\frac{x^2}{r_{\text{long}}^2} + \frac{y^2}{r_{\text{short}}^2} = 1$, and assuming (0,0) to be the ellipse centre point, we

can find out l_x and l_y at different x or y value:

y	l_x	y	l_x	y	l_x	y	l_x	\bar{l}_x
0	80	6	76.31514	11	66.81317	16	48	61.49457
1	79.89994	7	74.93998	12	64	17	42.14262	
2	79.59899	8	73.32121	13	60.79474	18	34.87119	
3	79.09488	9	71.44228	14	57.13143	19	24.97999	
4	78.38367	10	69.28203	15	52.91503	20	0	

x	l_y	x	l_y	x	l_y	x	l_y	\bar{l}_y
0	40	11	38.45777	21	34.04409	31	25.27845	31.09217
1	39.9875	12	38.15757	22	33.40659	32	24	
2	39.94997	13	37.82856	23	32.72614	33	22.60531	
3	39.88734	14	37.46999	24	32	34	21.07131	
4	39.7995	15	37.08099	25	31.22499	35	19.36492	
5	39.68627	16	36.66061	26	30.39737	36	17.4356	
6	39.54744	17	36.20773	27	29.51271	37	15.19868	
7	39.38274	18	35.72114	28	28.56571	38	12.49	
8	39.19184	19	35.19943	29	27.54995	39	8.888194	
9	38.97435	20	34.64102	30	26.45751	40	0	

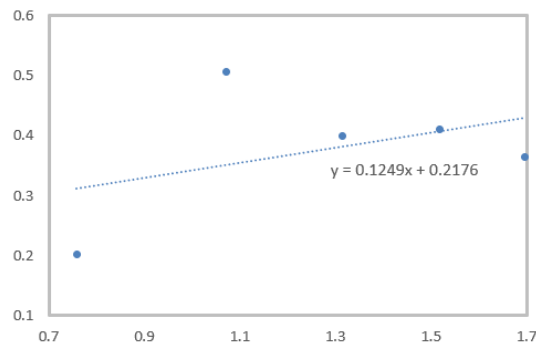
$\bar{l}_x = 61.49 \mu\text{m}$, it is within the limit of $\bar{l}_{\text{Rolling}} = 63.0 \pm 10 \mu\text{m}$ and $\bar{l}_y = 31.09 \mu\text{m}$, it is within the limit of $\bar{l}_{\text{Transverse}} = 30.55 \pm 10 \mu\text{m}$. Therefore, we can claim that $\bar{l}_{\text{Rolling,actual}}$ and $\bar{l}_{\text{Normal,actual}}$ values are representative of the actual average grain size.

Appendix 6.26: Proof of the $\bar{l}_{\text{Rolling,actual}}$ and $\bar{l}_{\text{Normal,actual}}$ values are representative of the actual average grain size along different direction and will give the linear interception values obtained earlier

Dislocation density before compression:

Peak	Position, 2θ	FWHM	Instrument broadening	real FWHM without Instrument broadening	$\cos\theta$	$2\sin\theta$	FWHM x $\cos\theta$
α 110	44.569	0.281	0.0634	0.2176	0.9253	0.7584	0.2014
α 200	64.766	0.67	0.0708	0.5992	0.8445	1.0712	0.5060
α 112	82.151	0.61	0.0794	0.5306	0.7538	1.3141	0.4000
α 220	98.754	0.72	0.0903	0.6297	0.6511	1.5180	0.4100
α 310	116.04	0.8	0.1108	0.6892	0.5296	1.6965	0.3650

Plot (FWHM x $\cos\theta$) against ($2\sin\theta$) gives:



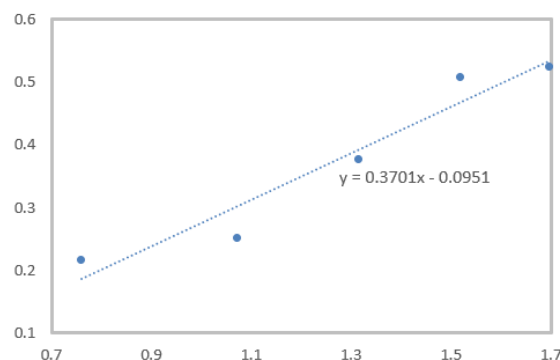
The slope of the fitting curve is the estimated micro-strain $\epsilon = 0.1249\%$

The unit cell length from XRD = 2.871907 a, the dislocation density is found to be: $4.75361 \times 10^{14} \text{ m}^{-2}$

Dislocation density of the specimen centre after compression:

Peak	Position, 2θ	FWHM	Instrument broadening	real FWHM without Instrument broadening	$\cos\theta$	$2\sin\theta$	FWHM x $\cos\theta$
α 110	44.659	0.298	0.0634	0.2346	0.9250	0.7599	0.2170
α 200	64.818	0.37	0.0708	0.2992	0.8442	1.0719	0.2526
α 112	82.233	0.58	0.0795	0.5005	0.7534	1.3152	0.3771
α 220	98.77	0.87	0.0903	0.7797	0.6510	1.5182	0.5076
α 310	115.97	1.1	0.1107	0.9893	0.5301	1.6958	0.5245

Plot (FWHM x $\cos\theta$) against ($2\sin\theta$) gives:



The slope of the fitting curve is the estimated micro-strain $\epsilon = 0.3701\%$

The unit cell length from XRD = 2.871603 a, the dislocation density is found to be: $4.17474 \times 10^{15} \text{ m}^{-2}$

Appendix 6.27: Bainitic steel dislocation density estimation before and after compression